Doctoral Thesis

High-Quality Phase-Pure Formamidinium Perovskite Layers for Efficient Perovskite Solar Cells

Woon Seok Yang

Department of Chemistry

Graduate School of UNIST

2019

High-Quality Phase-Pure Formamidinium Perovskite Layer for Efficient Perovskite Solar Cells

Woon Seok Yang

Department of Chemistry

Graduate School of UNIST

High-Quality Phase-Pure Formamidinium Perovskite Layer for Efficient Perovskite Solar Cells

A thesis/dissertation
submitted to the Graduate School of UNIST
in partial fulfillment of the
requirements for the degree of
Doctor of Philosophy

Woon Seok Yang

06 / 12 / 2019 of submission
Approved by

_____

Advisor
Sang Il Seok

High-Quality Phase-Pure Formamidinium Perovskite Layer for Efficient Perovskite Solar Cells

Woon Seok Yang

This certifies that the thesis/dissertation of Woon Seok Yang is approved.

06 / 12 / 2019 of submission

signature

_____

Advisor: Sang Il Seok

signature

_____

Myoung Soo Lah

signature

_____

Hoi Ri Moon

signature

_____

Jin Young Kim

signature

_____

Nam Joong Jeon

Abstract

High-Quality Phase-Pure Formamidinium Perovskite Layers
for Efficient Perovskite Solar Cells

By Woon Seok Yang

Department of Chemistry

UNIST

Advised by Prof. Sang Il Seok

Over the last few years, the metal halide perovskite has attracted considerable attention in the solar cell research field as a promising PV material.

Perovskite materials exhibit excellent photovoltaic properties such as diffusion length of long charge carriers due to low trap density, high absorption coefficient due to the direct bandgap, high open circuit voltage and small exciton binding energy. In addition, perovskite solar cells can be manufactured at a low cost through solution processes.

Recently, the recording efficiency of perovskite solar cells reached 24.2% in 1 sun condition, reported by the National Renewable Energy Laboratory.

In order to produce an efficient perovskite solar cell, many requirements are required. Among them, the quality of the perovskite film is a necessity that must be satisfied. Control of the composition of the material is also important, but forming a dense and uniform thin film on the substrate is critical to the production of high-performance perovskite solar cells.

Particularly, the quality of the perovskite thin film produced by the solution process can be greatly changed according to the process method.

In order to achieve high efficiency of the solar cell, the perovskite thin film should have appropriate morphological characteristics. As its characteristics, it includes sufficiently large particles, total surface coverage, low surface roughness, and good inter-particle connectivity.

However, unlike conventional organic thin films, it is very difficult to form a uniform and dense film by using simple spin-coating because of the rapid reaction between MAI or FAI and PbI_2 and self-assembling properties. Therefore, it is important to develop coating methods that improve surface roughness and reduce surface defects by controlling fast crystallization behavior.

In chapter 1, report on the synthesis of a PbI_2(DMSO) precursor with excellent capabilities for molecular exchange with FAI at low temperatures during the spinning process, as well as the fabrication of highly efficient $FAPbI_3$-based PSCs with certified PCEs exceeding 20 %. To fabricate $FAPbI_3$-based

PSCs through intramolecular exchange between DMSO and FAI (MABr) using pre-deposited PbI$_2$(DMSO) layers and a FAI (MABr) solution. The FAPbI$_3$ film derived from PbI$_2$(DMSO) exhibited a dense and well-developed grain structure with larger grains. I deposited FAPbI$_3$–based layers with a thickness of ~ 500 nm, and fabricated devices consisting of fluorine-doped tin oxide (FTO)-glass/barrier layer (bl)-TiO$_2$/mesoporous (mp)-TiO$_2$/perovskite/poly-triarylamine(PTAA)/Au. The current density-voltage (J-V) curves of the fabricated cells with FAPbI$_3$-based layers were measured under a standard air mass 1.5 global (AM 1.5G) illumination and the external quantum efficiency (EQE) spectra were measured. The J–V curves measured via reverse and forward bias sweep for one of the best-performing solar cell. The devices we fabricated also showed no hysteresis. J$_{SC}$, V$_{OC}$, and FF determined from the J–V curves were 24.7 mA / cm^2, 1.06 V, and 77.5 %, respectively, and correspond to a PCE of 20.2 % under standard AM 1.5G illumination. This study provides an effective protocol for fabricating efficient and cost-effective inorganic-organic hybrid heterojunction solar cells.

In chapter 2, I intend to increase the photovoltaic conversion efficiency of devices by controlling the added substances of intramolecular exchange process (IEPs). PbI$_2$, FAI, and MACl. In order to improve the optical-cell-physical properties such as light collection, electron transport, and electron diffusion, it is important to control a thin film shape with a uniform and large crystal grains and having few defects. PbI$_2$, FAI, and MACl make a significant contribution to making uniform and large crystalline FAPbI$_3$ films in IEPs. The morphology changes of FAPbI$_3$ films according to each material were observed through FESEM and the light conversion efficiency of the device was confirmed to confirm the conditions for producing high-efficiency perovskite solar cell.

In chapter 3, report the certified PCE of 22.1% in small cells and 19.7% in 1 cm^2 cells using the composition of defect-controlled perovskite films. Analyzed the perovskite films produced by the IEPs method using deep-level transient spectroscopy (DLTS) and time-correlated single photon counting (TCSPC) measurements. The addition of iodide ion to the organic cation solution used to form the perovskite thin film shows that it has a significant effect on the microstructure development, the concentration of the deep defect and hence the charge carrier recombination. I believe that the management of halide anions in the perovskite layer will provide a new direction for the production of high-efficiency PSCs.

Ultimately, the phase-pure FAPbI$_3$ and high-quality morphology of the perovskite layer formed through intramolecular exchange (IEPs) and control of concentration of deep defect and charge carrier recombination will provide directionality for high efficiency perovskite solar cell fabrication.

Key words
High quality, phase-pure FAPbI$_3$, Perovskite, Perovskite solar cell, Intramolecular exchange, Morphology, High efficiency, Iodide management, Defect

Contents

List of Figures

List of Tables

Chapter 1. Introduction

1.1 Solar Energy

Energy is the foundation for the development of human civilization. Today, the energy crisis of increasing energy demand, the depletion of energy resources, and the increase in environmental problems such as climate change has become a serious threat to human civilization.

According to BP's 2016 report[1], world energy consumption between 1965 and 2015 has increased from 43 petawatt-hours (PWh) to 153 PWh, which is illustrated in Figure 1.1.1. As you can see, the annual increase in energy consumption is almost linear and leads to a growth rate of about 2.2 PWh per year. Natural resources such as petroleum, coal and natural gas, which supplied most of the world's energy in the 20th century, are limited in quantity and cause environmental pollution caused by toxic gases generated through energy production. Therefore, development of sustainable and clean energy technology is urgent.

Despite the significant improvements in renewable energy conversion efficiency and technology over the last decades, most of the energy I use (~ 80%) comes from fossil fuels[2]. This can be seen in Figure 1.1.2. Burning fossil fuels, especially uncleaned coal, releases greenhouse gases and dust into the environment. Emissions of greenhouse gases are the cause of global warming and climate change, which can destroy the environment and threaten the safety of human activities. Renewable energy is a solution that solves energy starvation problems and mitigates environmental pollution problems.

As the most abundant energy source on the planet, solar energy can theoretically provide 89 petawatts (PW) of energy for human use. However, due to geographical accessibility, the energy available with current technology amounts to several thousand terawatts (TW)[3]. Nevertheless, this amount of energy is sufficient to meet the demand for global energy consumption.
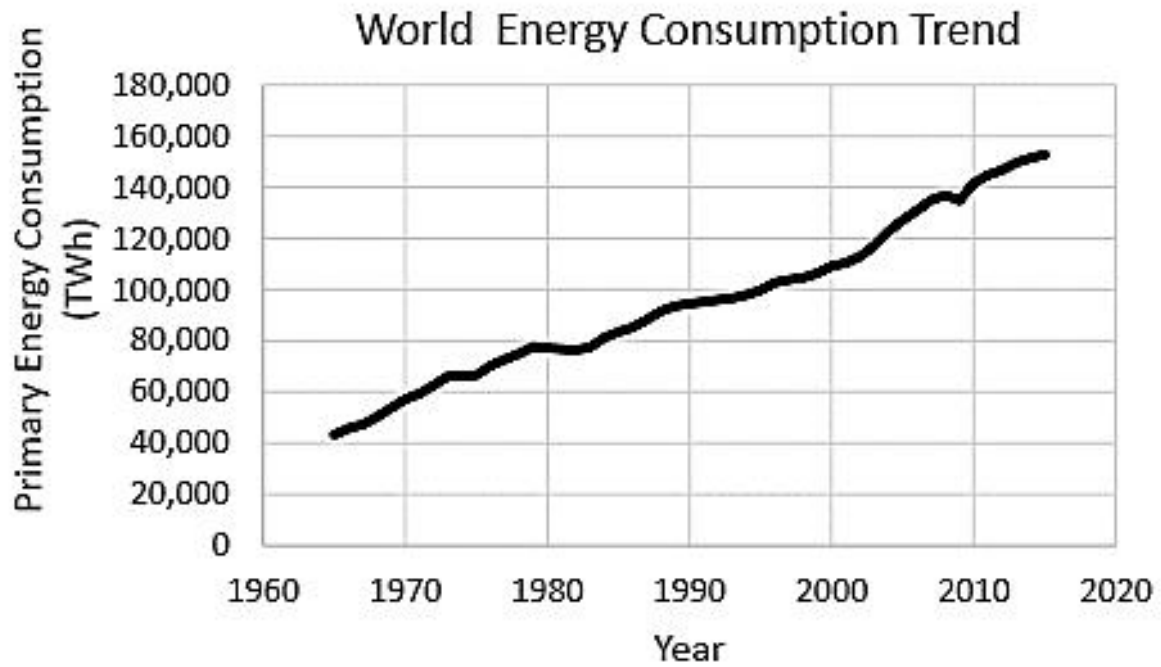
Figure 1.1.1 World energy consumption from 1965 to 2015[1].
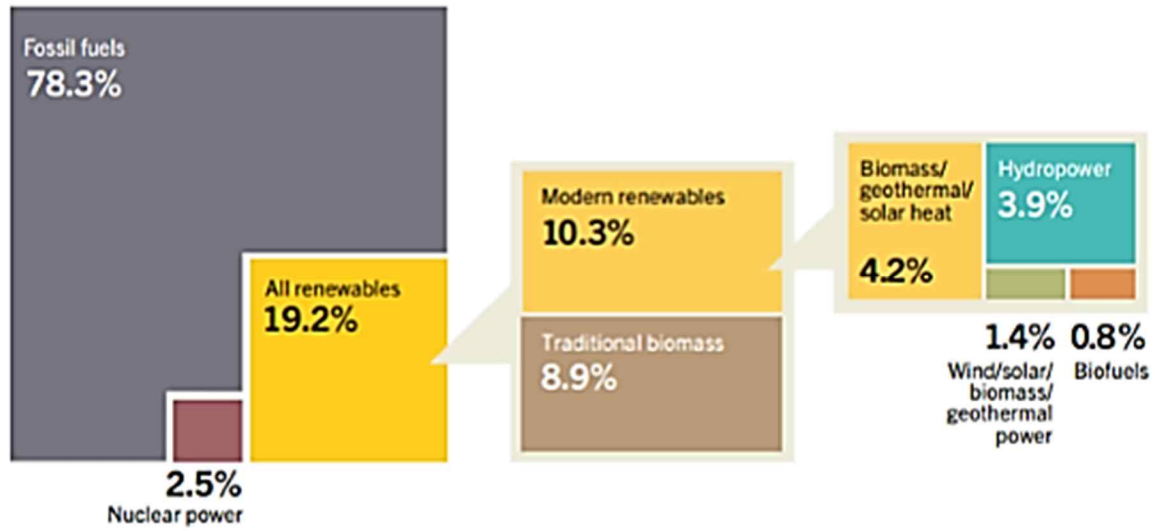
Figure 1.1.2 Renewable energy share of global final energy consumption in 2014[2].

1.2 Photovoltaic Devices

Photovoltaic cells (solar cells) are semiconductor devices that convert solar energy directly into electrical energy. To date, various types of solar cells have been studied, and Figure 1.2.1 shows a history of their evolution[4].

In the 1980s, research on silicon solar cells has been successful and solar cells have begun to improve photovoltaic performance. Recently, the most widely used semiconductor material in the field of solar cells is silicon (Si), and the power conversion efficiency (PCE) of crystalline Si-based photovoltaic cells is up to 25%[5].

Photovoltaic energy conversion is applied as a type of p-n junction type. Voltage is generated in solar cells by a process known as "photovoltaic effect". The collection of photo-generated charge carriers by p-n junctions causes transportation of electrons to the n-type layer and transportation of holes to the p-type layer[6].

The general energy conversion process proceeds as follows. The first step is light absorption. The photoactive semiconductor material absorbs light having energy higher than the bandgap of the active semiconductor material. Therefore, low-bandgap semiconductor materials are required for efficient light harvesting. In the second step, exciton formation and dissociation into a free charge carrier. A photon with energy greater than the bandgap of the photoactive semiconductor material excites electrons in the valence band to conductance band to produce an exciton. These excitons are dissociated into free charge carriers (free electrons, free holes) due to the presence of a strong built-in electric field. The third step is the charge transfer. The free charge carrier is transferred to the charge transport layer. The last step is the charge collection. The transferred free charge carrier is collected on the electrode and generates current.

The most basic of solar cell characterization technology is the measurement of power conversion efficiency (PCE). PCE is defined as the ratio of the power output from solar cells to the input power from sunlight. As shown in Figure 1.2.2, the characteristics of solar cell performance under illumination are commonly used by current density-voltage curves (J-V curves). Current density and voltage are represented by Y-axis and X-axis, respectively. The open circuit voltage (V_{OC}) is the maximum voltage at zero current. Short-circuit current density (J_{SC}) is defined as the current through the solar cell when the voltage is zero. The power per unit area is calculated as the product of current density and voltage, the voltage at the maximum power point (V_{max}), and the current density at the maximum power point (J_{max}).

Using this parameter, the fill factor (FF) and PCE are calculated using the following formula:

$$FF = \frac{J_{max} \times V_{max}}{J_{sc} \times V_{oc}} \qquad (1.1)$$

$$PCE = \frac{V_{oc} \times J_{sc} \times FF}{P_{in}} \qquad (1.2)$$

Where P_{in} is the incident light density.

These photovoltaic parameters are closely related to junction quality and recombination (i.e., radiation, Shockley-reed-hall, auger) in solar cells. Therefore, many important issues still have to be solved in order to obtain a high efficiency solar cell.
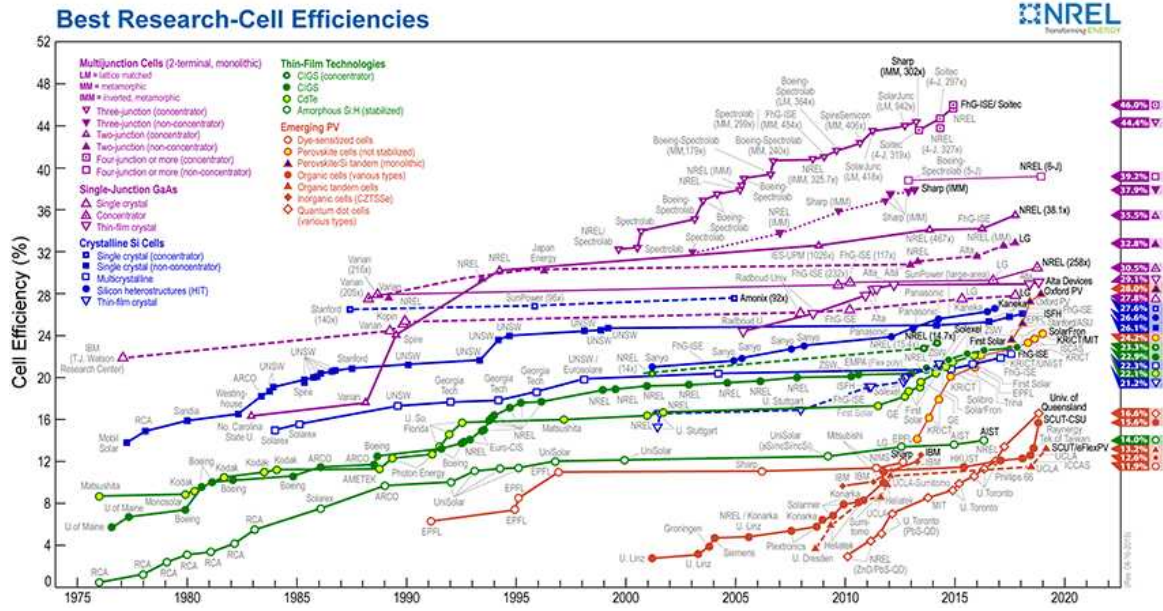
Figure 1.2.1 Best research-cell efficiency chart[4].
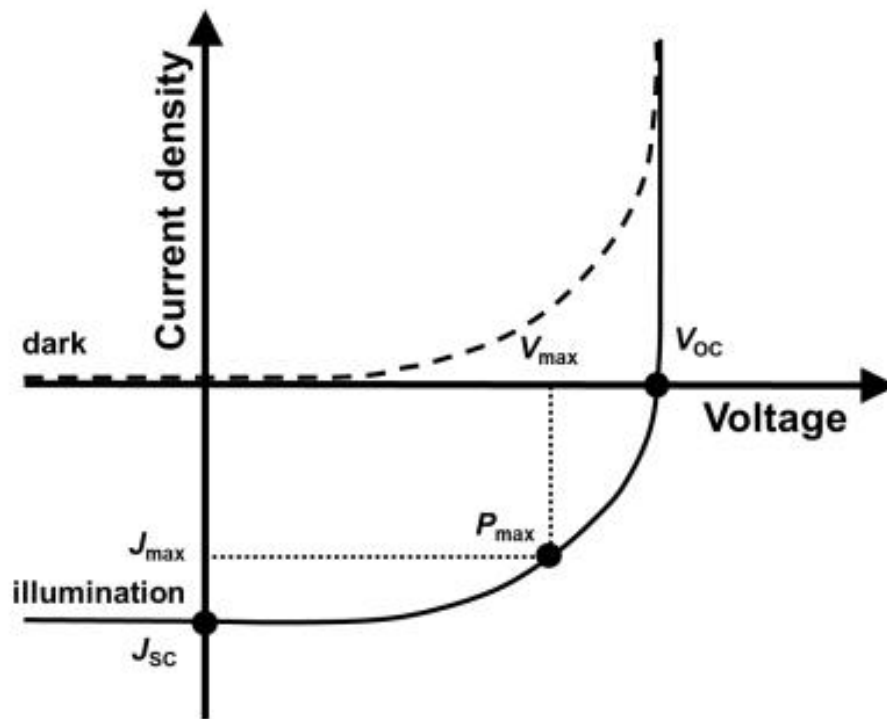
Figure 1.2.2 J-V curve of solar cells.

1.3 Perovskite Solar Cells (PSCs)

In order to make solar cells our main energy source, development of innovative materials to replace Si is the most important issue. It should also have a lower price than efficiency. Perovskite solar cells have sufficient potential as a satisfactory solution.

In 2009, Kojima et al. published a dye sensitized solar cell (DSSC) of 3.8% PCE using perovskite as a light absorber[7]. This discovery led to the emergence of new thin-film solar cells, perovskite solar cells (PSCs). Currently, PSCs are one of the most studied solar cells, and this interest is related to the fact that this technology has resulted in a significant increase in energy conversion efficiency from 3.8% to 22.1% over the past seven years. In addition, PSCs are easy to produce and show great potential for building integrated photovoltaic systems (BIPVs) that allow color[8]. The highest certified PCE to date is 24.2% belonging to the Korea Research Institute of Chemical Technology (KRICT).

Despite the significant development of lab-scale PSCs, perovskite-based PV still has to overcome several barriers. There are generally two major problems. Device instability of device performance and hysteresis of J-V (current density-voltage). At present, long range efficiency measurement is still not suitable for commercialization of PCS. In order to overcome this, it is very important to understand the decomposition mechanism of perovskite materials and device components such as hole transport medium (HTM) and electron transport medium (ETM). J-V hysteresis causes problems in standardizing measurement protocols of PSCs. In addition to improving the stability of the PSCs and reducing the J-V hysteresis, future studies include large-area manufacturing and lead-free perovskite thin film development. Perovskite is clearly the next candidate to replace Si due to its excellent structural, electrical and optical properties. Therefore, there is a need for continuous observation and study of the crystal and electrical structure of the perovskite material.

1.3.1 Perovskite Light Absorbing Material

Perovskite is the name of the crystalline structure of inorganic minerals $CaTiO_3$ discovered by German mineralogist Gustave Rose in 1839 and was named after Russian mineralogist Lew A. Perovski.

The crystal structure of the perovskite material is generally described as ABX_3, where the A, B, and X sites are an organic cation (e.g. methyl-ammonium $CH_3NH_3^+$, ethyl-ammonium $CH_3CH_2NH_3^+$ or formamidinium $NH_2CH=NH_2^+$), divalent metal cation (e.g. Ge^{2+}, Sn^{2+}, Pb^{2+}) and a halide anion (e.g. F^-, Cl^-, Br^-, I^-), respectively. A is a bulky cation that occupies the cubo-octahedral site shared with the 12X anion, and B is a smaller cation that is stabilized in the octahedral site shared by the 6X anion. Many such combinations provide excellent flexibility of perovskite properties. A typical unit cell structure of a basic perovskite compound is shown in Figure 1.3.1.

Perovskite compounds cause phase changes due to temperature changes. When the temperature is lower than 100K, perovskite exhibits a stable orthorhombic phase (γ). When the temperature is increased to 160K, a tetragonal phase (β) begins to appear and replaces the original orthorhombic phase (γ). As the temperature increases to about 330 K, the tetragonal phase (β) begins to be replaced by another stable cubic phase (α)[9]. Figure 1.3.2 shows all three crystal structures.

In $MAPbI_3$, the basic structure of the perovskite compound, the film deposited on mesoporous TiO_2 has an energy band gap of 1.5 eV, and the valence band energy position was estimated to be -5.43 eV below vacuum level using UPS[10]. From the optical band gap and the position of the valence band, the conduction band (ECB) was estimated to be -3.93 eV, as the energy band gap of $MAPbBr_3$ reported to be 2.2 eV[11], and for $MAPbCl_3$ 3.11 eV[12]. Depending on the crystal phase change, the lower symmetry of the orthorhombic system increases the bandgap to 1.6 eV and the higher symmetry of the cubic phase reduces the bandgap to 1.3 eV.

The ability to easily adjust the band gap of the perovskite compound in various ways has great advantages in solar cell applications. In addition, low exciton binding energy, long carrier lifetime, long diffusion length and high absorption coefficient are great advantages as an absorption layer for solar cells[13]. Therefore, perovskite materials can be widely used as promising harvesters in low-cost, high-efficiency solar cells.
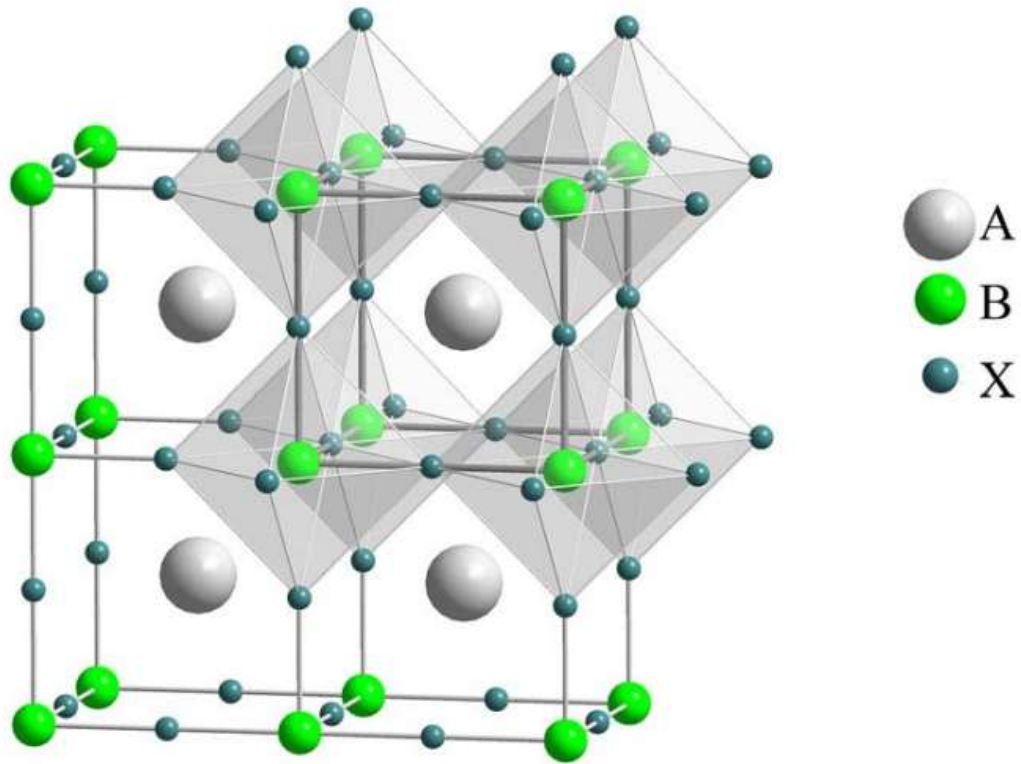
Figure 1.3.1 Ball and stick model of the basic ABX_3 perovskite structure and their extended network structure connected by BX_6 corner-sharing octahedral[14].
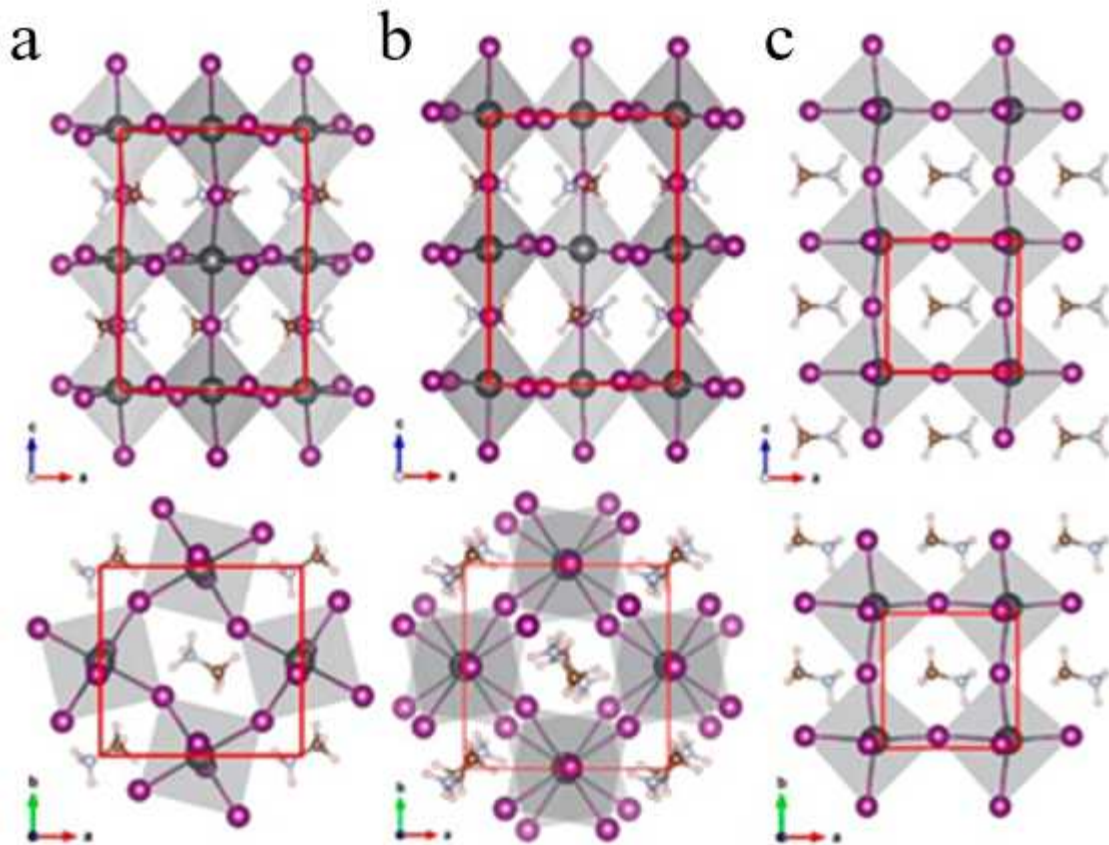
Figure 1.3.2 Various perovskite (MAPbI$_3$) phases belonging to different crystal systems: (a) orthorhombic (b) tetragonal and (c) cubic. Top row: viewed from the direction parallel to the b-axis (i.e. a-c plane) and bottom row: from the direction parallel to the c-axis (i.e. a-b plane)[15].

1.3.2 Structures of PSCs

Typical PSCs include a transparent conductive oxide (TCO), an electron transport layer (ETL), a perovskite based absorber, a hole transport layer (HTL), and a metal electrode.

The structure of PSCs has evolved from 2009 to the present. In 2009, Miyasaka et al. first used $CH_3NH_3PbI_3$ and $CH_3NH_3PbBr_3$ to replace organic dyes in dye-sensitized solar cells (DSSC)[7](Figure 1.3.3a). Park et al. used solid state HTL to replace liquid electrolyte in 2012. Mesoporous TiO_2 was used as the ETL and a spiro-OMeTAD solid organic small molecule as the HTL. This reported an efficiency of 9.7%[10]. In 2013, mesoporous TiO_2-based solar cells have been actively studied. PCE reached 20.1% using mesoporous TiO_2 and sequential deposition methods[16](Figure 1.3.3b). As shown in Figure 1.3.3c, the planar structure consists of a perovskite layer between the n-type thin film without the mesoporous layer and the p-type HTM. The most important factor in this structure is the compactness, crystal size and morphology of the perovskite layer. This structure is also a starting point for research on the structure of inverted organic solar cells and has produced excellent results[17]. A schematic diagram of the device structure is shown in Figure 1.3.3d. This is a significant step forward in allowing for the knowledge, materials, infrastructure expansion and manufacturing established for research and development of perovskite solar cells.
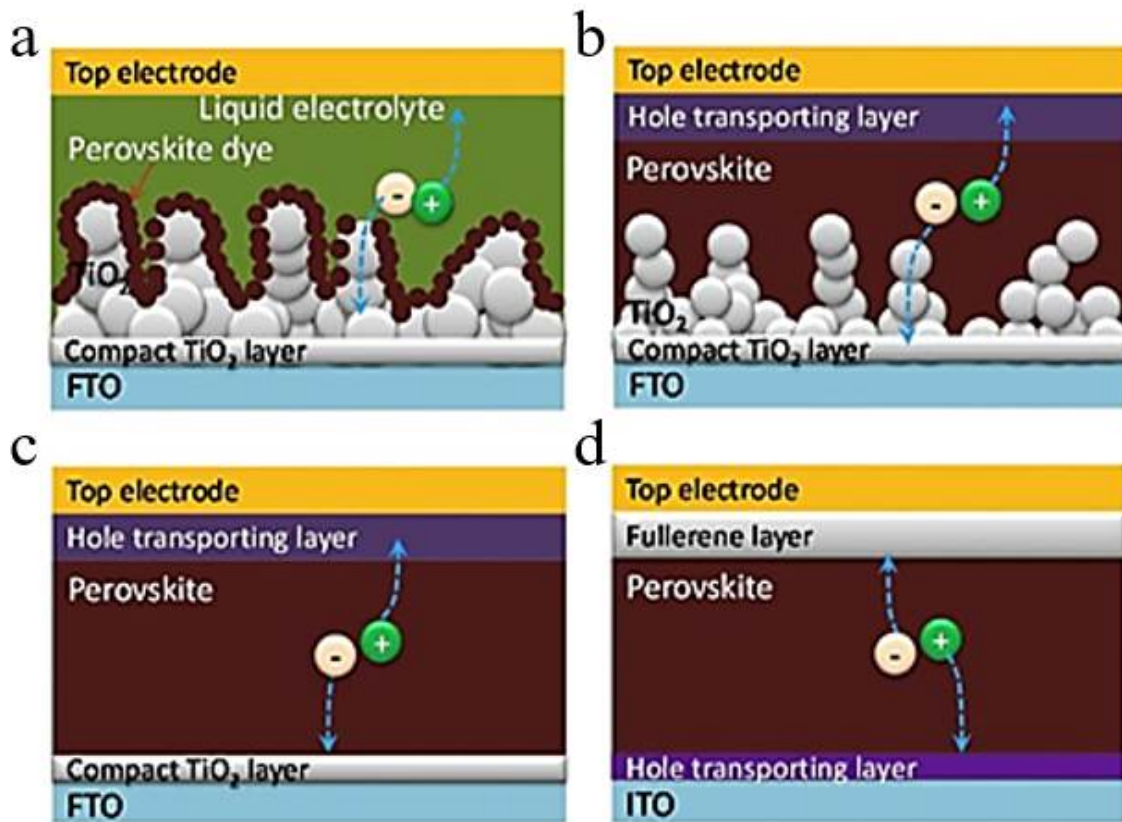
Figure 1.3.3 (a) Liquid DSSC structure perovskite solar cells with mesoporous TiO_2 layer and liquid electrolyte where the perovskite material worked as a sensitizer. (b) Solid-state DSSC structure perovskite solar cells with mesoscopic TiO_2 layer. (c) n-i-p planar hetero structure perovskite solar cells with a compact TiO_2 layer. (d) p-i-n planar hetero structure perovskite solar cells with a flat hole transporting layer at the bottom and fullerene transporting layers at the top.

1.3.3 Operating Principle of PSCs

Perovskite solar cells have very similar structures to common DSSCs. The most common configurations are 1) transparent conductive oxide (TCO) glass substrates, 2) semiconductor compact layers (commonly called blocking layers); 3) a mesoporous semiconductor film (scaffold); 4) Perovskite absorbing material; 5) hole transport materials (HTM); And 6) an electrically conductive back contact. The corresponding structure of this type of device is depicted in the figure 1.3.4. The blocking layer is typically made of TiO_2, an n-type material that selectively forms an n-i junction in the passage of electrons. The mesoporous layer serves to direct the light injecting electrons to the blocking layer, but it is not necessary in the PSC process. This is because there is evidence that the main role is to serve as a scaffold for the perovskite deposition[18].

The perovskite layer is a light absorbing material that produces charge separation that leads electrons to an n-i junction and holes to an i-p junction. The hole transport material is a p-type material that forms an optional i-p junction for hole transport. For effective charge extraction, the band alignment of the perovskite and the n- and p-type selective materials is very important: the conduction band of the electron transport layer should be lower than that of the perovskite conduction band and the valence band of the hole transport layer should be lower than the perovskite (Figure 1.3.5).

In a typical configuration of a PSC device, an electron-hole pair is created as the perovskite absorbs light (Eq. 1). The light-generated electrons are injected into the mesoporous semiconductor and the holes are directed into the HTM (Eq. 2) The injected electrons pass through the external circuit until they come into back contact, and the holes are carried to the same contact point by the hopping mechanism (electronic conduction). At the interface HTM / back contact, the hole and electron recombine regenerating the system (Figure 1.3.5a). The p-n junction is responsible for the creation of a built-in electric field that allows charge separation, where the electrons travel to the mesoporous TiO_2 and the holes travel to the HTM[19]. Since both materials have different Fermi levels, charge flows until they reach equilibrium. A space charge region appears at each interface and the resulting band bending is observed (Figure 1.3.5b).

$$\text{Perovskite} + h\nu \rightarrow (e^- \dots h^+)_{\text{perovskite}} \quad \text{(Eq. 1)}$$

$$(e^- \dots h^+)_{\text{perovskite}} \rightarrow e_{cb}^-(TiO_2) + h^+(HTM) \quad \text{(Eq. 2)}$$
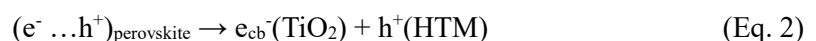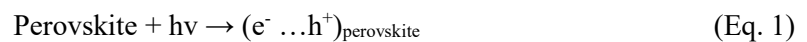
However, undesired reactions may occur, competing with the extraction of photogenerated charges.

The main back reactions are: exciton annihilation by photoluminescence – (Eq. 3); non-radiative recombination – (Eq. 4); and recombination of the charge carriers at the interfaces (TiO$_2$ surface, HTM surface and TiO$_2$/HTM interface) – (Eqs. 5~7); with consequent heat release.

$$(e^- \ldots h^+)_{perovskite} \rightarrow h\nu' \qquad \text{(Eq. 3)}$$

$$(e^- \ldots h^+)_{perovskite} \rightarrow \triangledown \qquad \text{(Eq. 4)}$$

$$e_{cb}^-(TiO_2) + h^+(perovskite) \rightarrow \triangledown \qquad \text{(Eq. 5)}$$

$$h^+(HTM) + e^-(perovskite) \rightarrow \triangledown \qquad \text{(Eq. 6)}$$

$$e_{cb}^-(TiO_2) + h^+(HTM) \rightarrow \triangledown \qquad \text{(Eq. 7)}$$
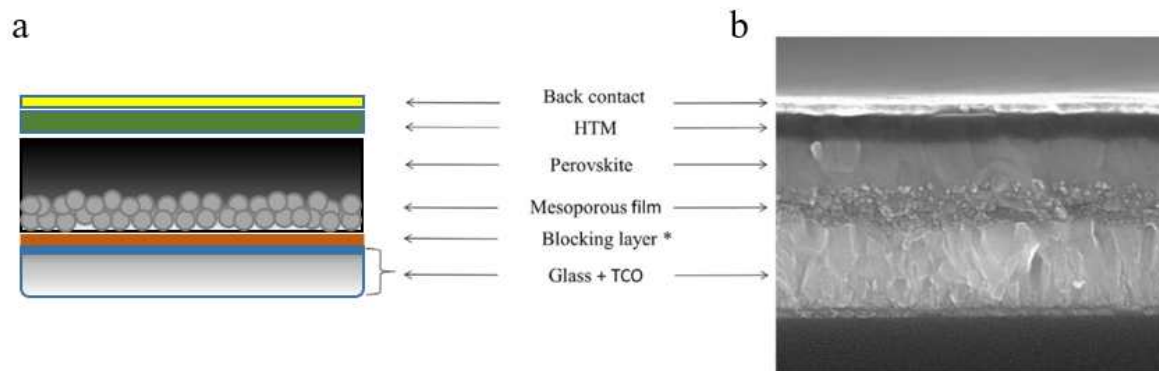
Figure 1.3.4 Typical mesoporous perovskite solar cell: (a) sketch illustrating the multilayer arrangement and; (b) a scanning electron microscopy (SEM) image (*the blocking layer is so thin that is imperceptible in SEM image).
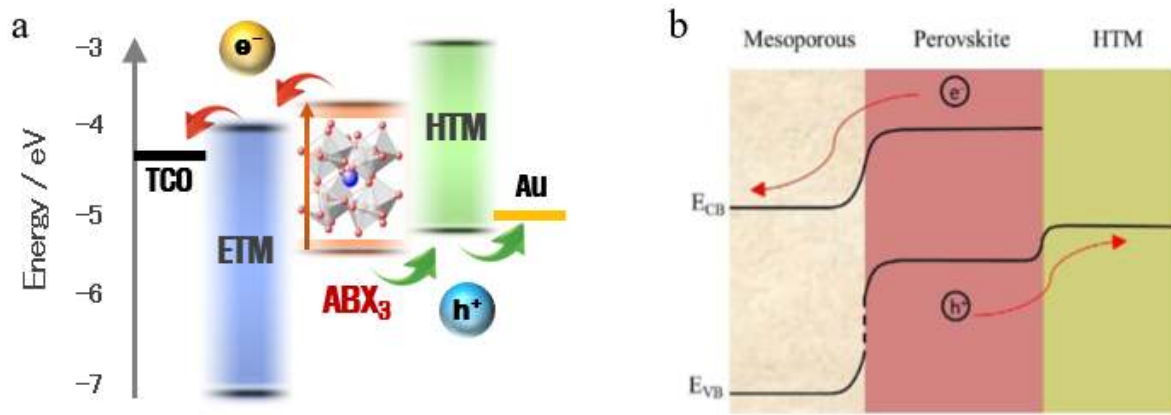
Figure 1.3.5 (a) Energy diagram of a typical PSC representing the energy levels of typical materials used in the different layers and (b) band-bending of energy levels during separation of charges.

Chapter 2. Main Parameters of PSCs: Perovskite layer for Enhanced Efficiency

2.1 Main Parameters of PSCs

The performances of PSCs are mainly characterized by six parameters such as IPCE, J_{SC}, V_{OC}, FF, PCE and J-V curves. Also, the long-term stability of PSCs under continuous simulated solar-light irradiation is a vital parameter for sustained cell operation. These photovoltaic key parameters are explained below.

Short Circuit Current (J_{SC})

Short circuit current density (J_{SC}) is the actually generated current density by the cell without bias potential. The J_{SC} value is the photocurrent per unit area (mA/cm^2) when a PSC under irradiation is short-circuited. The J_{SC} is related to the interaction between ETL and the perovskite, as well as the carrier lifetime of the perovskite. A high J_{SC} value is thus associated with the following characteristics: 1) intense light absorption capabilities of perovskite over the wide range of sunlight, 2) the long carrier lifetime for high electron injection efficiencies from photo-excited perovskite to the CB of ETL, and 3) efficient regeneration of the oxidized perovskite by HTM. The J_{SC} value strongly depends on the photophysical and electrochemical properties and carrier lifetime of the perovskite. The J_{SC} value can be derived by integrating the IPCE spectra to give equation (Eq. 1).

$$J_{SC} = e \int IPCE\ (\lambda)I_S(\lambda)d\lambda\ =\ \int(LHE(\lambda) \times \eta_{inj}\ \times \eta_{col}\ )I_S(\lambda)d\lambda \qquad \text{(Eq. 1)}$$

in which $I_S(\lambda)$ is the photon flux at wavelength λ in AM 1.5 (100 mWcm^{-2})

Open Circuit Potential (V_{OC})

V_{OC} is the difference in the electrical potential between the two terminals when there is no external load connected, i.e. when the circuit is broken or open. In other words, the current does not flow externally, even when there are internal currents such as self-discharge currents in batteries. It is influenced by the semiconductor's properties and I_0 (reverse-saturated current). The relation between them is derived from equation (Eq. 2),

$$I = I_O \left(\exp\left(\frac{eV_A}{KT}\right) - 1 \right) \qquad \text{(Eq. 2)}$$

$$V_{OC} = \frac{KT}{e} \ln\left(\frac{I_L}{I_O} + 1\right) \qquad \text{(Eq. 3)}$$

$$V_{OC} \approx \frac{KT}{e} \ln\left(\frac{I_{SC}}{I_O}\right) \qquad \text{(Eq. 4)}$$

For high V_{OC}, obtain higher I_L and lower I_O. The lifetime of the minority carriers should be prolonged to obtain lower I_O from equation (Eq. 5).

$$I_O \propto \sqrt{\frac{D}{\tau}} \qquad \text{(Eq. 5)}$$

This requires the reduction of the recombination velocity. The relation between the band gap and V_{OC} is obtained from equations (Eq. 6, 7).

$$n_i^2 = N_c N_v \exp\left(-\frac{E_g}{KT}\right) \qquad \text{(Eq. 6)}$$

$$I_O = \alpha \exp\left(-\frac{E_g}{KT}\right) \qquad \text{(Eq. 7)}$$

Therefore,

$$E_g \downarrow \Rightarrow I_O \uparrow \Rightarrow V_{OC} \downarrow$$

As shown in the above equation, V_{OC} is most affected by the band gap (E_g) and electron recombination.

Fill Factor (FF)

Fill factor (FF) is a value between 0 and 1, exhibiting the degree of the ideality of the cell. The ideality means that a cell has no loss of generated current during the operation. If the cell has no internal resistance, impedance, and defects, FF goes to 1 and the corresponding J-V curve has a rectangular graph. However, because there is no ideal device in the real world, some losses in the cell inevitably occur, resulting in the necessity of FF as the criterion. FF is calculated by a simple formula (Eq. 8):

$$FF = \frac{P_{m\,ax}}{J_{SC} \times V_{OC}} \qquad\qquad (Eq.\ 8)$$

Where $P_{m\,ax}$ is the maximum value among the products of J values and V values at each measuring point. The value of the fill factor reflects the resistances of series (R_S) and parallel resistances (R_{sh}) losses occurring during operation of the PSCs, which include the sheet resistance of the substrate and counter electrode, electron transport resistance and leakage current through the solar cells, and the charge-transfer resistance at the counter electrode. Increasing the shunt resistance and decreasing the series resistance as well as reducing the overvoltage for diffusion and electron transfer will lead to higher fill factors, thus resulting in greater PCE and pushing the output power of the cell closer toward its theoretical maximum. Therefore, careful PSCs fabrication is important for obtaining high photovoltaic performance.

Photocurrent Photovoltage Curves (J-V curves)

Measurement of the J-V curve is an easy and useful method for the evaluation of the photovoltaic performance of a PSCs. A typical J-V curve is depicted in Figure 2.1.1. The performances of PSCs are universally represented by the following four key factors; open-circuit photovoltage (V_{OC}), short-circuit photocurrent density (J_{SC}), fill factor (FF) and power conversion efficiencies (PCE).

The point (J_{max}, V_{max}) on the J-V curve, where the maximum power is produced, is the product of current and voltage and is illustrated in the Figure 2.1.1 as the area of the rectangle formed between a point on the J-V curve and the axes. The maximum power point is the point on the J-V curve where the area of the resulting rectangle is largest.
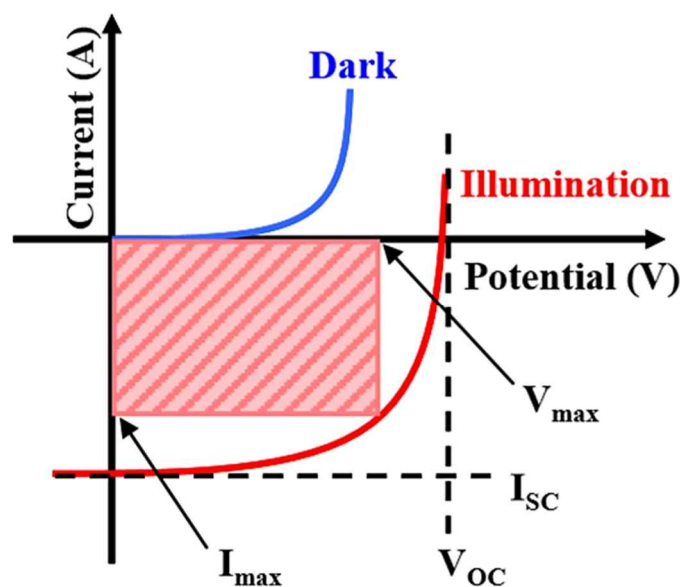
Figure 2.1.1 Graph of current versus voltage for photovoltaic devices.

Power Conversion Efficiency (PCE)

The most representative index, PCE of the cell, is the ratio of the output power of the cell to the input power from the external surroundings (i.e., sunlight from the solar simulator). It is defined as the maximum power in the J-V curve. It can be considered as the P_{max} mentioned above, hence calculated by the relation (Eq. 9):

$$PCE(\%) = \frac{J_{SC}(mA/cm^2) \times V_{OC}(V) \times FF}{I_O(mW/cm^2)} \times 100 \qquad (Eq.\ 9)$$

Where I_O is the power of incident light (as mentioned, usually 100 mW/cm²). Because one of the most important criteria for determining the characterization of solar cell is the power conversion efficiency (PCE), J-V measurement, the most frequently used analysis for measuring PCE, should be introduced briefly here. J-V measurement requires two major equipments: solar simulator and potentiostat. The solar simulator generates artificial solar light and projects it to the solar cells. Although the output power of solar simulator can be controlled variously, the standard condition for measuring PCE is AM 1.5 (1 sun condition) which has an intensity of 100 mW/cm². Generated photocurrent by solar cells is measured by the potentiostat. For the clear and specific analyses on PCE, the output current of solar cell is measured at various external bias potentials applied to the cell. As a result, the output photocurrent depending on the varying bias potential is plotted as graphs of voltage (x-axis)-current density (y-axis). Consequently, to obtain a high PCE value, optimization of the values of J_{SC} and V_{OC} of the cell is essential.

Incident-Photon-to-Conversion Efficiency (IPCE)

The IPCE [also referred to as the external quantum efficiency (EQE)] is defined as the number of electrons flowing through the external circuit divided by the number of incident photons and can be represented by Equation (Eq. 10):

$$IPCE(\%) = \frac{1240 \times J(mA/cm^2)}{\lambda(nm) \times P(W/m^2)} \qquad (Eq.\ 10)$$

In which J_{ph} is the short-circuit photocurrent density generated by monochromatic light, and λ and P are the wavelength and intensity of the monochromatic light, respectively. A plot of IPCE versus excitation wavelength is termed an IPCE spectrum or a photocurrent action spectrum. The IPCE spectrum is very useful for the evaluation of a new perovskite sensitizer for PSCs. On the other hand, IPCE can also be expressed as the product of light-harvesting efficiency LHE(λ)=1-10^A] for photons of

wavelength λ, the quantum yield of electron injection (Φ_{inj}) from the excited perovskite to the CB of the TiO$_2$ electrode, and the efficiency of collection of the injected electron (η_{col}) at the FTO glass.

$$IPCE(\lambda) = LHE(\lambda) \cdot \Phi_{inj} \cdot \eta_{col} \qquad \text{(Eq. 11)}$$

IPCE is therefore directly related to the absorption properties of the perovskite, the thickness of perovskite on the ETL surface (or LHE), the quantum yield of electron injection from the excited perovskite to the CB of the ETL, and the efficiency of collection of electrons in the external circuit. The maximum IPCEs for PSCs lie in the 85-90% range; they do not reach 100% experimentally because of reflection and absorption losses (10-15%) due to the FTO glass.

Loss Mechanism of Solar Cells

The factors which allow the parameters of the solar cell to be reduced ultimately cause a decrease in cell efficiency. I$_{SC}$ is affected by both the optical losses and electrical losses. Surface reflections and the shadow effect from the metal grid are the dominant factors reducing the incident light. To solve such problems, an antireflection coating and surface texturing are applied to prevent surface reflections and improved grid designs such as buried contacts are investigated. Also, carrier recombination at the front surface is another key issue in this field. A well-organized passivation layer and defect management are required. On the other hand, V$_{OC}$ is closely related to the built-in potential of the semiconductor and recombination velocity. An optimized p-n junction and low recombination velocity can allow a high value of V$_{OC}$ to be achieved. In addition, FF is mainly determined by the resistance values, viz. the series resistance, R$_s$, and shunt resistance, R$_{sh}$. There are several physical mechanisms responsible for these resistances, such as the bulk resistance of the semiconductor materials or metallic contacts for R$_s$, and the leakage current at the crystal defects or impurities for R$_{sh}$. Ideally, very low values of R$_s$ and very high values of R$_{sh}$ are required (Figure 2.1.2)[20].
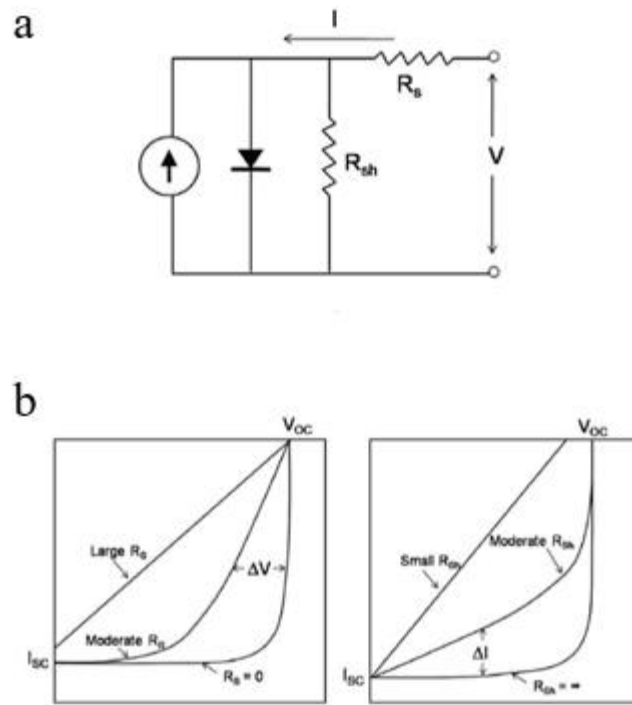
Figure 2.1.2 (a) Equivalent circuit (b) effects of resistance on the I-V characteristics[20].

2.2 Key Parameters for Efficiency Enhancement of Perovskite layer

2.2.1 Enhancement of J_{SC}

Improvement Absorption and Optimized Bandgap of Perovskite

The absorption coefficient of perovskite material is above 3.0×10^4 cm^{-1} in the visible range, which indicates that the perovskite material only needs 380 nm to absorb 90% of the visible light by taking into consideration the electrode reflection[21]. As a matter of fact, most of the reported high-efficiency devices had a thickness of around 300–600 nm.

Another advantage of the perovskite materials is the maneuverability of its bandgap. The bandgap can be tuned by changing the atoms at any sites of A, B or X in the ABX$_3$ structure. It is established that the corner-sharing BX$_6$ octahedral plays a major role in determining the band structure[21, 22]. Theoretical calculations show that conduction band minimum (CBM) of CH$_3$NH$_3$PbI$_3$ is mainly from Pb p orbital with negligible coupling with I s orbital, and the valance band maximum (VBM) has strong Pb s and I p antibonding character[23-25]. Nevertheless, the size of A cation also plays an important role in controlling the B–X bond length and electron cloud overlap between B and X atoms. A larger or smaller A cation can cause the whole lattice to expand or contract[26]. A longer B–X bond length induces the reduction of the electron cloud overlap between B and X atoms, which causes the decreased bandgap. Eperon et al. first used a slightly larger formamidinium cation (FA$^+$) to replace MA$^+$, the bandgap was reduced from 1.55 to 1.48 eV, corresponding to an absorption edge shift from 800nm to around 840 nm[26]. The formamidinium lead iodide (FAPbI$_3$)-based perovskite solar cell devices delivered a photocurrent of 23mA/cm^2 due to the extended light absorption. On the contrary, a smaller cesium cation (Cs$^+$) at A site causes the bandgap to increase to 1.73 eV[26]. For the X halide site, by replacing I$^-$ with Br$^-$ or Cl$^-$, the bandgap can be tuned from 550 nm for MAPbBr$_3$ to 400 nm for MAPbCl$_3$, respectively. Figure 2.2.1a–b shows the continuous tuning of the optical bandgap of FAPbI$_y$Br$_{3-y}$ ($0\leq y\leq 1$) based materials[26]. It is clear that the absorption edge was tuned from 840 nm for FAPbI$_3$ to 550 nm for FAPbBr$_3$ perovskite.

For the metal B site, experiment results showed that larger B cation size results in the increased bandgap. The bandgap of the MAPbI$_3$ was decreased to 1.2 eV by replacing the Pb$^+$ with smaller Sn$^+$[27]. The trend of the bandgap change with respect to each atom size of the perovskite structure is shown in Figure 2.2.2.
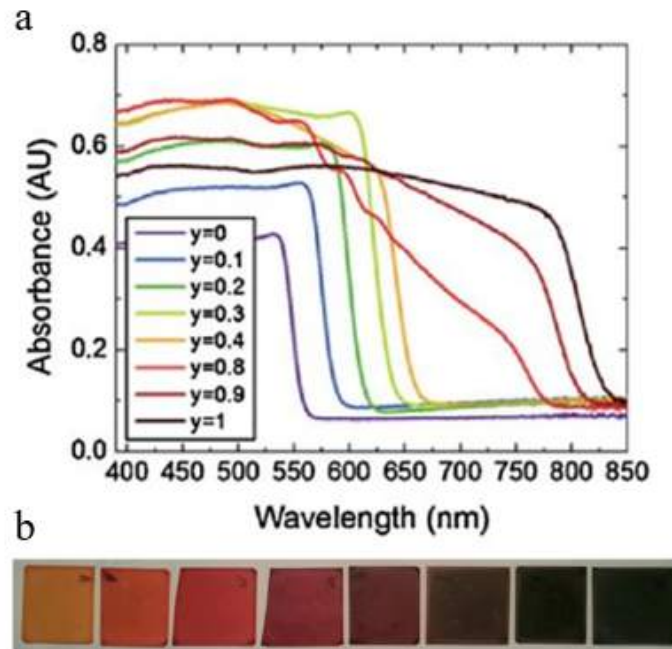
Figure 2.2.1 (a) UV–Vis absorbance of the $FAPbI_yBr_{3-y}$ perovskites with varying y, measured in an integrating sphere. (b) Photographs of the $FAPbI_yBr_{3-y}$ perovskite films with y increasing from 0 to 1 (left to right) [26].
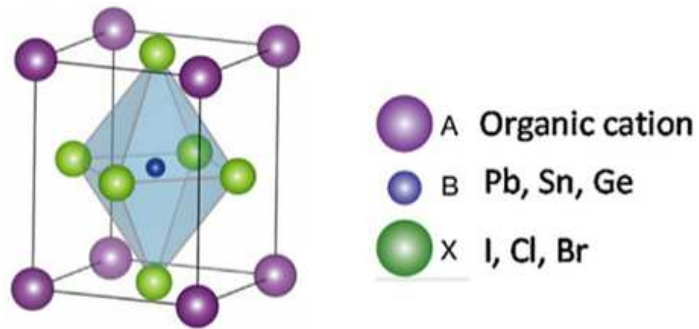
Figure 2.2.2 Bandgap tuning of the perovskite by change the atom size of different sites in the perovskite structure.

Improvement Charge Carrier Mobility of Perovskite Films

An important reason for perovskite materials to work as promising photovoltaic materials is their high charge carrier mobility. The theoretical limit of carrier mobility is determined by the effective mass of the electrons and holes which is controlled by the energy band structure. Like any semiconductor material, the carrier mobility of the perovskite is affected by the shape and defect of the material.

In polycrystalline films, grain boundaries usually slow down charge transport because of its possible charge trapping and scattering effects caused by grain orientation, dislocations, dangling bonds or composition change at grain boundaries. Since the perovskite materials easily decompose at low annealing temperature while most perovskite films need to be annealed for grain growth, there is large chance to form non-stoichiometric perovskite at film surface and grain boundaries by losing the organic cations. A recent local optical study by Ginger et al. showed that the grain boundaries actually show weaker photoluminescence emission as well as shorter charge recombination lifetime as shown in Figure 2.2.3, which directly confirmed that grain boundaries do have a negative impact to the photogenerated charges[28]. In our initial study of carrier transport along lateral direction in polycrystalline film, observed that grain boundary reduced carrier mobilities, while a grain boundary passivation can effectively recover the excellent charge transport properties even in polycrystalline films[29]. Lateral carrier transport was studied because the grain size in our perovskite films was generally comparable or much larger than the film thickness so that the carrier transport in vertical direction actually does not need to across a grain boundary[30]. Bi et al. experimentally shown that, in the polycrystalline MAPbI$_3$ film, the Hall mobility of holes was increased from 2.5 cm^2/V s to around 30 cm^2/V s after thermal annealing of perovskite films for 1.5 h. The increased mobility is mainly due to the increased crystallinity and average grain size of the perovskite films which reduced the grain boundary area. The grain size was increased from less than 190 nm to over 300 nm during the heating process[31]. Therefore, in order to have long carrier mobility in perovskite film, increasing large grains and the passivation of grain boundaries must be improved.
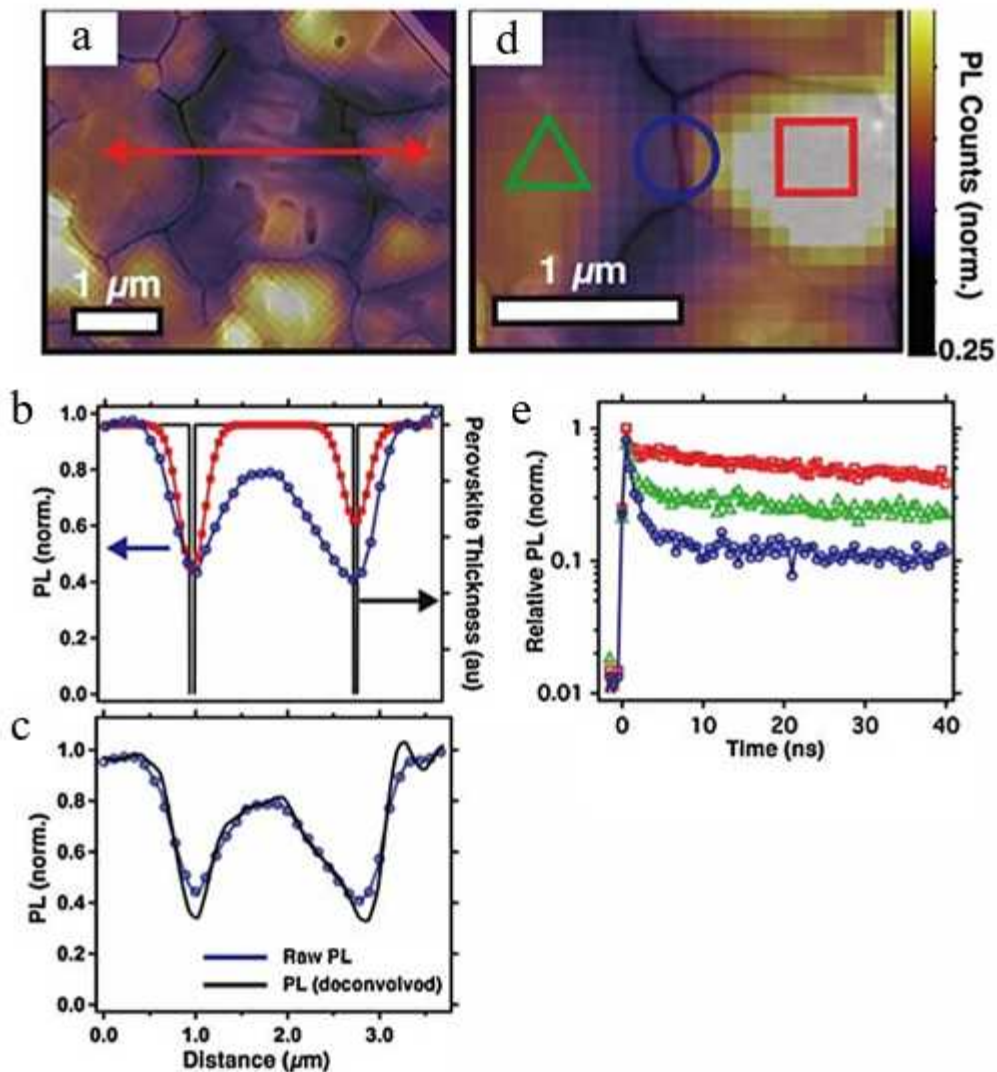
Figure 2.2.3 (a) Fluorescence image with semi-transparent SEM overlay showing a line scan (red arrow) across two distinct grain boundaries. (b) Convolution data analysis showing at grain boundaries the half width at half max (HWHM) of the measured PL quenching trace (blue circles) is larger than the HWHM of the point spread function (PSF, red squares) convolved with the grain boundary width (black line). (c) Deconvolved the PSF from the raw PL quenching at the GB to determine the spatial extent (~210 nm) and absolute magnitude (~65%) of PL quenching. (d) Fluorescence image of $CH_3NH_3PbI_3(Cl)$ film on glass showing PL intensity variations at a bright grain (red square), grain boundary (blue circle), and dark grain (green triangle). (e) Time resolved photoluminescence traces showing grain boundaries (blue circle) quench PL significantly more than dark (green triangle) and bright regions (red square) [28].

2.2.2 Enhancement of V_{OC}

Improvement PbI₂ Crystals of Perovskite Films

The standard perovskite in the community has so far been methylammonium lead iodide, $MAPbI_3$, but both the organic ion and the halide can be substituted. MA has for example been replaced with formamidinium (FA)[16, 32-34], and iodine by chlorine[35] and bromine[36]. The MA/FA and Br/I ratios can also be changed simultaneously[16, 37, 38], and the best cells at the moment are based on mixed perovskites with compositions around $MA_{1/3}FA_{2/3}Pb\text{-}(Br_{1/6}I_{5/6})_3$[39, 40]. For a given perovskite, the precise stoichiometry is important as well. Most notably, a slight excess of PbI_2 in the perovskite film has been observed to be beneficial[39, 41, 42]. PbI_2 may, for example, passivate the TiO_2 interface[39, 43-45] and thereby decrease hole recombination, either due to surface passivation or band edge matching between TiO_2, PbI_2, and the perovskite (Figure 2.2.4a). Another benefit is that PbI_2 could facilitate electron injection into TiO_2[41, 46]. As excess of PbI_2 is beneficial also when blocking layers other than TiO_2 are used, i.e., SnO_2[37], those appear to be less likely explanations. At the perovskite/HTL interface, PbI_2 could, according to similar reasoning, act as an electron blocking layer, facilitate hole injection, and thereby decrease recombination[44, 47] (Figure 2.2.4b). These results show that the incorporation of PbI_2 is a crucial strategy in polycrystalline perovskite solar cells, which are fabricated by a solution process for realizing high-efficiency perovskite-based solar cells.
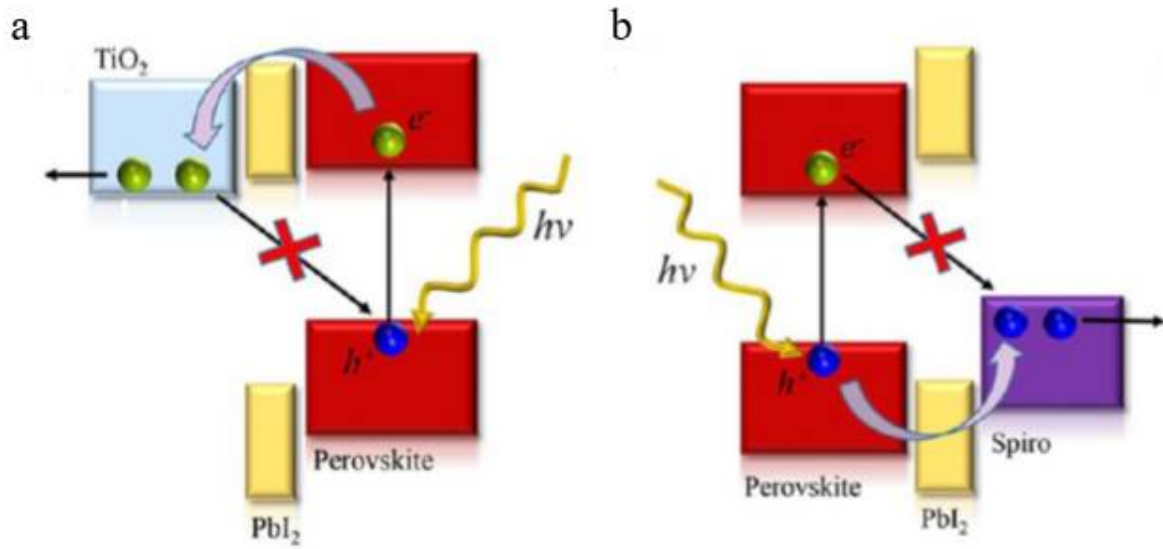
Figure 2.2.4 (a) PbI_2 as a passivating layer at the back contact. (b) PbI_2 as a passivation layer next to the hole-selective layer[48].

2.2.3 Enhancement of FF

The series resistance arises from the resistance of the cell material to current flow, particularly through the front surface to the contacts, and from resistive contacts. Series resistance is a particular problem at high current densities, for instance under concentrated light. The parallel or shunt resistance arises from leakage of current through the cell, around the edges of the device and between contacts of different polarity. It is a problem in poorly rectifying devices. Series and parallel resistances reduce the fill factor as shown in Figure 2.2.5. For an efficient cell, want R_s to be as small and R_{sh} to be as large as possible.
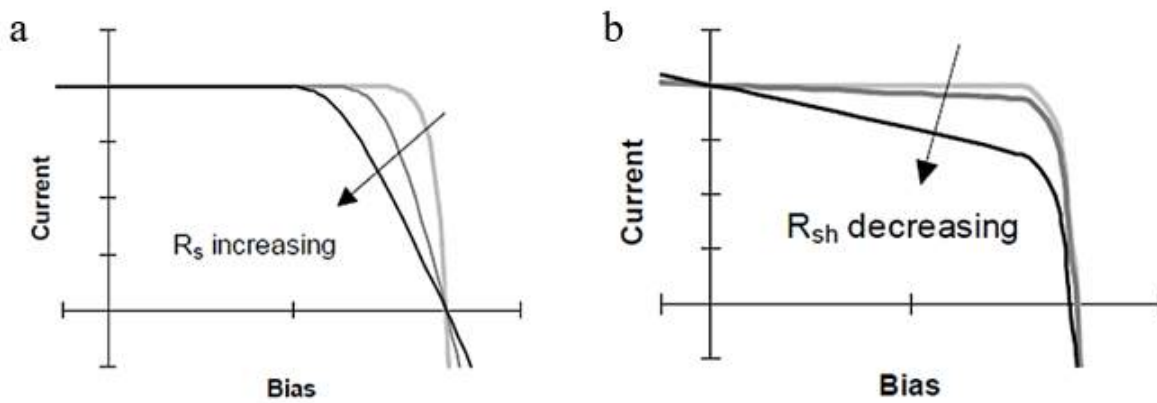
Figure 2.2.5 Effect of (a) increasing series and (b) reducing parallel resistances.

Chapter 3. Development of New Sequential Process for Production of High Quality FAPbI₃ Films: Intramolecular Exchange Process System (IEPs)

3.1 Introduction

The continuous development of high quality film forming methods[49-51] and perovskite composite technologies[11, 33, 34] has led to rapid growth in power conversion efficiency. However, achieving PCE close to the theoretical value (> 30%) still requires the development of new technologies and is an important challenge in making the solar cell industry economically competitive.

Formamidinium lead iodide (FAPbI₃) is a perovskite substance that can potentially provide better performance than methylammonium lead iodide (MAPbI₃) due to the broad absorption of the solar spectrum. In addition, FAPbI₃ with an n-i-p structure (n-plane illuminated with sunlight) exhibits negligible hysteresis in the sweep direction during current-voltage measurements. However, it is more difficult to form a perovskite phase and a high-quality film more stable than MAPbI₃ with FAPbI₃. Therefore, it is important to develop a coating method capable of producing high-quality FAPbI₃ films. Various methodologies such as sequential deposition[49], solvent engineering[50], vapor assisted deposition[52], additive assisted deposition[53, 54], and vacuum deposition[51] have been proposed as methods for making perovskite films. Two-step sequential deposition of these methods is a typical process for producing perovskite films for high-performance PSC. In a sequential deposition process, a thin layer of PbI₂ is deposited on the substrate; Methylammonium iodide (MAI) or formamidine iodide (FAI) is applied to pre-deposited PbI₂ to enable conversion to the perovskite phase. This process involves crystal nucleation and the growth of the perovskite phase by solution or solid state reaction of organic iodides such as PbI₂ and MAI or FAI. However, the sequential reaction of PbI₂ and organic iodide to the inner crystal region from the surface of PbI₂ was not effective in producing high-performance perovskite films with thicknesses exceeding 500 nm. Problems such as the incomplete conversion of PbI₂, peeling of the perovskite film in the solution, and uncontrolled surface roughness. This means that more sophisticated deposition techniques are needed to produce high quality thick FAPbI₃ films (> 500 nm) that allow sufficient absorption up to a wavelength of 840 nm.

The proposed IEPs has a conceptual advance for the formation of inorganic-organic hybrid crystalline perovskite materials. In this study, the proposed intramolecular exchanging crystallization is conceptually different from the retardation approach. The exchange instantaneously occurs and results in compact, uniform, and highly crystalline perovskite film with preferred orientation.

In contrast to the conventional processes, the stimulated reaction gives important advantages to make thick perovskite film without unreacted phase and the exchanging process gives small volume change, resulting in high-quality inorganic-organic perovskite film.

3.2 Results & Discussion

PbI$_2$(DMSO) complex powder was prepared for the intramolecular exchange method. First, toluene was poured as a non-solvent into 1.0 M PbI$_2$ dissolved in DMSO to obtain a precipitate. The x-ray diffraction (XRD) spectrum of the precipitate produced is shown in Figure 3.2.1a. Figure 3.2.2 shows that the precipitate is a crystalline PbI$_2$(DMSO)$_2$ complex without any secondary phase according to the simulated powder XRD data based on the PbI$_2$(DMSO)$_2$ single crystal analysis. The prepared PbI$_2$(DMSO)$_2$ was subjected to vacuum annealing at 60 °C for 24 hours to obtain another powder. A completely different XRD pattern of the vacuum annealed powder in Figure 3.2.1b indicates that vacuum annealing converts the crystalline PbI$_2$(DMSO)$_2$ to another crystalline form. The composition of the other crystalline forms could be estimated to be PbI$_2$(DMSO) based on elemental analysis (EA) results that the atomic percentages of C, H, and S were reduced by half after vacuum annealing. The elemental analysis (EA) results are shown in table 1. The DMSO content of the vacuum-annealed PbI$_2$(DMSO) complex was checked by elemental analysis (EA), which yielded H = 1.0% (1.1%) and C = 4.1% (4.4%), where the values expressed in parenthesis indicate the theoretical mass percent for a given element for C$_2$H$_6$SOPbI$_2$. The thermal stability of PbI$_2$(DMSO) complex was confirmed by TG analysis. Figure 3.2.3 shows a first phase change at around 70-80 ℃. It is expected that the PbI$_2$(DMSO) complex will become PbI$_2$.

PbI$_2$(DMSO) complex was dissolved in dimethylformamide (DMF) solution to form a film by spin coating. The XRD results for films coated on a fused silica substrate are shown in Figure 3.2.4. The XRD pattern of the film shows that it is formed consistent with the XRD pattern of the PbI$_2$(DMSO) complex powder. It can be seen that the thermodynamically stable PbI$_2$(DMSO) complex has no problem in thin film formation even under solvent-evaporation conditions during spin coating. In addition, the coated PbI$_2$(DMSO) complex film has a flat, dense surface as in the FESEM image of Figure 3.2.5.

A sequential reaction such as an inter-diffusion between FAI / MAI and PbI$_2$ through thermal annealing in organic iodide / PbI$_2$ multilayer film has been conventionally employed to form perovskite FAPbI$_3$ or MAPbI$_3$ films from inorganic PbI$_2$ film. However, the conventional methods have problems such as low uniformity of reaction and the existence of unreacted regions. I tried to overcome these problems. As a result, the formation of the perovskite film by the film of the newly prepared PbI$_2$(DMSO) complex gave meaningful observations with significantly different behavior compared to the formation of the perovskite film on the conventional PbI$_2$ film.

To investigate behavior to form into perovskite film, 400 μl of a 0.63 M FAI solution in IPA was spin-coated on top of the PbI$_2$(DMSO) complex film and the annealed PbI$_2$ film on a fused silica substrate.

The major difference between the conventional method using an annealed PbI$_2$ film and the intramolecular exchange process (IEP) using a PbI$_2$(DMSO) composite film is when the perovskite

crystal is formed. Figure 3.2.6 shows a process diagram of the conventional method and the IEP method. Conventional methods use a sequential reaction such as inter-diffusion between FAI / MAI and PbI_2 through thermal annealing in an organic iodide / PbI_2 multilayer to form a perovskite $FAPbI_3$ or $MAPbI_3$ film, while in the case of the IEP method, A perovskite $FAPbI_3$ or $MAPbI_3$ film is formed during the spin coating of the organic iodide. This reaction process can be confirmed by XRD analysis before and after heat treatment of each method. Figure 3.2.7 shows the XRD patterns of $FAPbI_3$ powder, as-coated and annealed FAI / PbI_2 (DMSO), and as-coated and annealed FAI / PbI_2 films. The as-coated FAI / PbI_2(DMSO) films show only XRD peaks corresponding to $FAPbI_3$ powder, while as-coated FAI / PbI_2 films show strong peaks of PbI_2 and weak peaks of $FAPbI_3$. According to the XRD results, the reaction between the FAI and PbI_2(DMSO) complexes were completed during spin coating within 1 minute and consequently $FAPbI_3$ perovskite phase formed without the sequential annealing process required for inter-diffusion in the conventional process using PbI_2 film does. After annealing for $FAPbI_3$ crystallization, the $FAPbI_3$ film based on PbI_2 film in the conventional inter-diffusion process produces residual PbI_2 by incomplete reaction, but the excellent reactivity of IEP using PbI_2(DMSO) complex is due to the high-quality perovskite make a film. The XRD patterns of $FAPbI_3$ films derived from PbI_2(DMSO) complex films exhibit dominant (-111) and (-222) diffraction peaks at 13.9 ° and 28.1 °, respectively. IEP leads to a high quality pure $FAPbI_3$-based film with the desired orientation along the [111] axis.

Also, due to this reactive difference, conventional methods and IEP cause differences in volume expansion. Conventional methods induce significant volume expansion in the growth of perovskite crystals. As shown in Table 2, an increase in the thickness of the PbI_2 film to 570 nm due to the reaction with FAI at 290 nm was observed. In contrast, a perovskite film derived from a PbI_2(DMSO) complex film maintains a thickness of 560 nm after reacting with FAI.

The reason for this result is that in the case of the IEP method, the intercalated DMSO molecule in PbI_2 is easily replaced by FAI, which has a high affinity for PbI_2. FAI molecules experience ionic interaction while DMSO participates in Van der Waals interactions. Since the molecular sizes of DMSO and FAI are similar, they do not induce volume expansion.

$$PbI_2(DMSO) + FAI \rightarrow PbI_2\text{-}FAI + DMSO \uparrow (removal)$$
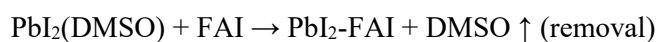
The other mechanism of perovskite formation, IEP, is significant in that it produces high-quality $FAPbI_3$ thin films. A dense perovskite film with a planar surface to demonstrate a high-performance perovskite solar cell is an important requirement that must be satisfied. Figure 3.2.8 shows the FESEM plane-image of films derived from PbI_2(DMSO) complex and PbI_2 films. The $FAPbI_3$ film derived from the PbI_2(DMSO) complex film exhibits a dense, well-developed particle structure of much larger particles than the $FAPbI_3$ film derived from PbI_2.

The optimum thicknesses of the mesoporous mp -TiO_2 and $FAPbI_3$ layers for charge collection and light harvesting in n-i-p heterojunction perovskite solar cells composed of FTO / bl-TiO_2 / mp-TiO_2 / $FAPbI_3$ / PTAA /. As shown in the cross-sectional FESEM image of Figure 3.2.9, I constructed and designed a solar cell consisting of a 100 nm thick mp-TiO_2 layer and a 500 nm-$FAPbI_3$ layer.

Composition engineering, such as A and/or X site replacement of AMX_3 materials, can provide positive results that improve photovoltaic performance and stability. The composition of the films produced through the IEP was controlled by modifying the FAI solution by adding MABr. As a result, a device was fabricated by applying IEP using PbI_2(DMSO) complex film to 10 mol% MABr on mp-TiO_2 / bl-TiO_2 / FTO glass substrate and FAI solution. Figure 3.2.10a shows the J-V curve measured through reverse and forward bias sweeps for one of the best performing solar cells. The device fabricated in this study does not exhibit hysteresis and provides J_{SC}, V_{OC}, and FF from the J-V curve at 24.7 mA / cm^2, 1.06 V and 77.5 %, respectively. This corresponds to a PCE of 20.2 % under standard AM 1.5 conditions. Figure 3.2.10b shows the EQE spectrum and integrated J_{SC} for one of the highest performing solar cells. High J_{SC} values are due to the broad EQE plateau of 85% or more between 400 nm and 780 nm due to the low band gap of $FAPbI_3$ (1.47 eV) and wide light harvesting to a long wavelength of 840 nm. The J_{SC} values of 24.4 mA / cm^2 integrated from EQE were found to be in good agreement with those measured by J-V. It was assumed that the reason for making high-performance solar cells came from high-quality $FAPbI_3$ films with large particles, preferred orientation, and dense, flat surfaces manufactured via IEP. To confirm this assumption, I compare the performance of a device made from a perovskite film derived from a PbI_2(DMSO) complex film and a perovskite film derived from a PbI_2 film in Figure 3.2.11 and show the J-V curve and PCE statistics. Devices made from PbI_2(DMSO) complexes exhibit superior PCE with smaller deviations than conventional PbI_2. The high-performance device, which shows 20.2 % in PCE, was certified as a standardized method in the PV calibration laboratory and identified 20.1 % PEC under AM1.5G full sun (Figure 3.2.12).
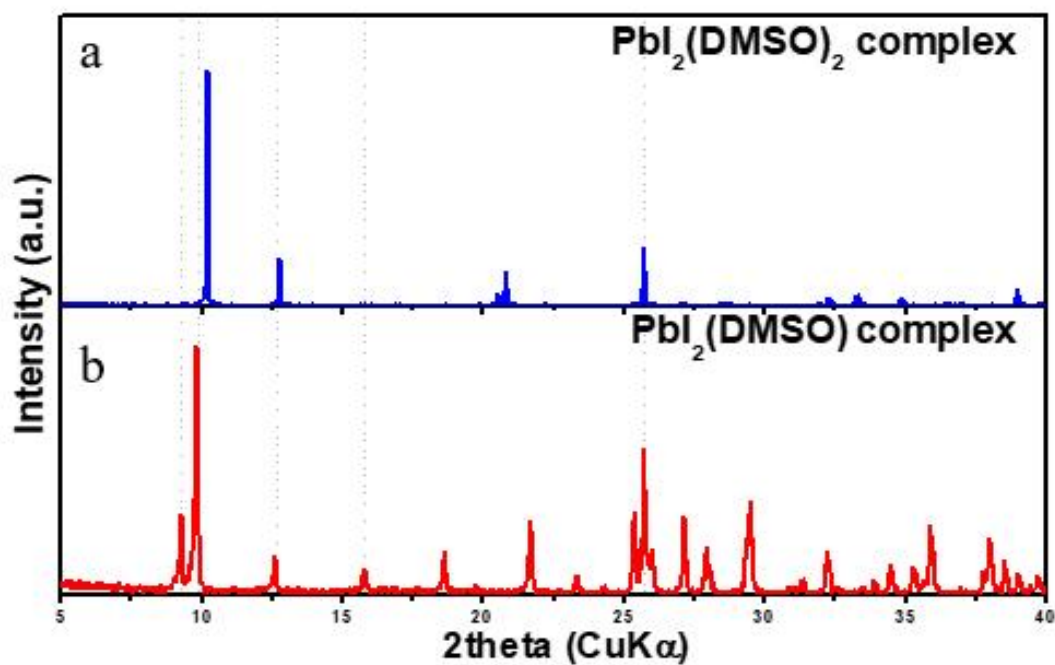
Figure 3.2.1 X-ray diffraction patterns of (a) $PbI_2(DMSO)_2$ complex and (b) $PbI_2(DMSO)$ complex.
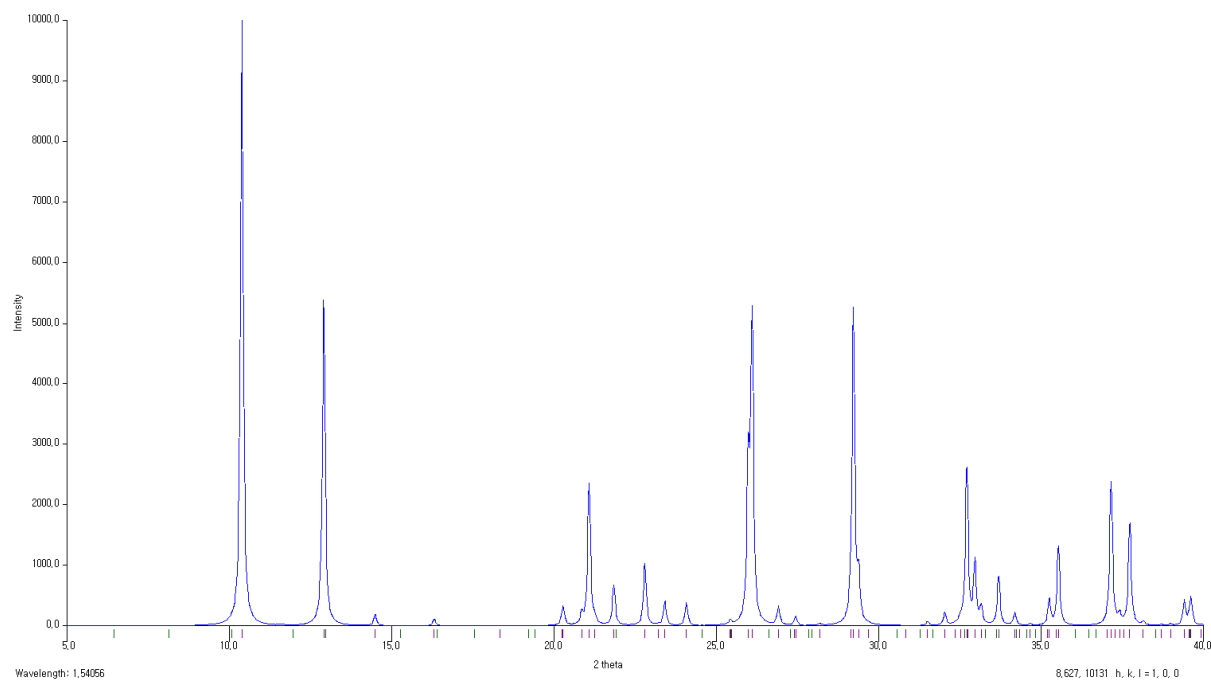
Figure 3.2.2 Theoretical powder XRD pattern of $PbI_2(DMSO)_2$ complex which is simulated by Mercury 3.0 software based on single crystal analysis data.

Analysis item Sample name	C (%)	H (%)	N (%)	S (%)
Y1 [PbI$_2$(DMSO)$_2$]	7.8	2.0	-	6.6
Y2 [PbI$_2$(DMSO)]	4.1	1.0		4.7

Table 1 The elemental analysis (EA) of (a) Y1 [PbI$_2$(DMSO)$_2$] and (b) Y2 [PbI$_2$(DMSO)].
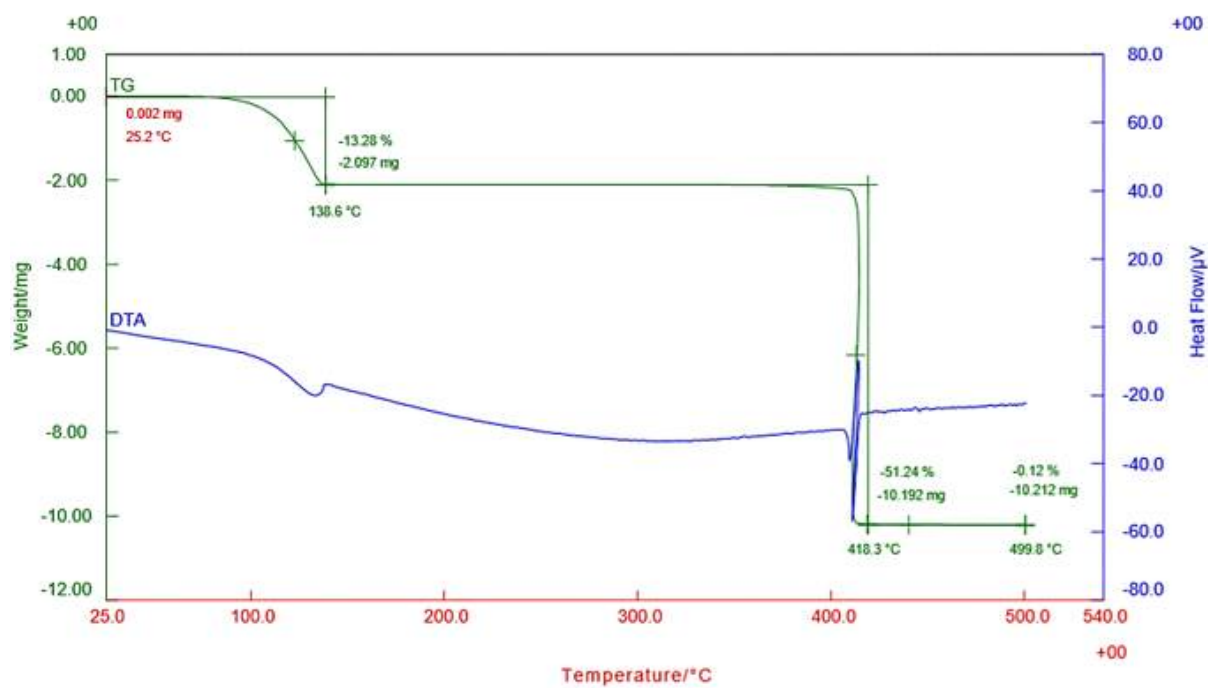
Figure 3.2.3 TG analysis results of PbI$_2$(DMSO) complex.
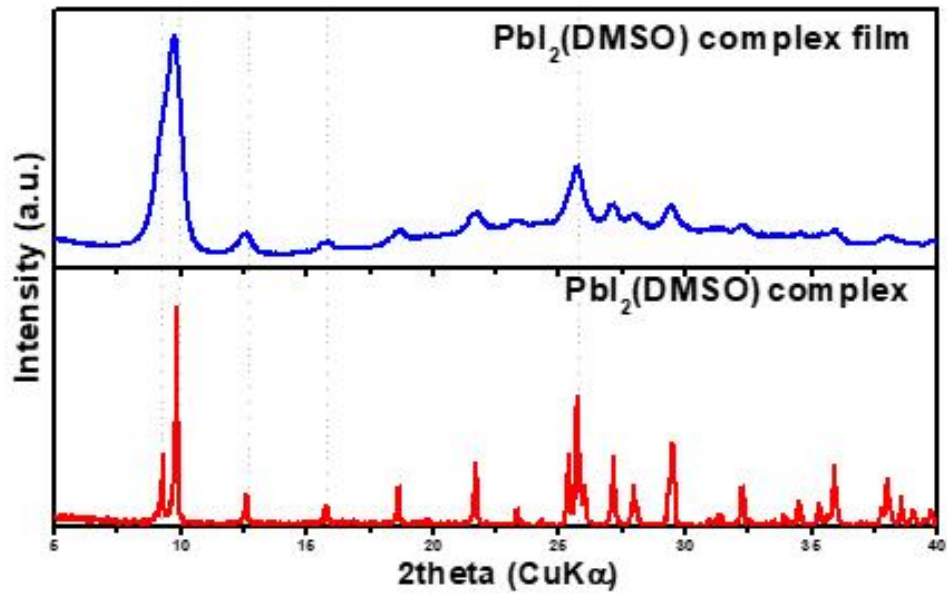
Figure 3.2.4 X-ray diffraction patterns of PbI$_2$(DMSO) complex film.
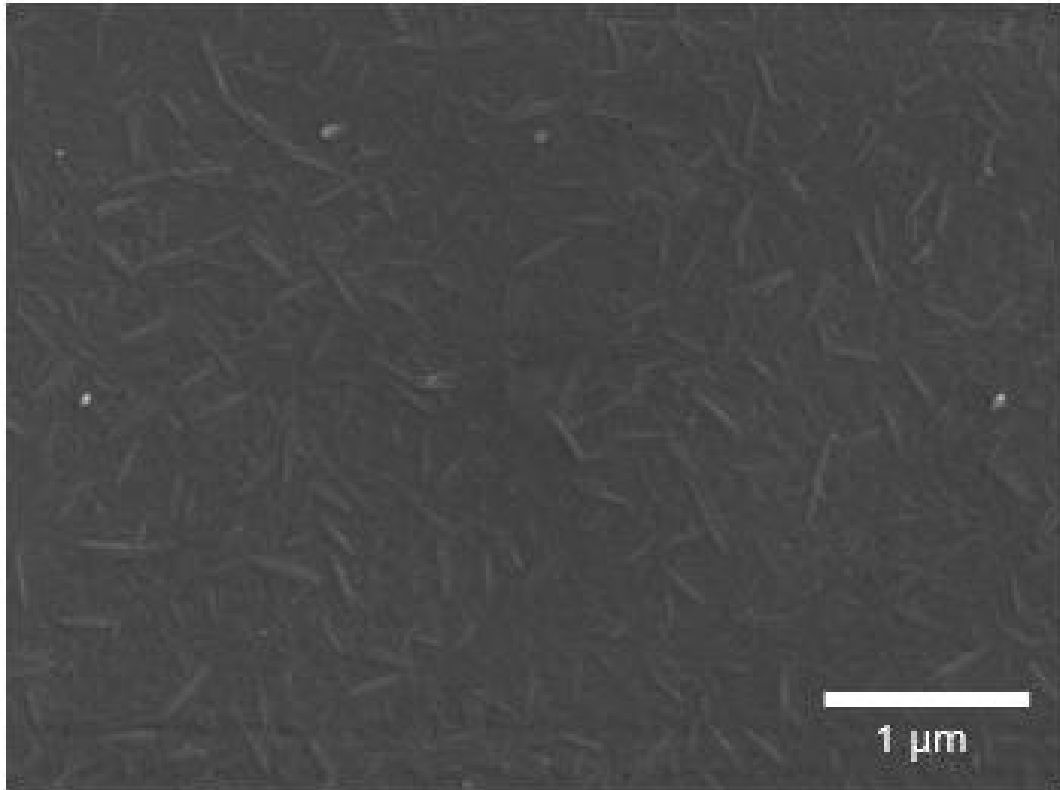
Figure 3.2.5 FESEM image of PbI$_2$(DMSO) complex thin film.
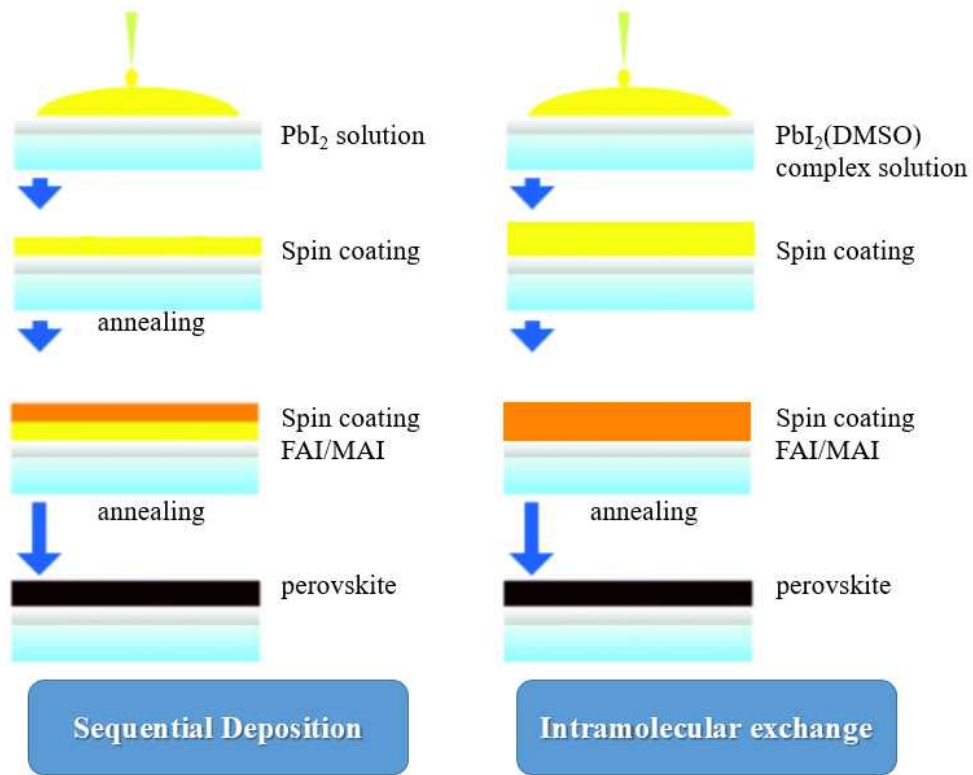
Figure 3.2.6 Process schematic diagram of (left) conventional method and (right) intramolecular exchange process (IEPs).
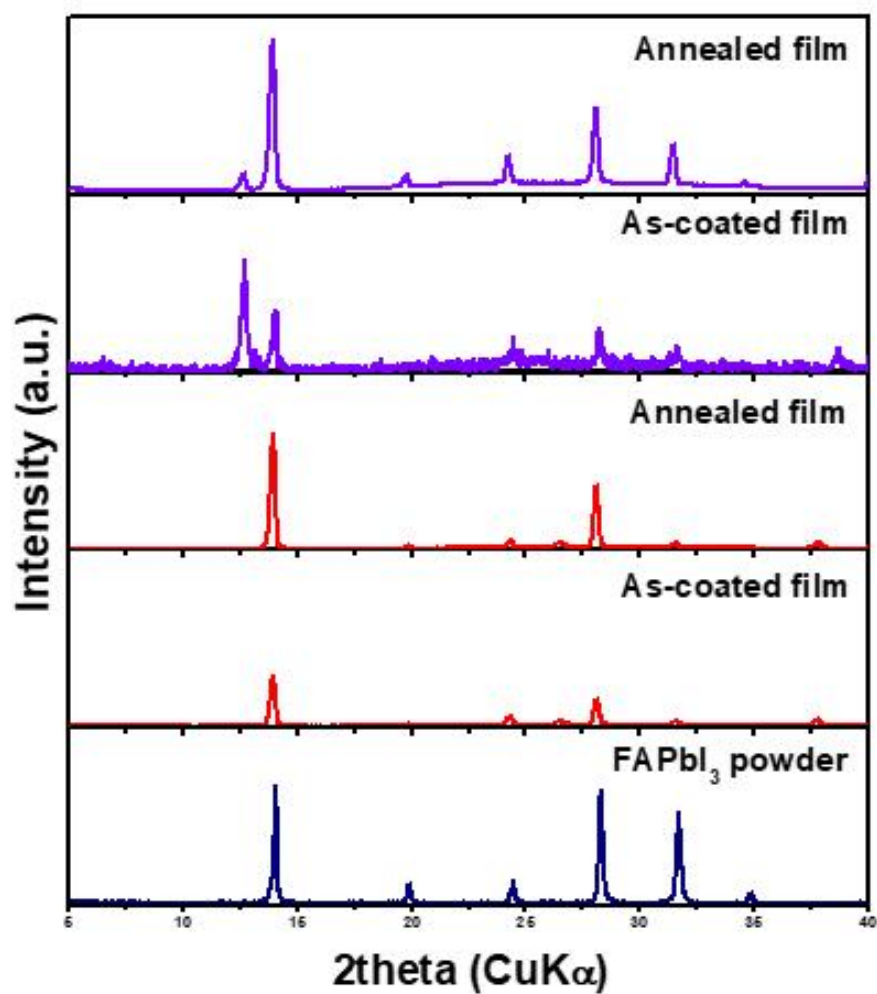
Figure 3.2.7 XRD patterns for FAPbI$_3$ powder, as-coated and annealed films which are prepared by coating of FAI solution on prior PbI$_2$(DMSO) complex (red) and PbI$_2$ films (violet).

	PbI$_2$(DMSO) complex film (IEP)	PbI$_2$ film (Conventional method)
As-coated film	510 nm	290 nm
After FAI deposition and annealing	560 nm	570 nm

Table 2 Thickness of prepared films on fused silica substrate.
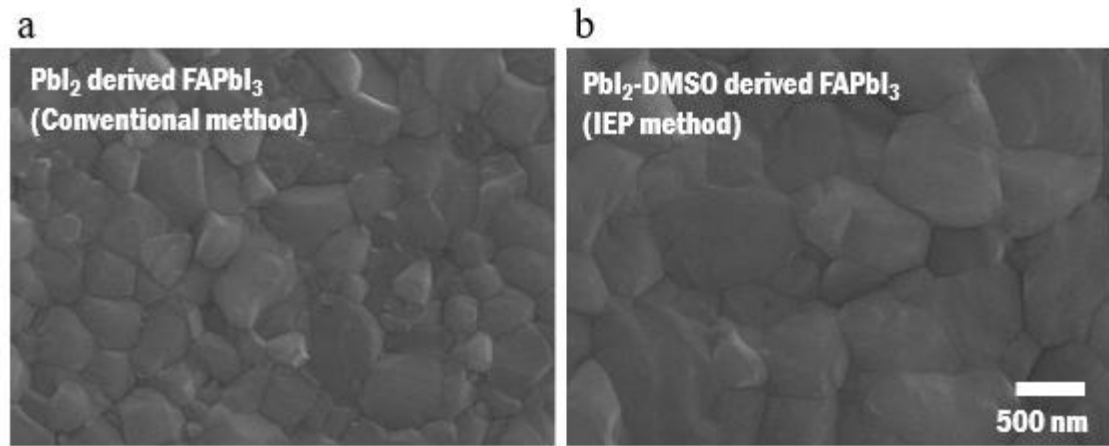
Figure 3.2.8 FESEM images of FAPbI$_3$ thin film derived (a) PbI$_2$ [Conventional method] and (b) PbI$_2$(DMSO) [IEP method].
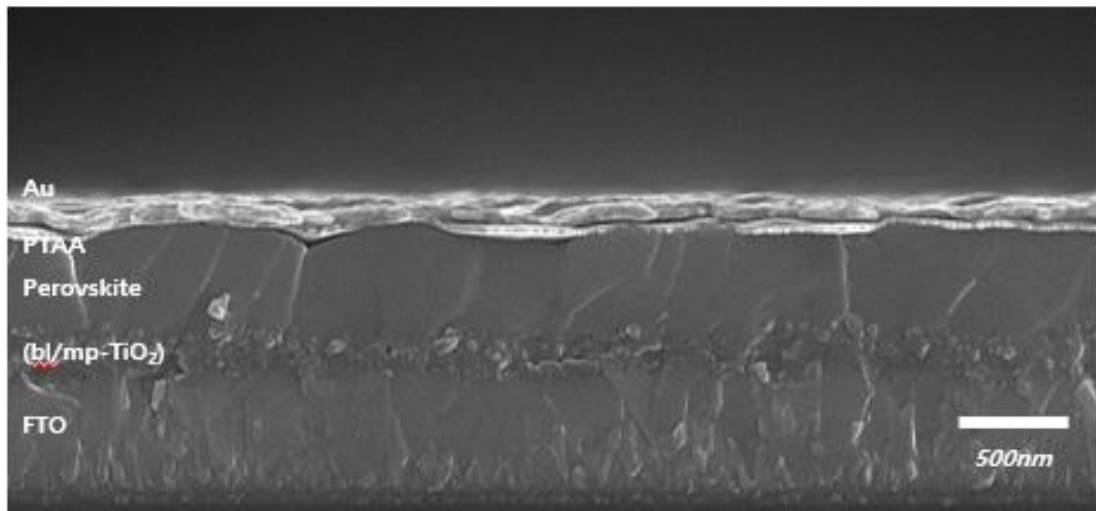
Figure 3.2.9 Cross-sectional FESEM image of the device consisting of FTO-Glass / bl-TiO$_2$ / mp-TiO$_2$ / perovskite / PTAA / Au.
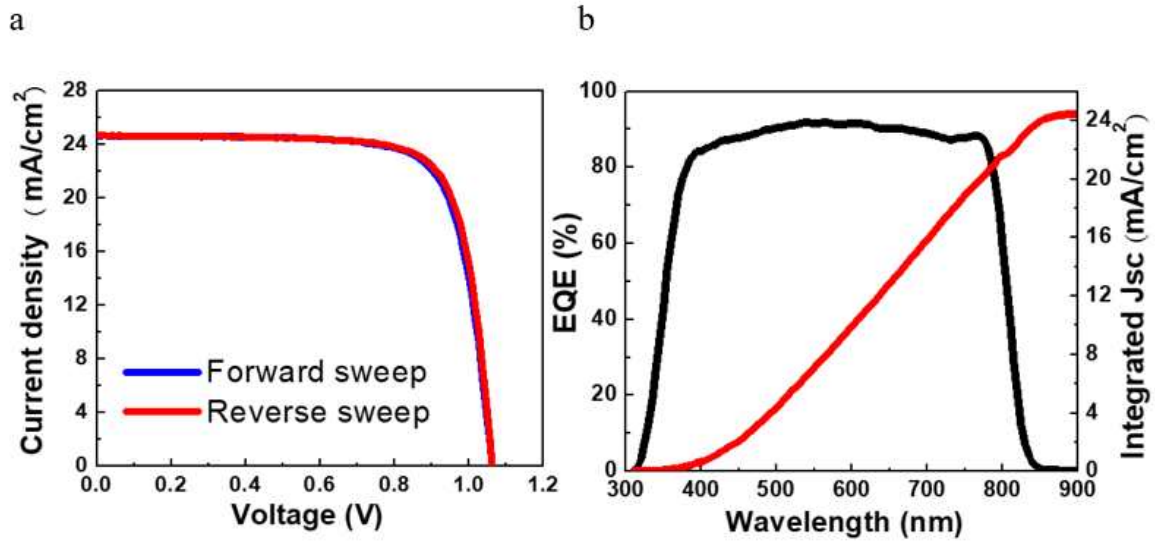
Figure 3.2.10 I-V and EQE measurements (a) J-V curves of best device measured with a 40 ms scanning delay in reverse (from 1.2 V to 0 V) and forward (from 0 V to 1.2 V) modes under standard AM 1.5G illumination, and (b) EQE spectra for best device and integrated $J_{SC.}$
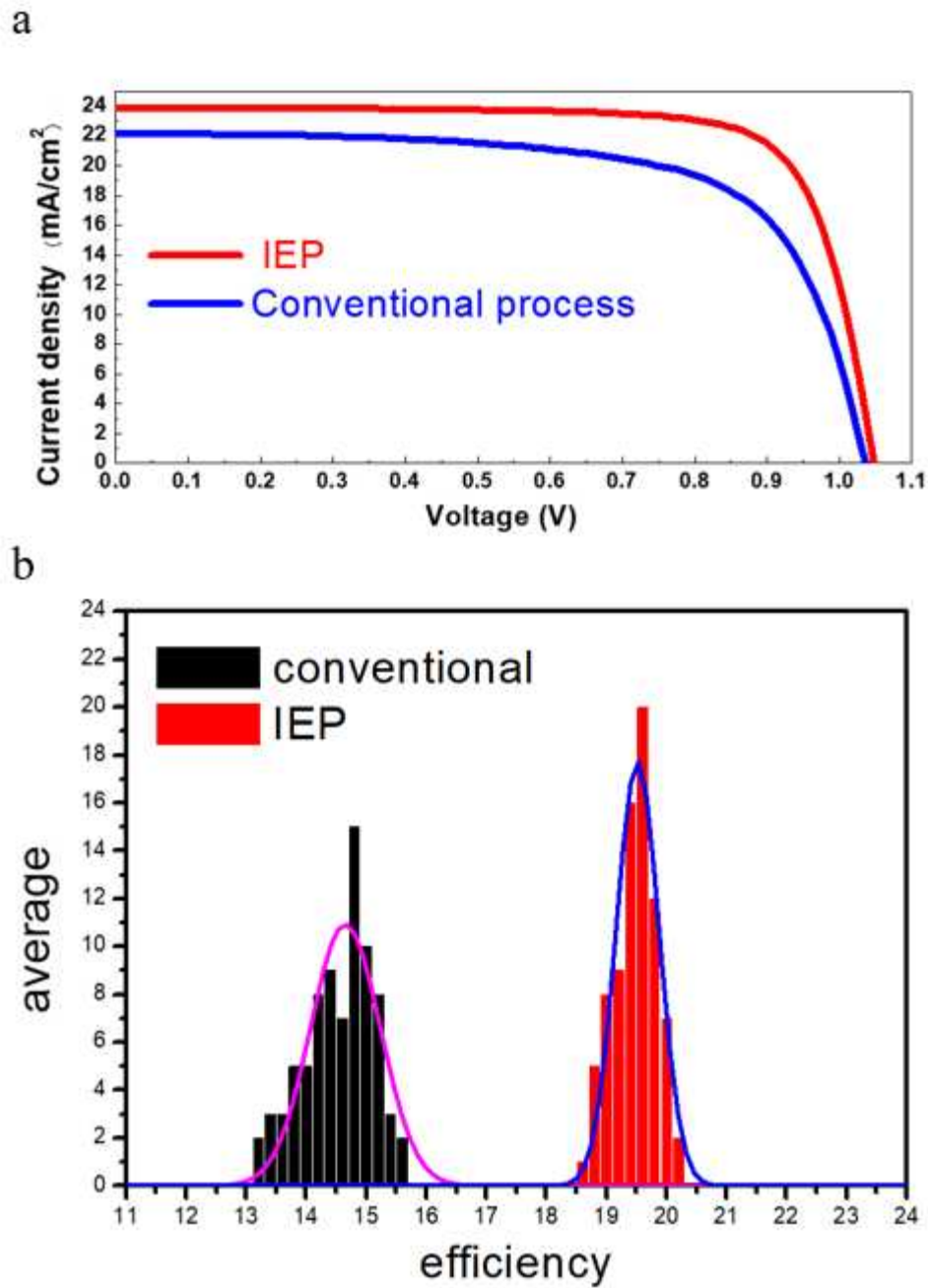
Figure 3.2.11 Performance, and reproducibility between IEP and conventional process

(a) Representative J-V curves for FAPbI$_3$-based cells fabricated by IEP and conventional process

(b) Histogram of solar cell efficiencies for each 66 FAPbI$_3$-based cells fabricated by IEP and conventional process.
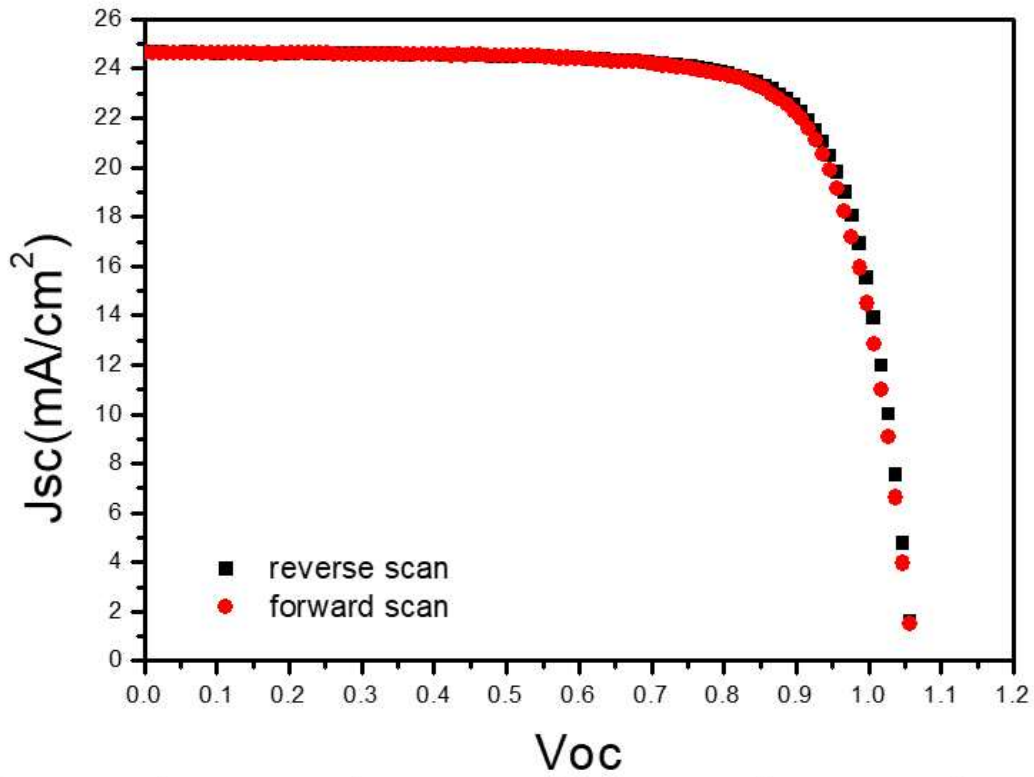
	Jsc (mA/cm²)	Voc (V)	FF	PCE (%)	Rseries
Reverse	24.7	1.06	77.5	20.2	30.81
forward	24.6	1.06	76.7	20.0	37.48

Figure 3.2.12 Highly performing devices exhibiting 20.2% in PCE was certified by the standardized method in the PV calibration laboratory.

3.3 Conclusion

In this work, I report on the synthesis of a $PbI_2(DMSO)$ precursor with excellent capabilities for molecular exchange with FAI at low temperatures during the spinning process, as well as the fabrication of highly efficient $FAPbI_3$-based PSCs with certified PCEs exceeding 20 %. To synthesize the $PbI_2(DMSO)$ precursors, precipitates were obtained by pouring toluene as a non-solvent into 1.0 M PbI_2 solution dissolved in DMSO. The as-prepared $PbI_2(DMSO)_2$ was then annealed at 60 ºC for 24 h in vacuum to obtain $PbI_2(DMSO)$ by removal of 1 mole DMSO. The XRD pattern of the vacuum-annealed powder did not match that of $PbI_2(DMSO)_2$, implying that the $PbI_2(DMSO)_2$ transformed into a different phase by releasing some DMSO molecules. The content of DMSO in the as-annealed powder was estimated by thermogravimetric analysis (TGA). The DMSO content of the vacuum-annealed $PbI_2(DMSO)$ complex was checked by elemental analysis (EA), which yielded H = 1.0% (1.1%) and C = 4.1% (4.4%), where the values expressed in parenthesis indicate the theoretical mass percent for a given element for $C_2H_6SOPbI_2$.

I first confirmed that the $PbI_2(DMSO)$ phase was retained even after spin-coating with the $PbI_2(DMSO)$ precursor dissolved in DMF. The XRD pattern for film coated on a fused silica substrate was compared with that of the initial precursor. The XRD pattern for the as-coated film was consistent with that of the $PbI_2(DMSO)$ complex powder, although its crystallinity is lowered. The as-coated $PbI_2(DMSO)$ film had a flat and dense surface, as shown in the field-emission scanning electron microscopy (FESEM) image.

To fabricate $FAPbI_3$-based PSCs through IEP between DMSO and FAI (MABr) using pre-deposited $PbI_2(DMSO)$ layers and an FAI (MABr) solution. The $FAPbI_3$ film derived from $PbI_2(DMSO)$ exhibited a dense and well-developed grain structure with larger grains. I deposited $FAPbI_3$–based layers with a thickness of ~ 500 nm, and fabricated devices consisting of fluorine-doped tin oxide (FTO)-glass/barrier layer (bl)-TiO_2/mesoporous (mp)-TiO_2/perovskite/poly-triarylamine(PTAA)/Au. The current density-voltage (J-V) curves of the fabricated cells with $FAPbI_3$-based layers were measured under a standard air mass 1.5 global (AM 1.5G) illumination and the external quantum efficiency (EQE) spectra were measured. The J–V curves measured via reverse and forward bias sweep for one of the best-performing solar cell. The devices I fabricated also showed no hysteresis. J_{SC}, V_{OC}, and FF determined from the J–V curves were 24.7 mA / cm^2, 1.06 V, and 77.5 %, respectively, and correspond to a PCE of 20.2 % under standard AM 1.5G illumination.

The devices based on $FAPbI_3$ fabricated from $PbI_2(DMSO)$ showed superior PCEs with smaller deviations in the value, compared to those prepared from conventional PbI_2 films. High-efficiency solar cells with average PCEs of over 19% could be produced with a high degree of reproducibility by using the IEP. This study provides an effective protocol for fabricating efficient and cost-effective inorganic-organic hybrid heterojunction solar cells.

3.4 Experimental

Materials

Unless stated otherwise, all materials were purchased from Sigma-Aldrich or Junsei Organics and used as received. Poy(triarylamine) (PTAA) was purchased from EM Index.

Synthesis of Inorganic / Organic Halide Materials

$NH_2CH=NH_2I$ (FAI) was synthesized by reacting 30 mL hydroiodic acid (57% in water, Aldrich) and 15 g formamidine acetate (Aldrich) in a 250 mL round-bottomed flask at 0 °C for 2 h with stirring. Similarly, CH_3NH_3Br (MABr) was synthesized by reacting 27.86 mL CH_3NH_2 (40% in methanol, Junsei Chemical) and 44 mL hydrobromic acid (48 wt% in water, Aldrich) in a 250 mL round-bottom flask at 0 °C for 4 h with stirring. The precipitates were recovered by evaporating the solutions at 50 °C for 1 h. The products were dissolved in ethanol, recrystallized from diethyl ether, and finally dried at 60 °C in a vacuum oven for 24 h.

For preparation of $PbI_2(DMSO)_2$ complex, PbI_2(50 g) was dissolved in dimethylsulfoxide (DMSO) of 150 ml at 60 °C and then toluene of 350 ml was slowly added into the PbI_2 solution. Then produced white precipitation was filtered and dried for 3 h at room temperature. The PbI_2(DMSO) complex was obtained by annealing $PbI_2(DMSO)_2$ for 24 h in vacuum oven at 60 °C.

Solar Cell Fabrication

TiO₂ Substrate

A dense blocking layer of TiO_2 (60 nm, bl-TiO_2) was deposited onto a F-doped SnO_2 (FTO, Pilkington, TEC8) substrate by spray pyrolysis using a 20 mM titanium diisopropoxide bis(acetylacetonate) solution (Aldrich) at 450 °C; this was done to prevent a direct contact between FTO and the hole-conducting layer. A 150-nm thick mesoporous (mp) TiO_2 was spin-coated onto the bl-TiO_2/FTO substrate using diluted TiO_2 paste and calcinated at 500 °C for 1 h in air to remove the organic components.

Perovskite Film [PbI₂(DMSO) Complex]

1.30 M PbI_2(DMSO) complex solution in N,N-Dimethylformamide (DMF) was prepared at 70 °C. The PbI_2(DMSO) complex solution was spin-coated on mp-TiO_2 substrate at 3000 rpm for 30 seconds, and transparent PbI_2(DMSO) film was obtained. Then 465 mM FAI solution in 2-propanol was spin-coated on top of the transparent PbI_2(DMSO) film at 5000 rpm for 30 sec. The films changed to dark brown in color during spin-coating and the films were dried on a hot plate at 150 °C for 20 min.

($FAPbI_3$)$_{1-x}$($MAPbBr_3$)$_x$ films were prepared by same procedure using FAI solution added MABr.

HTM & Au Counter Electrode

A polytriarylamine (PTAA) (EM index, Mn = 17,500 g/mol)/toluene (10 mg/1mL) solution with an additive of 7.5 µl Li-bis(trifluoromethanesulfonyl) imide (Li-TFSI)/acetonitrile (170 mg/1 mL) and 4 µl 4-*tert*-butylpyridine (TBP) was spin-coated on the perovskite layer/mp-TiO_2/bl-TiO_2/FTO substrate at 3000 rpm for 30 s. Finally, an Au counter electrode was deposited by thermal evaporation; the active area of this electrode was fixed at 0.16 cm^2.

Characterization

The X-ray diffraction (XRD) spectra of the prepared films were measured using a Rigaku SmartLab X-ray diffractometer; the in situ XRD experiment of the as-prepared $FAPbI_3$ yellow powder was performed using a Rigaku Ultima IV with an X-ray tube (Cu Kα, λ=1.5406Å). Ultraviolet visible absorption spectra were recorded on a Shimadzu UV 2550 spectrophotometer in the 300–800 nm wavelength range at room temperature. The morphology of the films was observed using a field-emission scanning electron microscope (MIRA3 LMU, Tescan). Thermal gravity (TG) and differential scanning calorimetric (DSC) analyses of the as-prepared powders were performed with a heating rate of 2 ºC/min from RT up to 300 ºC under nitrogen atmosphere using TA Instruments SDT 2960 and DSC 2910, respectively. External quantum efficiency (EQE) was measured by a power source (Newport 300W Xenon lamp, 66920) with a monochromator (Newport Cornerstone 260) and a multimeter (Keithley2001). The *J–V* curves were measured using a solar simulator (Newport, Oriel Class A, 91195A) with a source meter (Keithley 2420) at 100 mA/cm^2 illumination AM 1.5 G and a calibrated Si-reference cell certificated by NREL. The *J-V* curves were measured by reverse (forward bias (1.2 V) → short circuit (0 V)) or forward (short circuit (0 V) → forward bias (1.2 V)) scan. The step voltage was fixed at 10 mV and the delay time, which is a delay set at each voltage step before measuring each current, was modulated. The *J–V* curves for all devices were measured by masking the active area with a metal mask (area of 0.094 cm^2).

Chapter 4. Material Control to Create Perovskite Film for Increased Quality and Grain Size

4.1 Introduction

Unlike conventional organic thin films, perovskite thin films are very difficult to form a uniform and dense thin films. Perovskite materials exhibit various thin film morphologies due to their rapid reaction and self-assembly properties. To overcome these problems, various coating methods and methods of controlling crystallization have been studied. These attempts ultimately have the directionality to increase the collection probability by preventing recombination of electron-hole pairs generated by light, while minimizing optical loss and thermal loss. In order to improve the optical-cell-physical properties such as light collection, electron transport, and electron diffusion, it is important to control a thin film shape having a uniform and large crystal grains and having few defects.

Improving the crystallization and grain size of the perovskite absorber is important for increased device efficiency[55, 56].

Since defects in the grain boundaries and crystal grains act as traps that dissipate electrons and holes during transport, they cause a decrease in efficiency. Therefore, the grain size of the absorber layer is advantageous for device performance as the size increases without internal defects. The microstructural control for micron-sized grains results in intense photoluminescence and improved photovoltaic performance in polycrystalline perovskite thin films[57-60].

The crystallization speed of the perovskite can be controlled to adjust the growth and formation of the film. And the rate of crystallization speed is affected by nucleation. Generally, nucleation and film growth depends on various factors such as deposition temperature, choice of solvent, precursor composition, solution concentration, and interfacial energy. There are several factors in the IEPs to increase efficiency through the crystallization of the perovskite film and the improvement of the particle size.

4.2 Results & Discussion

Several conditions of IEPs were controlled to form high-quality perovskite films. The crystallization and grain size of the perovskite film was observed for each condition and the photoelectric conversion efficiency of the solar cell was compared.

4.2.1 The MACl Additive Introduced into the Perovskite Composition

The role of MACl in perovskite solar cells has an interesting and effective impact on device performance improvement. During the annealing process, MACl is mostly dissipated from the film through sublimation and decomposition. The Cl^- remaining in the final film is mainly observed at grain boundaries. It has been reported that the maximum amount of Cl that can be incorporated into perovskite films is limited to < at 4 % (chlorine vs. iodine) due to the considerable difference in ion radius[61]. Despite the presence of small amounts in the perovskite film, the incorporation of Cl^- significantly improved the performance of the perovskite solar cell[62]. In the microstructure, Cl^- has a great influence on the formation process of the perovskite film. In addition, intermediate steps involving Cl^- contribute to improved coverage by slowing down the reaction rate. Although it is well known that Cl^- produces large particles in the perovskite monolayer, a mechanistic study showing the correlation between the detailed role of Cl in film growth kinetics and the increased particle size, crystallinity, and Cl^- concentration in the film still not enough.

Perovskite film was formed by adding 0 ~ 10 mg of MACl material to the secondary coating solution of IEPs. The crystallinity of the prepared perovskite films was compared by XRD analysis. As shown in Figure 4.2.1a, the intensity of the diffraction peaks at 13.9 ° (110) and 28.1 ° (220) increases significantly with the content of MACl. This clearly demonstrates that the presence of MACl in IEPs was involved in the crystallization of perovskite films. In addition, XRD analysis of the 150 °C anneals over time under the condition of adding 10 mg of MACl showed that the intensity was increased up to 30 minutes and then maintained (Figure 4.2.1b).

The morphology change and particle growth of perovskite film by MACl effect and annealing effect were confirmed by SEM image. As can be seen in Figure 4.2.2a, it can be observed that the grain size can be increased to more than 1um as the addition of MACl increases up to 10 mg. In addition, the grain size of perovskite film increased by about 2 times according to the heat treatment time under the condition of adding 10 mg of MACl (Figure 4.2.2b). In the case of ordinary perovskite films, grain size increases with the change in heat treatment conditions. However, cannot observe dramatic changes such as grain size change due to the addition of MACl.

Figure 4.2.3 shows the J-V characteristics of a perovskite solar cell (with the detailed photovoltaic parameters in Table 3). The 10 mg MACl added to the secondary coating solution greatly improves the

short-circuit current (Jsc) and the fill factor (FF) to achieve 20.8% power conversion efficiency. As the content of MACl increased from 0 to 10 mg, the series resistance (Rs) of the device decreased. The short-circuit current (Jsc) and the fill factor (FF) are improved by reducing the series resistance.
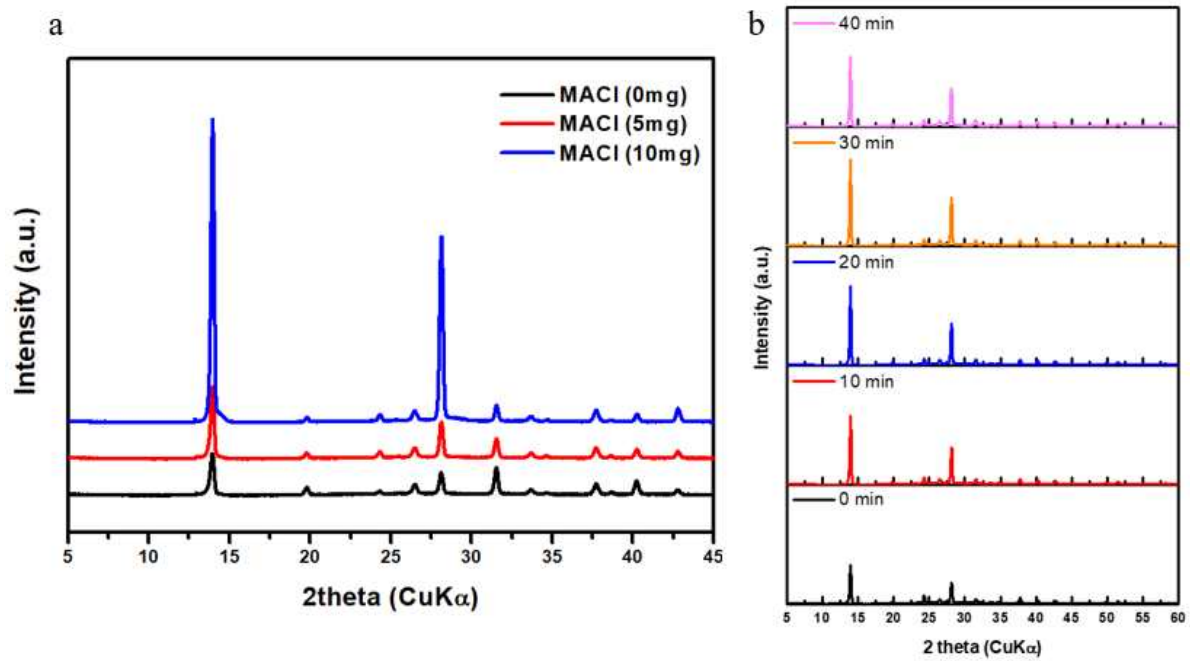
Figure 4.2.1 X-ray diffraction patterns of (a) the amount of MACl (b) heat-treatment time (Under MACl 10mg and 150 °C heat treatment conditions).
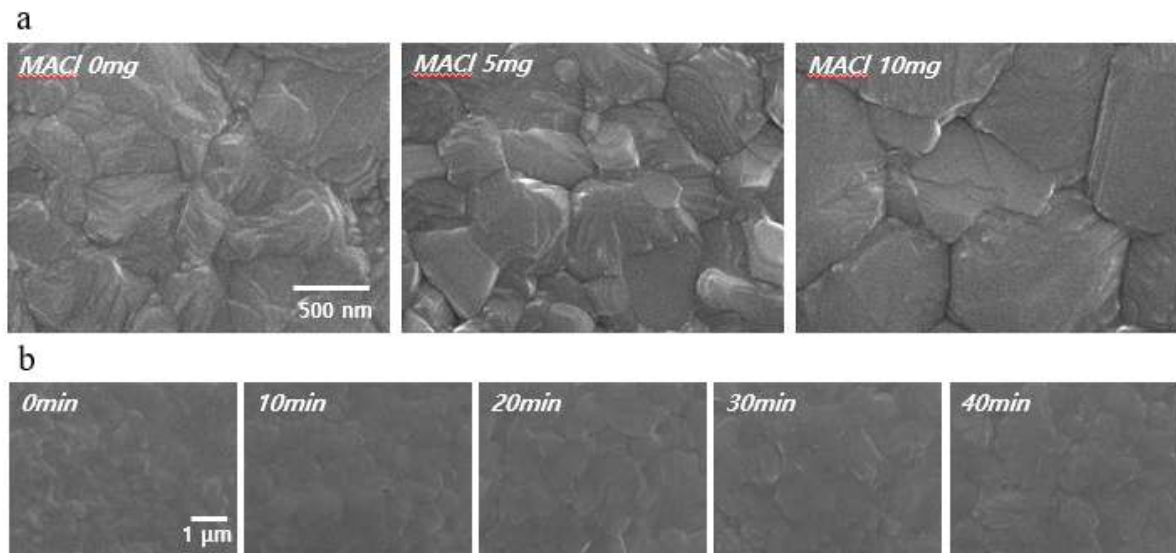
Figure 4.2.2 FESEM images of (a) grain size changes according to MACl content and (b) grain size changes according to heat treatment time in FAPbI$_3$ thin film (Under MACl 10mg and 150 °C heat treatment conditions).
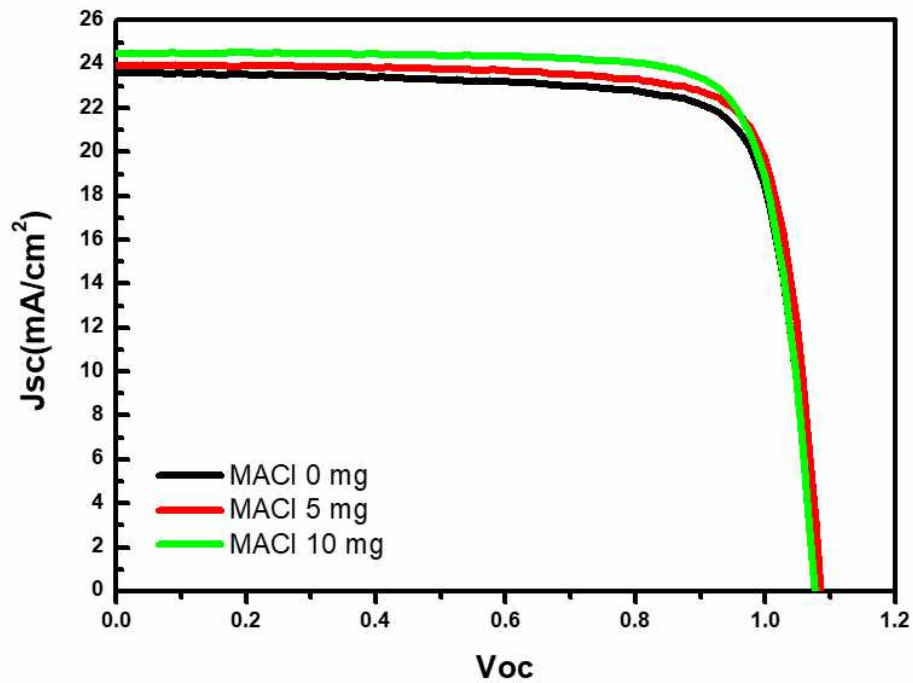
Figure 4.2.3 J-V characteristics as the MACl amount changes from 0 to 10 mg.

	Jsc (mA/cm²)	Voc (V)	FF	PCE (%)	Rseries(ohm)
MACl 0 mg	23.6	1.07	79.7	20.3	26.39
MACl 5 mg	24.0	1.08	80.3	20.9	25.51
MACl 10 mg	24.5	1.07	80.7	21.3	24.20

Table 3 Photovoltaic parameters of the solar cells (This data is the average efficiency of the device).

4.2.2 PbI$_2$ Purification and FAI Concentration Effect

The purity of PbI$_2$ and FAI materials, precursors of FAPbI$_3$ perovskite films, is important for making high-quality films. In particular, the PbI$_2$ film that is first coated in the sequential process changes the state of the film depending on the state of the PbI$_2$ precursor and greatly affects the quality of the final perovskite film.

Figure 4.2.4 shows the results of SEM observation of the surface of the perovskite film produced after the secondary reaction through the film surface and the PbI$_2$ film according to the type of PbI$_2$. Three types of PbI$_2$ materials were used. Figure 4.3.4a shows a PbI$_2$ product obtained by dissolving a commercial PbI$_2$ product in DMF and precipitating with toluene. As can be seen, it can be seen that a very dense PbI$_2$ film is formed and it can be observed that the perovskite film is formed at high quality after the second reaction. Figure 4.3.4b shows a PbI$_2$ film using alfa aesar's PbI$_2$ product. Small pores formed in the PbI$_2$ film were observed. The disadvantages of such primary films have adversely affected the morphology of the finished perovskite film. The PbI$_2$ film in Figure 4.3.4c showed a worse shape than the two films in the front. This phenomenon is expected to be closely related to the purity of the PbI$_2$ material.

The purity of the PbI$_2$ material affects nucleation for the secondary reaction of FAI and affects the rate of crystallization. As evidence for this, it was confirmed that the rate of conversion to the black phase differs for each PbI$_2$ film during the heat treatment for perovskite formation. Table 4 shows the photovoltaic conversion efficiencies of the solar cells fabricated using the respective perovskite films. The grain size and surface roughness of the perovskite affected the photovoltaic conversion efficiency through the change of the fill factor (FF) and Voc, and also caused the hysteresis phenomenon.

FAPbI$_3$ films prepared through IEPs showed grain size changes according to the conditions of FAI concentration. Figure 4.2.5 shows the surface change of the perovskite film according to the FAI solution concentration for the secondary coating. As the concentration of FAI solution increases, grain size increases. The change in FAI concentration affects the nucleation process and the rate of crystallization. Also, the proper concentration of FAI for sufficient reaction to form FAPbI$_3$ film is important.
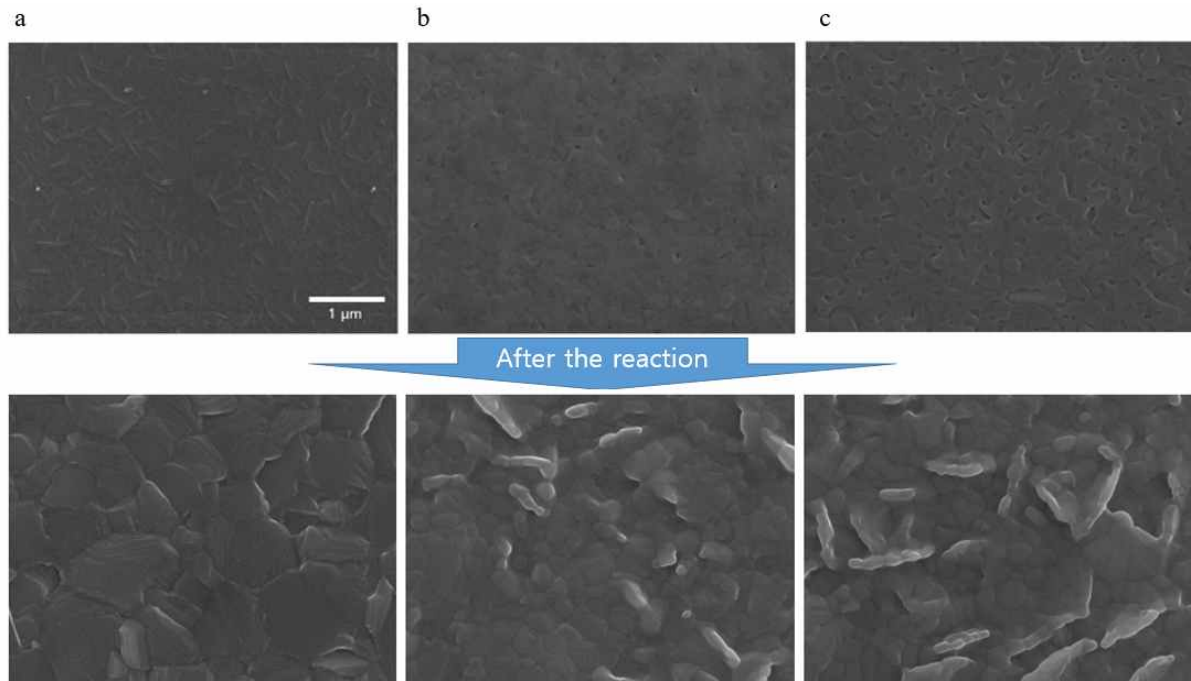
Figure 4.2.4 FESEM images of of PbI_2 film and $FAPbI_3$ film depending on the type of PbI_2 material: (a) PbI_2 product obtained by dissolving a commercial PbI_2 product in DMF and precipitating with toluene, (b) alfa aesar's PbI_2 products, and (c) third-party PbI_2 products.

	Jsc (mA/cm^2)	Voc (V)	FF	PCE (%)	Rseries
re. scan - PbI$_2$ (a)	23.8	1.1	80.9	21.1	29.57
fo. scan	23.8	1.08	80.3	20.6	34.15
re. scan - PbI$_2$ (b)	23.7	1.09	76.8	19.8	26.35
fo. scan	23.6	1.05	67.1	16.6	46.41
re. scan - PbI$_2$ (c)	23.4	1.03	59.5	14.5	43.23
fo. scan	23.4	0.93	44.0	9.6	127.51

Table 4 Power conversion effect of a device on $FAPbI_3$ film made according to PbI_2 type.
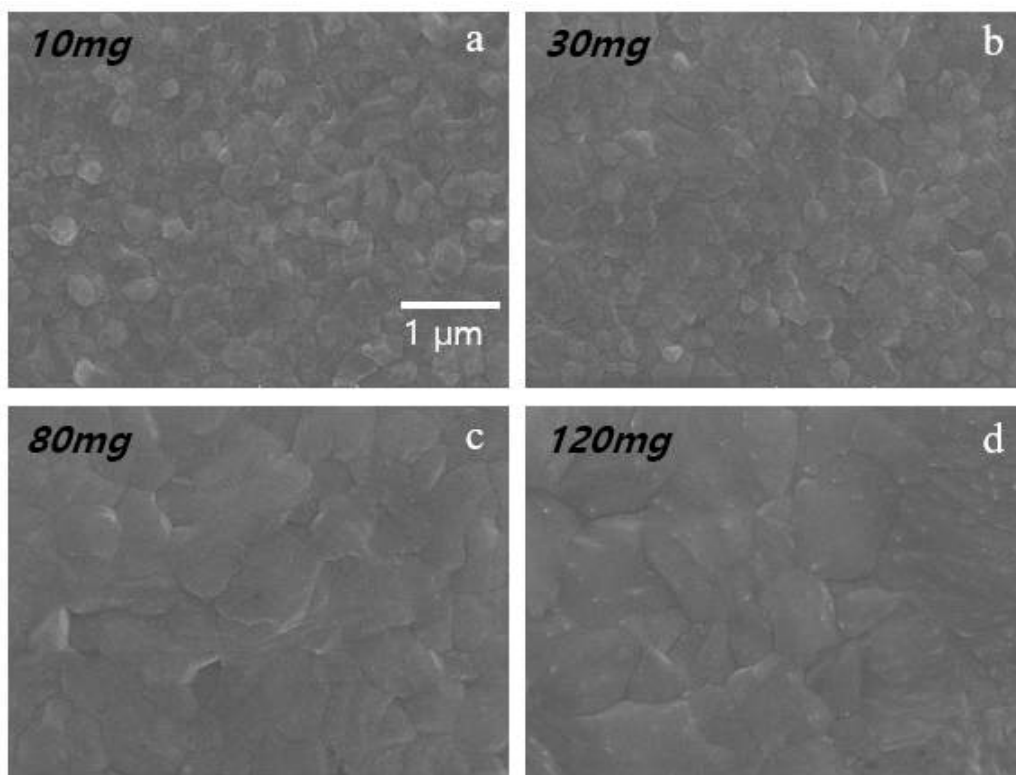
Figure 4.2.5 FESEM images of perovskite layer morphology as FAI content of secondary coating solution changes from 10 mg to 120 mg.

4.3 Experimental

Materials

Unless stated otherwise, all materials were purchased from Sigma-Aldrich or Junsei Organics and used as received. Poy(triarylamine) (PTAA) was purchased from EM Index.

Synthesis of Inorganic / Organic Halide Materials

$NH_2CH=NH_2I$ (FAI) was synthesized by reacting 30 mL hydroiodic acid (57% in water, Aldrich) and 15 g formamidine acetate (Aldrich) in a 250 mL round-bottomed flask at 0 °C for 2 h with stirring. Similarly, CH_3NH_3Br (MABr) was synthesized by reacting 27.86 mL CH_3NH_2 (40% in methanol, Junsei Chemical) and 44 mL hydrobromic acid (48 wt% in water, Aldrich) in a 250 mL round-bottom flask at 0 °C for 4 h with stirring. The precipitates were recovered by evaporating the solutions at 50 °C for 1 h. The products were dissolved in ethanol, recrystallized from diethyl ether, and finally dried at 60 °C in a vacuum oven for 24 h.

For preparation of $PbI_2(DMSO)_2$ complex, PbI_2(50 g) was dissolved in dimethylsulfoxide (DMSO) of 150 ml at 60 °C and then toluene of 350 ml was slowly added into the PbI_2 solution. Then produced white precipitation was filtered and dried for 3 h at room temperature. The PbI_2(DMSO) complex was obtained by annealing $PbI_2(DMSO)_2$ for 24 h in vacuum oven at 60 °C.

Solar Cell Fabrication

TiO$_2$ Substrate

A dense blocking layer of TiO_2 (60 nm, bl-TiO_2) was deposited onto a F-doped SnO_2 (FTO, Pilkington, TEC8) substrate by spray pyrolysis using a 20 mM titanium diisopropoxide bis(acetylacetonate) solution (Aldrich) at 450 °C; this was done to prevent a direct contact between FTO and the hole-conducting layer. A 150-nm thick mesoporous (mp) TiO_2 was spin-coated onto the bl-TiO_2/FTO substrate using diluted TiO_2 paste and calcinated at 500 °C for 1 h in air to remove the organic components.

Perovskite Film [Mixed Solvent]

PbI_2 (1.30 M) containing 2.5 mol% $PbBr_2$ was dissolved in a 1 mL mixture of DMF and DMSO (8/2, v/v) at 80 °C. The dripping solution was prepared by dissolving FAI (10 ~ 120 mg), MABr (10 mg), and MACl(0 ~ 10 mg) in 1 mL of isopropyl alcohol (IPA) containing triiodide (5 mmol). The triiodide solution was prepared by stirring I_2 in IPA at 80 °C for 7 days. The PbI_2/$PbBr_2$ precursor solution was spin-coated on the mp-TiO_2 substrate at 3,000 rpm for 30 s to obtain a transparent PbI_2($PbBr_2$)-DMSO

intermediate film. Then, 0.35 mL of the prepared dripping solution was dripped on top of the $PbI_2(PbBr_2)$-DMSO intermediate film and spin-coated at 5,000 rpm for 30 s. The film, which changed to dark brown in color during spin-coating, was dried on a hot plate at 150 °C for 0 ~ 40 min. The heat-treated film was washed with IPA, and then annealed at 100 °C for 30 min.

HTM & Electrode

A PTAA (EM Index, Mn = 17,500 g·mol^{-1})/toluene (10 mg/1 mL) solution with additives of 7.5 µL Li bis(trifluoromethanesulfonyl)imide (Li-TFSI)/acetonitrile (170 mg/1 mL) and 4 µL 4-*tert*-butylpyridine (TBP) was spin-coated on the perovskite layer/mp-TiO_2/bl-TiO_2/FTO substrate at 3,000 rpm for 30 s. Finally, an Au counter electrode was deposited by thermal evaporation; the active area of this electrode was fixed at 0.16 cm^2.

Characterization

The *J–V* curves were measured with a source meter (Keithley 2420) using a solar simulator (Newport, Oriel Class A, 91195A) at 100 mA·cm^{-2} illumination (AM 1.5 G) and a calibrated Si reference cell certificated by NREL. The *J–V* curves were measured in reverse (forward bias (1.2 V) → short circuit (0 V)) or forward (short circuit (0 V) → forward bias (1.2 V)) scan modes. The step voltage and delay time were fixed at 10 mV and 40 ms, respectively. The delay time is a delay set at each voltage step before measuring the current. The *J–V* curves of each device were measured by masking the active area with a metal mask (area of 0.096 cm^2). The X-ray diffraction (XRD) spectra of the prepared films were measured using a Rigaku SmartLab X-ray diffractometer. The morphology of the films was observed using a field-emission scanning electron microscope (MIRA3 LMU, Tescan).

Chapter 5. The Solution to Relax Halide Loss in Perovskite Films through Iodide Management

5.1 Introduction

Theoretical calculations indicate that point defects such as vacancy types (V_{MA}, V_{Pb}, V_I) and external invasion types (MA_i, Pb_i, I_i) are due to the low formation energy of $MAPbI_3$ perovskite[63, 64]. It has also been found that cationic substitution (MA_{Pb}, Pb_{MA}) and antisite substitutions (MA_I, Pb_I, I_{MA}, I_{Pb}) are also possible. It is known that most of the vacancy-type defects are generated at a thin electron level near the band edge[63, 65]. Deep-level defects such as interstitials and anti-sites that affect the non-radiative recombination of the perovskite layer are affected by I-pool or I-rich[63]. This phenomenon suggests that halide anions play a crucial role in controlling defects. Of course, the recombination center of the polycrystalline perovskite layer can also occur at crystal grain boundaries (GBs)[44, 66-69]. However, GBs do not affect charge recombination according to electron beam induced current (EBIC) studies[70]. It may be advantageous for charge separation as demonstrated using Kelvin Probe Force Microscopy (KPFM)[71]. In fact, some groups have reported improved performance by passivating under-coordinated Pb and I ions by in-situ or post-treatment of GBs with residual PbI_2[39, 44], 1,2-ethanedithiol (EDT)[66], pyridine[67], phenyl-C_{61}-butyric acid methyl ester (PCBM)[68], and guanidinium[69]. Nevertheless, the observed performance improvements were limited.

A new method of reducing the number of point defects in the composition is needed to further improve the performance of the PSCs, as no internal passivation method has been reported yet that utilizes the balance of halide ions in the treatment of the perovskite layer. Stewart et al. proposed that the two-step process can inhibit the formation of interstitial iodine[72]. In particular, the presence of I-rich tetraiodoplumbates (PbI_4^- species) may be related to the density of defects due to interstitial iodide (I_i) or may act as a charge recombination center. Nonetheless, the two-step process using DMSO as an intermediate can lead to the formation of an [organic cation-$(Pb_3I_8)_n]^{2n-}$, an I-deficient intermediate that is charge balanced by FA (or MA)[73].

Previously, I demonstrated the production of efficient PSCs based on formamidinium lead iodide ($FAPbI_3$) using a two-step process based on intramolecular exchange between organic cations and DMSO molecules to create a highly uniform and dense surface[16]. Based on these results, I report a method for making highly efficient perovskite films by using an optimal secondary reaction solution to reduce iodide deficiency. The PSCs fabricated by this method showed much better performance than the control cell. Ultimately, PSC prepared from secondary reaction solution containing iodine ion was able to obtain 22.1% PCE under 1un illumination (100mW / cm^2) condition.

5.2 Results & Discussion

Introducing Br⁻ into FAPbI₃ perovskite film to produce α-phase FAPbI₃ to work stably at room temperature was based on the intramolecular exchange method described in previous studies[16]. In the case of using PbI₂(DMSO) complex, DMSO ratio was changed when adding PbBr₂. Therefore, a mixed solution of dimethylformamide (DMF) and dimethylsulfoxide (DMSO) was used to overcome this problem. In order to match with the conventional method, mixed solution conditions of DMF and DMSO capable of forming a similar PbI₂ film were found by controlling the mixing ratio, the stirring temperature, and the stirring time change condition. Figure 5.2.1a shows the XRD patterns of the coated PbI₂ films for DMF and DMSO mixture ratios. In addition, it was confirmed that the FAPbI₃ membrane prepared using the PbI₂(DMSO) complex and the PbI₂ mixed solution of DMF and DMSO using the XRD pattern of Fig. 5.2.1b was successfully generated. The following procedure is also included in the process of dissolving PbI₂ and PbBr₂ (molar ratio = 95 / 5) in DMF and DMSO (80 / 20, v / v) ratio as a mixed solution.

Solid Iodine(I₂) was added to the second coating solution in the IEPs to solve the halide loss occurring during the heat treatment process. Solid Iodine (I₂) is dissolved in isopropyl alcohol solvent at 80 ° C with stirring. As seen in Eq. (1), iodine ion can be seen to be formed in the course of the oxidation of isopropyl alcohol to acetone[74].

$$(CH_3)_2CHOH\,(PA\,)\,+\,I_2\,\xrightarrow{\Delta}\,(CH_3)_2C\,=\,O(Acetone\,\,)+HI+I^- \qquad (1)$$
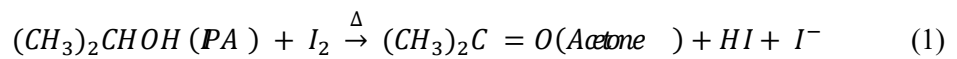
When the reaction is turned for a longer period, the triiodide (I₃⁻) is formed due to the reduction of free energy as shown in Eq. (2)[75].

$$I_2\,+\,I^-\,\rightleftarrows\,I_3^- \qquad (2)$$
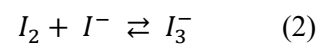
Spectroscopic analysis of the solvent in which iodine was dissolved in isopropyl alcohol showed an increase in light absorption at 291-361 nm (Figure 5.2.2). This result shows that the concentration of triiodide increases with the reaction time as shown in Eq. (1) and Eq. (2), which shows that all the iodine turns into triiodide after 7 days.

The perovskite solar cell was fabricated using the prepared iodine solution and has the following structure (Figure 5.2.3). : FTO / thin barrier TiO₂ (~60 nm) / mesoporous-TiO₂ : perovskite composite layer (~150 nm) / perovskite upper layer (~500 nm) / PTAA (~50 nm) / Au (~100 nm)

Figure 5.2.4 shows the result of measuring the power conversion efficiency by fabricating the device for the initial state and I₃⁻ state of the prepared iodine solution. As a result, it was observed that when the device was fabricated using I₃⁻ solution, J_{SC}, V_{OC}, and FF were all increased and high-efficiency

device was produced.

Based on these results, the characteristics of the perovskite device were confirmed by focusing on the I_3^- solution. Figure 5.2.5a shows the efficiency change of PSCs according to the amount of triiodide used in IEPs. The efficiency of the perovskite cell was significantly increased when triiodide was added regardless of the amount of the solution, which was highest when using a solution containing 3 mmol of triiodide. Solar cells using a large amount of triiodide (over 3 mmol) showed a slight decrease in performance, but all the photoelectric factors were found to decrease. This part is consistent with the claim that when perovskite layers are formed in the presence of a large number of iodines, the perovskite crystals become defective to form electron-hole recombination sites or carrier trap sites[72].

A current-voltage (I-V) graph of a perovskite cell and a non-perovskite solar cell using 3 mmol of triiodide as a solution is depicted in Figure 5.2.5b. The detailed photoelectric factor values (open circuit voltage (V_{OC}), short circuit current density (J_{SC}), fill factor (FF), and photoelectric conversion efficiency) are summarized in Table 5. The I_3^- added perovskite solar cell`s V_{OC} was 1.1 V, J_{SC} is 24.1 mA / cm^2, FF is 81.9%, and PCE is 21.6%. In contrast, the perovskite solar cell of the control cell is 20.3%, the V_{OC} is 1.07 V, the Jsc is 23.5 mA / cm^2, and FF is 80.8%. Compared with the control PSC, the increase of the efficiency of the I_3^- added PSC by 1.3% was able to have high efficiency as a result of simultaneously increasing J_{SC}, V_{OC}, and FF of the target PSC. It can be seen that the improved J_{SC} value is due to the improved light harvesting ability rather than the increase in charge collection since the thickness and surface morphology of the I_3^- added PSC and the control PSC are nearly identical (Figure 5.2.5). Increased V_{OC} and FF were shown to be due to improved crystallinity and reduced trap sites that lead to non-radiative charge recombination. Likewise, high crystallinity and good orientation have a significant effect on charge dissociation, transport, and diffusion length (For this reason, the open circuit voltage and fill factor values have been positively impacting the efficiency.)[76].

The J_{SC} value obtained from the J-V analysis is consistent with the spectral integral obtained from the external quantum efficiency (EQE) (Figure 5.2.5c). Figure 5.2.5d shows the UV-Vis absorption spectrum of the film. As expected, the absorption wavelengths of both films were very similar at ~ 800 nm. A possible absorption range over a broad spectrum range indicates that the presence of triiodide is not affected.

According to recent reports, since PbI_2 itself is often an I-deficiency, the intermediate may be composed of an I-deficient (organic cation) -Pb_3I_8 phase or an I-deficient $PbI_2(DMSO)$ complex[48, 73]. I, therefore, expect that the addition of I_3^- will increase the proportion of α-$FAPbI_3$ phase and decrease the concentration of defects in the whole perovskite layer. To obtain a deeper understanding of the nature of these defects, I performed deep level transient spectroscopy (DLTS) and steady-state and time-resolved PL. DLTS is a useful tool for studying electronic properties of defects such as density and activation energy and for capturing cross sections of deep defects[77]. I performed DLTS measurements in the 150-330 K range to compare the information on trap levels in the forbidden zone of the control

and target layers. As shown in Figure 5.2.6a, the temperature scan for the control layer shows three defect levels labeled A1, A2, and A3. In the I_3^- addition layer, the A1 signal disappeared and the defect concentration calculated at A2 decreased significantly from 5.28×10^{14} cm^{-3} to 8.81×10^{13} cm^{-3}. As the A1 peak disappears, it is speculated that defects at the A2 level can be easily healed by the presence of additional I_3^- in the formation of the perovskite phase. Dominant deep-level defects (A1 and A2) and semi-shallow defects (A3) with energy levels of 0.78 - 0.82 eV and 0.46 eV below the conduction band, respectively, have not yet been experimentally confirmed, but interstitial Pb (Pb_i) and antisite defects (MA_I, Pb_I, I_{MA}, and I_{Pb})[64, 65]. DLTS measurements confirmed that the addition of an iodide anion significantly reduced the level of defects of A1 and A2 corresponding to this energy level. The decrease in defect level density represents a decrease in the number of carrier recombination centers responsible for photoelectric conversion efficiency. However, in the case of A3, the change in the defect level could not be confirmed by adding triiodide. In the case of A3, the effect is believed to be due to the presence of point defects less than A1 and A2 or ionic bond breakdown.

The PL quenching yields of the control and I_3^- added layers are shown in Figure 5.2.7. α- An emission peak at 825 nm corresponding to $FAPbI_3$ was observed. The PL intensity of the target layer was significantly increased compared to the PL intensity of the control layer. The enhancement of the PL intensity is correlated with the difference (V) of the V_{OC} measured from the J-V characteristic as described in equation (3) under the condition that the voltage difference between the two devices is due to non-radiative recombination[78].

$$\Delta V = V_{OC}^{target} - V_{OC}^{control} = \frac{kT}{q} \cdot ln\left(\varphi_{PL}^{target} \big/ \varphi_{PL}^{control}\right) = ----- (3)$$

Where k is the Boltzmann constant, T is the temperature, q is the element charge, and $\varnothing_{PL}^{target}$ and $\varnothing_{PL}^{conrol}$ are the PL intensities of the two systems. The voltage difference (ΔV) between the target device and the control device is calculated as 0.020V, which is smaller than the measured difference (0.03V) between the two devices. However, the calculated voltage reduction is similar to the value (0.016 V) derived using the trap concentration determined using DLTS. This result suggests that the performance improvement achieved by introducing the triiodide into our system is related to a reduction in the deep level trap in the bulk perovskite layer. This phenomenon leads to a beneficial effect of reducing interfacial recombination by having a relatively rich iodine atom between the perovskite layer and the TiO_2 electrode interacting strongly with the titanium atom[79].

The carrier dynamics derived from transient PL behavior provide information on charge recombination through non-radiative recombination associated with defect concentration. The PL decay of each sample measured by time-correlated single photon counting (TCSPC) using a 620 nm solid-

state laser was fitted to the bi-exponential equation (Figure 5.2.6b). $Y = A1\exp(-t/\tau_1) + A2\exp(-t/\tau_2)$ and the results are summarized in Table 6[80]. The short PL lifetime quenching can be attributed to defect induced non-radiative recombination, while the long PL lifetime can be due to radiation recombination[81, 82]. The target layer exhibits a PL lifetime of about 138 ns and a long carrier lifetime of about 1,105 ns, while the control layer exhibits a PL lifetime of ~ 72 ns and ~ 228 ns. The lifetime of the long PL transition in the target layer may be due to a decrease in defect concentration and an increase in crystallinity. Therefore, it is suggested that the addition of triiodide ions to the loading solution can reduce the concentration of deep defects that cause charge recombination in the perovskite layer produced.

Based on these results, I adjusted the secondary solution and then repeated the production process to further improve PSC performance. Figure 5.2.8a shows the determined J-V curve for one of the most efficient cells measured with a 50 ms scanning delay in the reverse and forward scan modes under standard air mass 1.5 global (AM 1.5G) illumination. The J-V curve does not show any significant hysteresis between the two modes. The J_{SC}, V_{OC}, and FF values obtained from the J-V curve in the reverse scan mode were 25.0 mA / cm^2, 1.11 V, and 0.817, respectively, and a PCE of 22.6% under standard AM 1.5 G conditions. The corresponding values obtained from the J-V curve in forward scan mode were 25.0 mA / cm^2, 1.10 V, and 0.805, respectively, and a similar overall efficiency was 22.2%. For certification, these representative devices were sent to independent laboratories to show the efficiency of 22.1% reported to the PSC (Figure 5.2.9a). To test the performance reproducibility of a PSC fabricated using a tuned secondary solution, I prepared 80 cells independently under the same experimental conditions. The histogram of the mean PCE shown in Figure 5.2.8b shows that about 90% of the cells made using our method have an overall efficiency of more than 20.0% under 1 sun illumination with an average efficiency of $21.25 \pm 1.08\%$, and the benefit of added iodide ions the effect was confirmed. I also fabricated a large cell with an active area of about 1 cm^2 and confirmed the uniformity of the perovskite layer produced using the method described above. Figure 5.2.8c shows that the J_{SC}, V_{OC}, and FF values are 24.2 mA / cm^2, 1.14 mV, and 72.7%, respectively, and the overall PCE achieved 20.0% under the standard AM 1.5G condition. This performance was verified using the standardized method in the solar calibration laboratory and it was confirmed that the PCE was 19.7% under the condition of AM 1.5G (Figure 5.2.9b). A slight decrease in the performance of a large cell compared to the performance of a small cell may be due to the large sheet resistance of the FTO substrate.
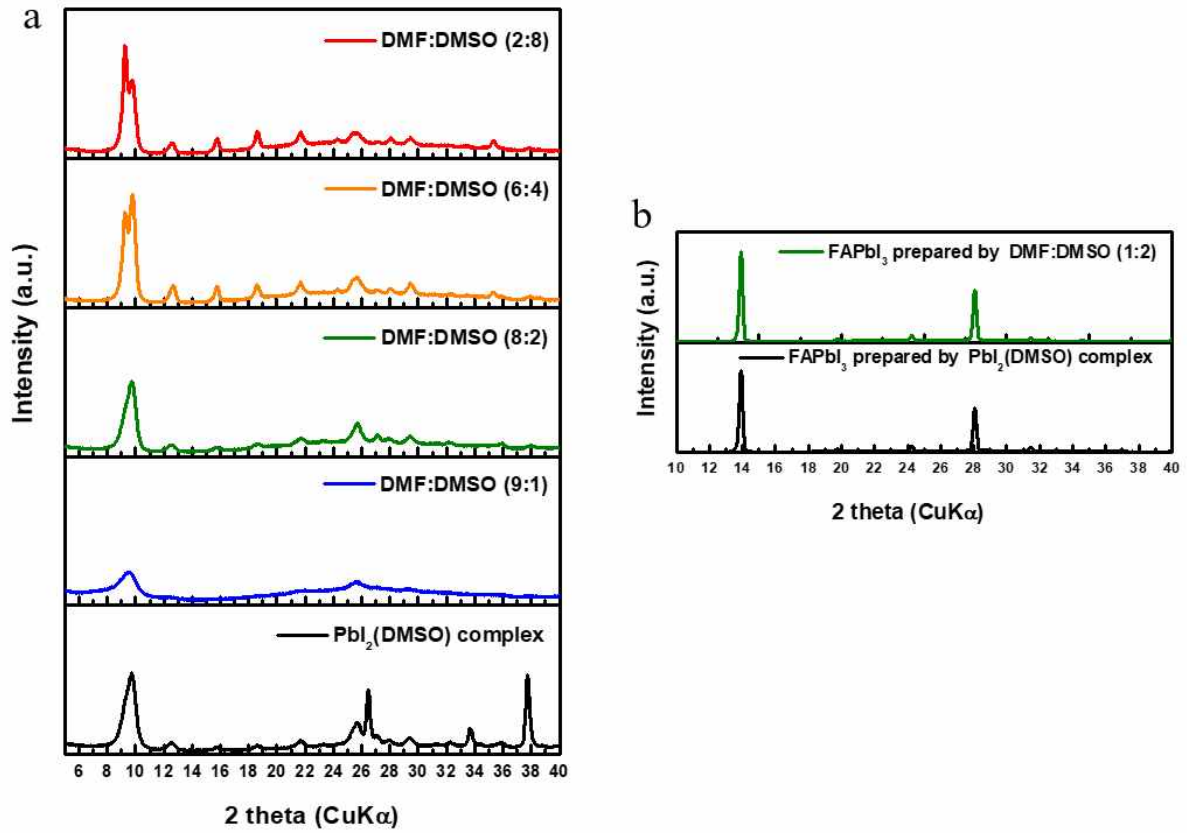
Figure 5.2.1 X-ray diffraction patterns of (a) PbI$_2$ film according to mixing ratio of DMF and DMSO (b) FAPbI$_3$ films prepared by DMF : DMSO (8:2) and PbI$_2$(DMSO) complex.
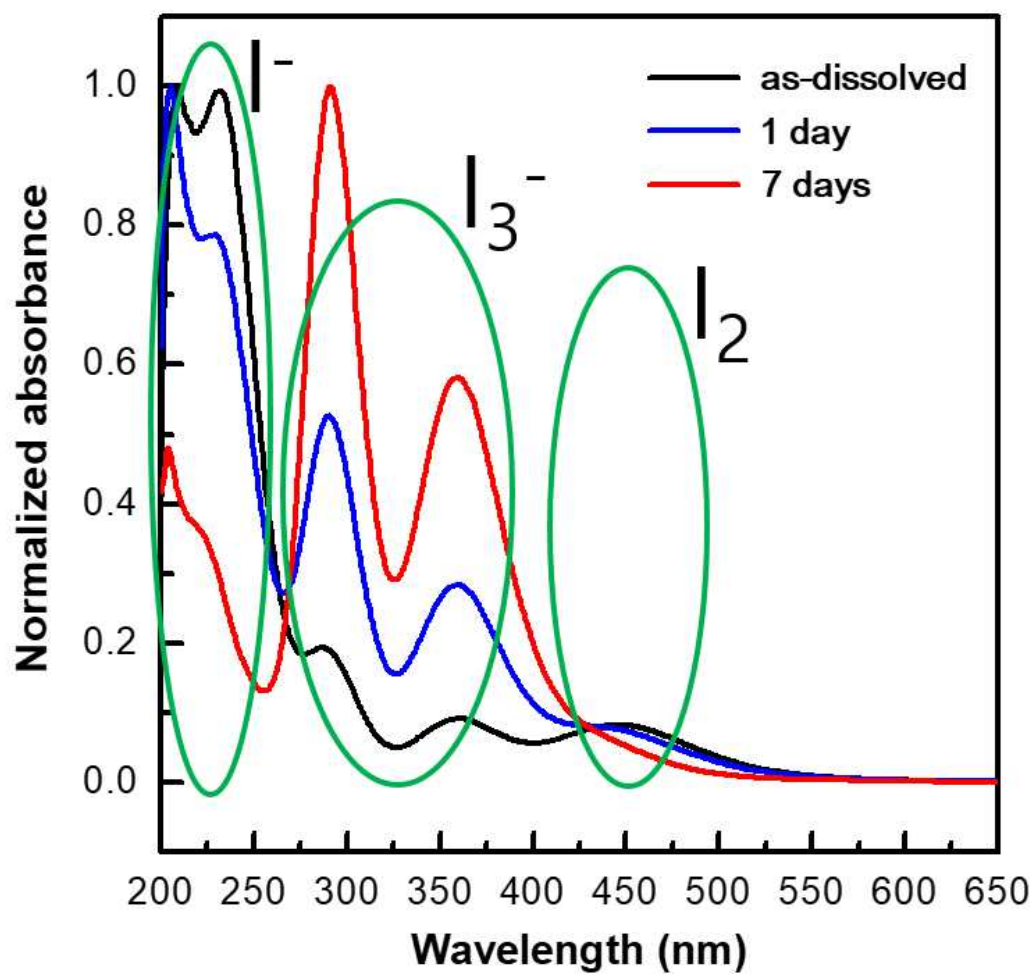
Figure 5.2.2 Changes in UV-absorption spectra after 1, and 7 days of iodine dissolving in isopropyl alcohol with stirring.
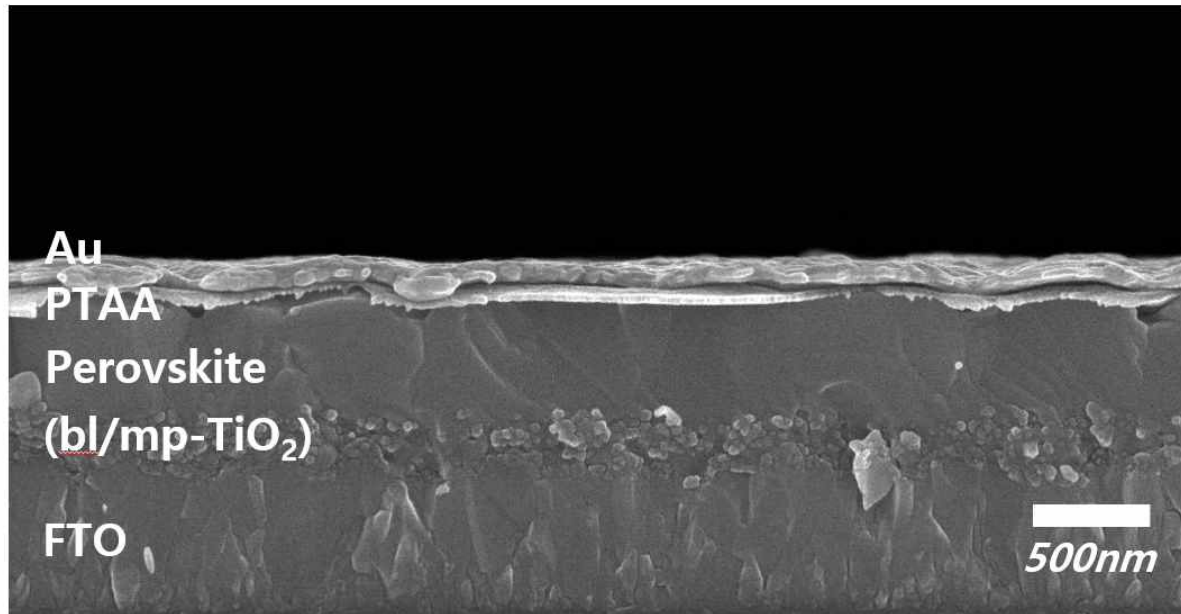
Figure 5.2.3 Cross-sectional FESEM image of the entire device (FTO / bl-TiO$_2$ / mp-TiO$_2$ / perovskite / PTAA / Au).
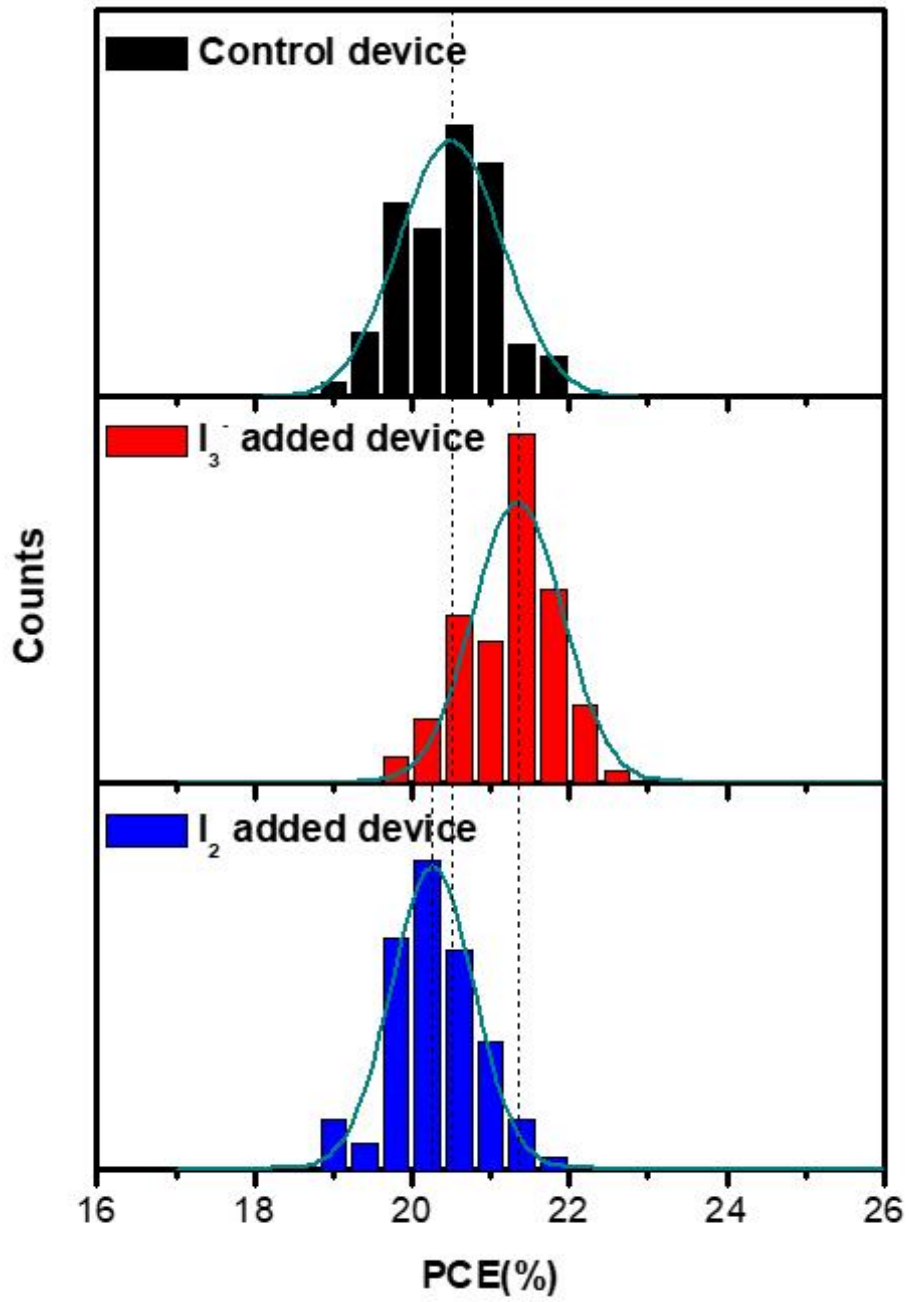
Figure 5.2.4 Efficiency distribution control device, I_3^- treated device & I_2 treated device.
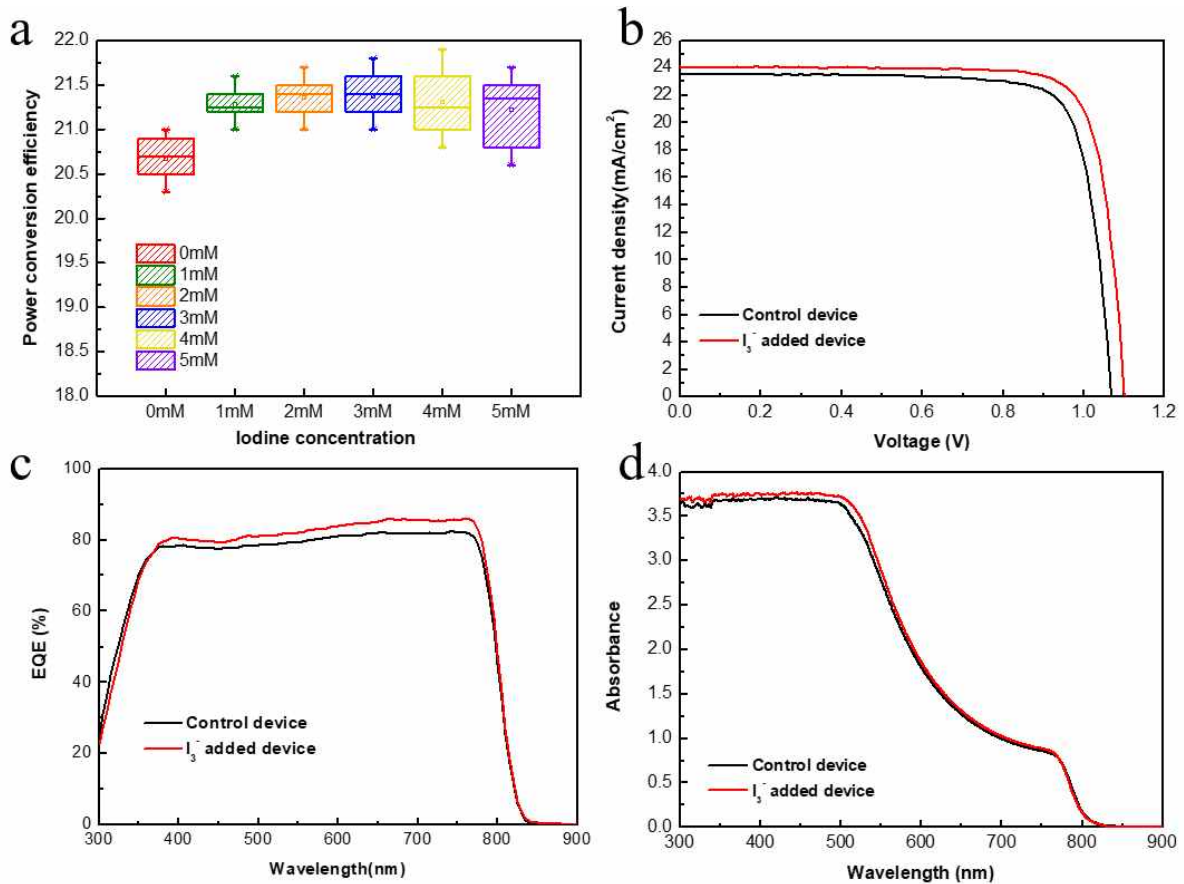
Figure 5.2.5 Device performance analysis and UV-Vis absorption spectra of perovskite layers deposited through IEPs with or without addition of triiodide ions to the loading solution. (a) The relationship between the dominant power conversion efficiency and the concentration of iodide ions added to the loading solution. (b) The J-V characteristic is measured under AM 1.5G illumination for the control and target device. (c) The external quantum efficiency and integration of the control and target devices. (d) UV-Vis absorption spectrum.

	Jsc (mA/cm²)	Voc (V)	FF	PCE (%)	Rseries(ohm)
Control	23.5	1.07	80.8	20.3	26.39
I₃⁻ added	24.1	1.1	81.9	21.6	25.51

Table 5 Photocell performance of devices.
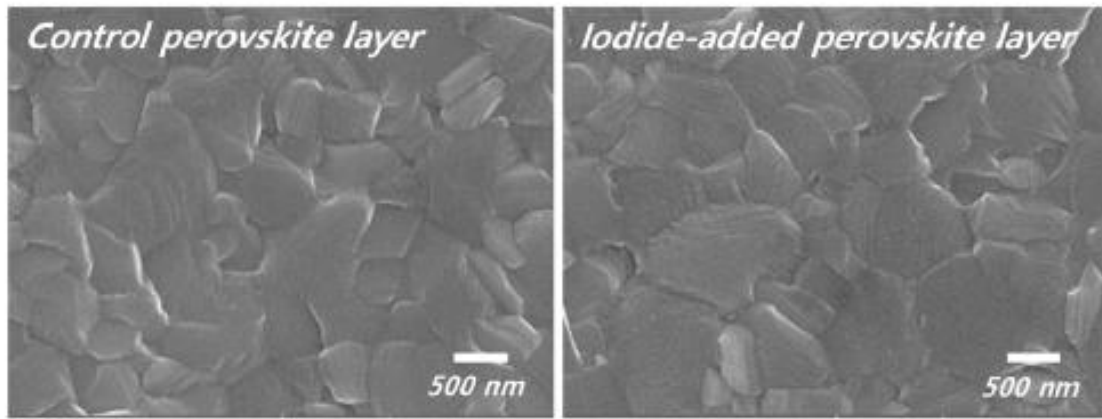
Figure 5.2.5 FESEM image of control and I_3^- added perovskite film.
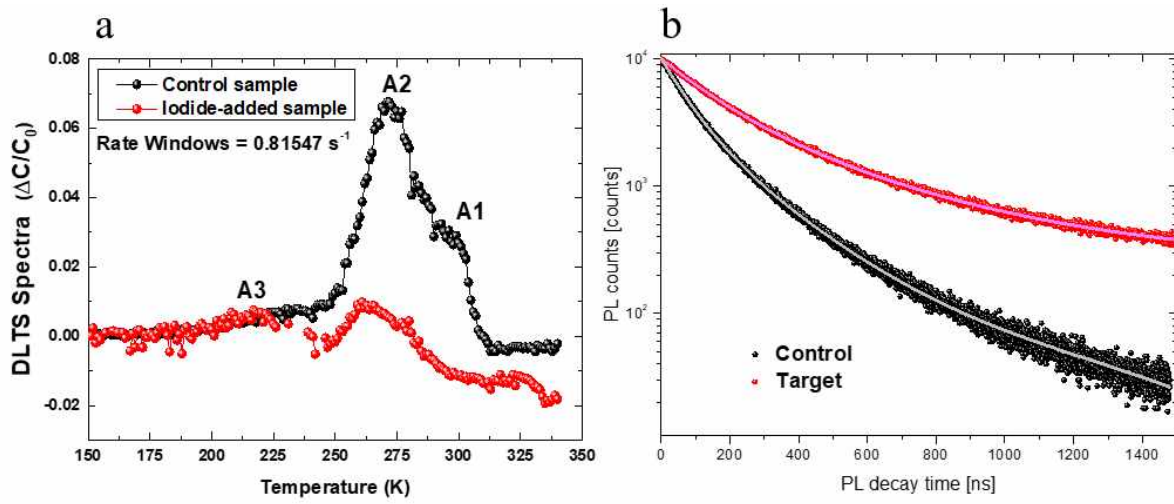
Figure 5.2.6 Deep-level transient spectroscopy (DLTS), and time-resolved photoluminescence (TRPL) analysis (a) The DLTS spectrum of the control and target layers was measured between 150K and 330K, (b) TRPL is the decay curve of the control and target perovskite layers emitted at λ = 825 nm with a bi-exponential fit.
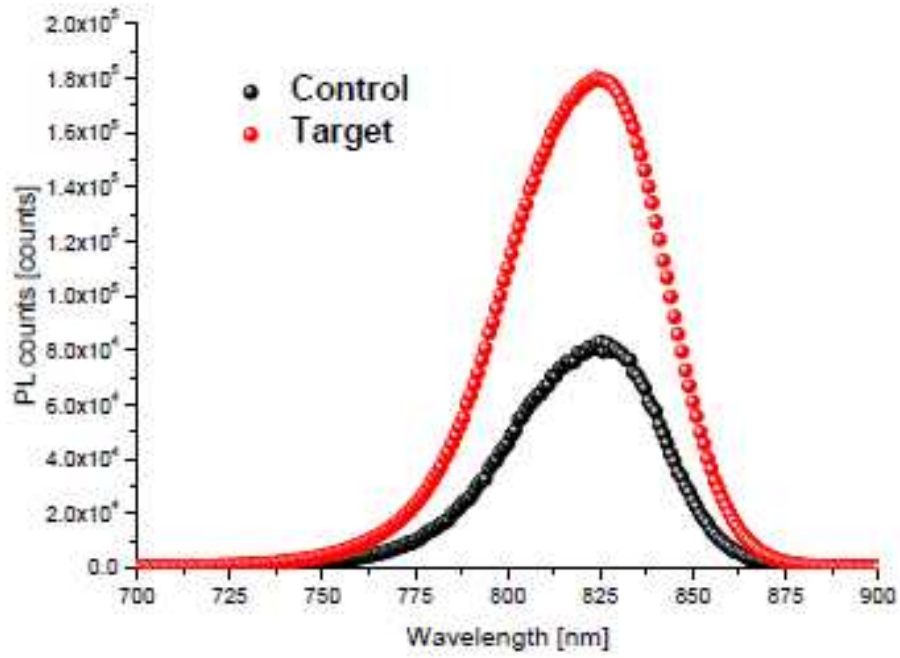
Figure 5.2.7 Photoluminescence emission spectrum of control layer and target layer.

	τ_1	τ_2
Control film	72 ns	228ns
I_3^- **added film**	138ns	1105 ns

Table 6 The fitting parameters obtained by fitting the TCSPC results to the bi-exponential decay equation: $Y = A1\exp(-t / \tau_1) + A2\exp(-t / \tau_2)$.
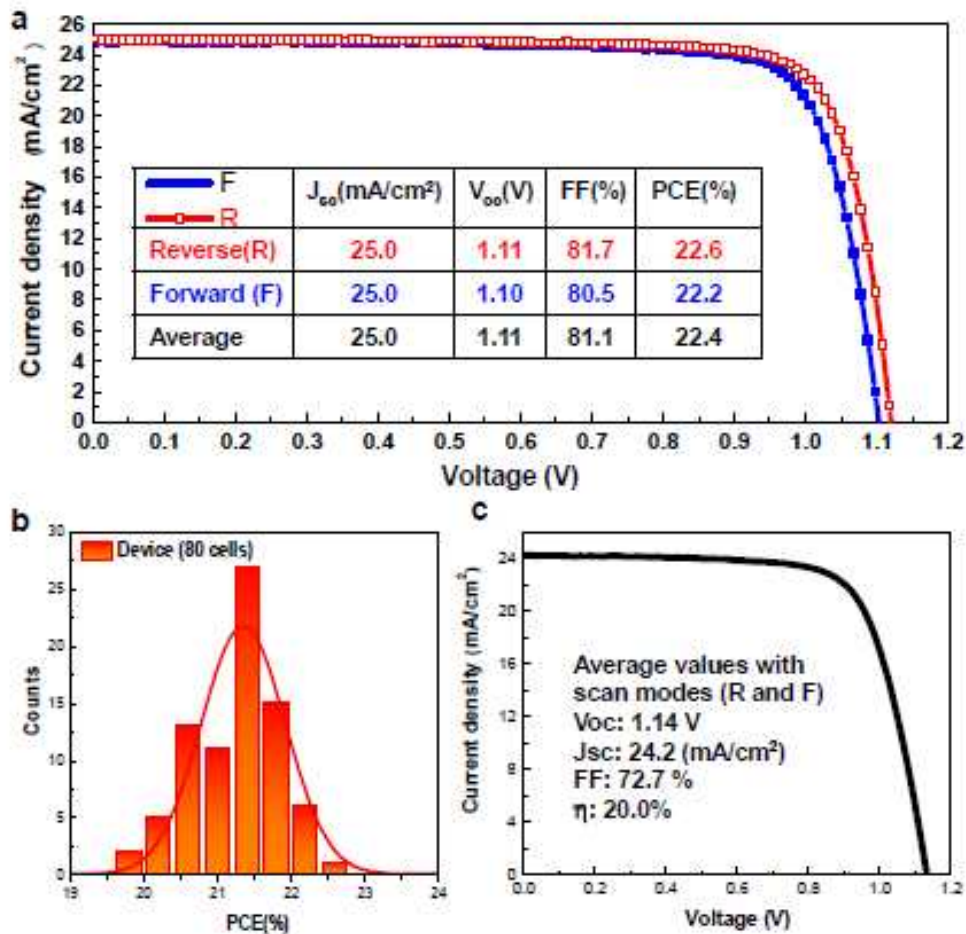
Figure 5.2.8 Current density-voltage (J-V) curves and photovoltaic parameters and device reproducibility of small and large PSCs with best performance (a) The JV curve at a PSC of 0.095 cm^2 shows small parameters in the forward and reverse scan modes (b) A histogram of average power conversion efficiency determined for a PSC of 80 ea (c) Average value of the J-V curve for the forward and reverse scanning modes for a PSC area of 1 cm^2.
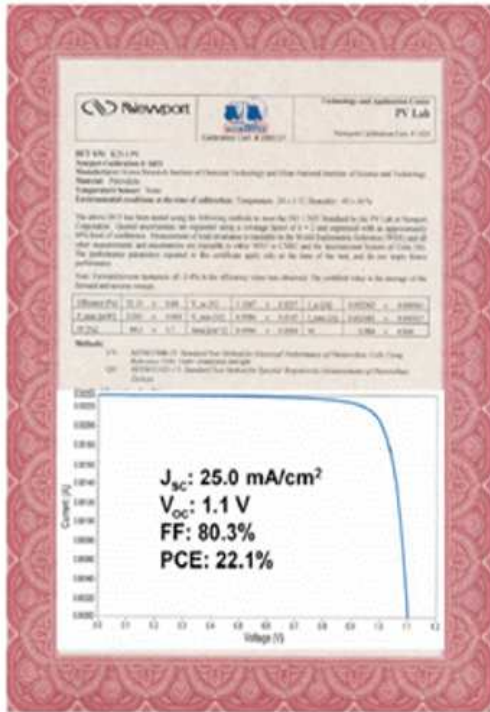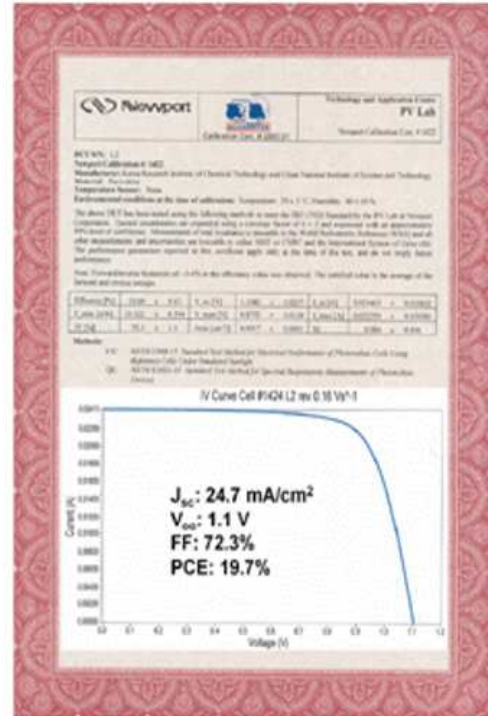
Figure 5.2.9 Newport Corp. Independent certification (a) area (0.0946 cm^2) (b) area (~ 1 cm^2).

5.3 Conclusion

Halogenated inorganic / organic hybrid perovskite materials using formamidinium (FA) with multiple cations and mixed halide anions have been shown to exhibit excellent performance and high stability[38, 83-85]. It is crucial to manufacturing a high-performance perovskite solar cell (PSC) by forming a dense and uniform thin film on the substrate, rather than controlling the composition of the material itself[16, 50, 86]. In order to further improve the power conversion efficiency (PCE) of the PSC, the concentration of the defect state, which is known to reduce the performance of the battery by decreasing the open circuit voltage (V_{OC}) and the short circuit current density (J_{SC}), should be as low as possible. In this study, I first report the certified PCE of 22.1% in small cells and 19.7% in 1 cm^2 cells using the composition of defect-controlled perovskite films.

I analyzed the perovskite films produced by the IEPs method using deep-level transient spectroscopy (DLTS) and time-correlated single photon counting (TCSPC) measurements. The addition of iodide ion to the organic cation solution used to form the perovskite thin film shows that it has a significant effect on the microstructure development, the concentration of the deep defect and hence the charge carrier recombination.

I believe that the management of halide anions in the perovskite layer will provide a new direction for the production of high-efficiency PSCs.

5.4 Experimental

Materials

Unless stated otherwise, all materials were purchased from Sigma-Aldrich or Junsei Organics and used as received. Poy(triarylamine) (PTAA) was purchased from EM Index.

Synthesis of Inorganic / Organic Halide Materials

NH$_2$CH=NH$_2$I (FAI) was synthesized by reacting 30 mL hydroiodic acid (57% in water, Aldrich) and 15 g formamidine acetate (Aldrich) in a 250 mL round-bottomed flask at 0 °C for 2 h with stirring. Similarly, CH$_3$NH$_3$Br (MABr) was synthesized by reacting 27.86 mL CH$_3$NH$_2$ (40% in methanol, Junsei Chemical) and 44 mL hydrobromic acid (48 wt% in water, Aldrich) in a 250 mL round-bottom flask at 0 °C for 4 h with stirring. The precipitates were recovered by evaporating the solutions at 50 °C for 1 h. The products were dissolved in ethanol, recrystallized from diethyl ether, and finally dried at 60 °C in a vacuum oven for 24 h.

Solar Cell Fabrication

TiO$_2$ Substrate

A dense blocking layer of TiO$_2$ (60 nm, bl-TiO$_2$) was deposited onto a F-doped SnO$_2$ (FTO, Pilkington, TEC8) substrate by spray pyrolysis using a 20 mM titanium diisopropoxide bis(acetylacetonate) solution (Aldrich) at 450 °C; this was done to prevent a direct contact between FTO and the hole-conducting layer. A 150-nm thick mesoporous (mp) TiO$_2$ was spin-coated onto the bl-TiO$_2$/FTO substrate using diluted TiO$_2$ paste and calcinated at 500 °C for 1 h in air to remove the organic components.

Perovskite Film [Mixed Solvent]

PbI$_2$ (1.30 M) containing 2.5 mol% PbBr$_2$ was dissolved in a 1 mL mixture of DMF and DMSO (8/2, v/v) at 80 °C. The dripping solution was prepared by dissolving FAI (80 mg) and MABr (10 mg) in 1 mL of isopropyl alcohol (IPA) containing triiodide (0–5 mmol). The triiodide solution was prepared by stirring I$_2$ in IPA at 80 °C for 7 days.

The PbI$_2$/PbBr$_2$ precursor solution was spin-coated on the mp-TiO$_2$ substrate at 3,000 rpm for 30 s to obtain a transparent PbI$_2$(PbBr$_2$)-DMSO intermediate film. Then, 0.35 mL of the prepared dripping solution was dripped on top of the PbI$_2$(PbBr$_2$)-DMSO intermediate film and spin-coated at 5,000 rpm for 30 s. The film, which changed to dark brown in color during spin-coating, was dried on a hot plate at 100 °C for 30 min and then at 150 °C for 30 min. The heat-treated film was washed with IPA, and

then annealed at 100 °C for 30 min.

HTM & Electrode

A PTAA (EM Index, Mn = 17,500 g·mol^{-1})/toluene (10 mg/1 mL) solution with additives of 7.5 µL Li bis(trifluoromethanesulfonyl)imide (Li-TFSI)/acetonitrile (170 mg/1 mL) and 4 µL 4-*tert*-butylpyridine (TBP) was spin-coated on the perovskite layer/mp-TiO$_2$/bl-TiO$_2$/FTO substrate at 3,000 rpm for 30 s. Finally, an Au counter electrode was deposited by thermal evaporation; the active area of this electrode was fixed at 0.16 cm^2.

Characterization

The J–V curves were measured with a source meter (Keithley 2420) using a solar simulator (Newport, Oriel Class A, 91195A) at 100 mA·cm^{-2} illumination (AM 1.5 G) and a calibrated Si reference cell certificated by NREL. The J–V curves were measured in reverse (forward bias (1.2 V) → short circuit (0 V)) or forward (short circuit (0 V) → forward bias (1.2 V)) scan modes. The step voltage and delay time were fixed at 10 mV and 40 ms, respectively. The delay time is a delay set at each voltage step before measuring the current. The J–V curves of each device were measured by masking the active area with a metal mask (area of 0.096 cm^2). External quantum efficiency (EQE) values were measured using a power source (Newport 300 W Xenon lamp, 66920) with a monochromator (Newport Cornerstone 260) and a multimeter (Keithley 2001). Grazing-incidence wide-angle X-ray scattering **(**GIWAXS) measurements were conducted at beamline 6D at the Pohang Accelerator Laboratory (PAL), Republic of Korea. X-rays (λ = 0.62382 Å) were incidence angles of 0.05° or 0.3° were used and samples were exposed to the X-rays for 5 s during scanning. The deep-level transient spectroscopy **(**DLTS) measurement system consisted of a HP4280A 1 MHz capacitive analyzer, a Boonton 7200 1 MHz capacitive analyzer, a HP8116A pulse generator, a SR640 filter, and a digital data acquisition device. The temperature was varied from 12 to 350 K using a liquid helium cooling method and controlled accurately within 0.01 K using a He cryostat. A Au Schottky junction was formed using a thermal evaporator to deposit a Au electrode with a diameter of 500 µm and a thickness of 200 nm. DLTS measurements were carried out at 150–330 K for the perovskite structure of the fabricated Schottky junction. The filling pulse bias was 0 V, the measurement bias was −0.7 V, and the rate windows were 0.81547 s^{-1}. Capacitance-voltage (C–V) measurements showed that the carrier concentrations of the control and target perovskite structures were 1.52×10^{15} cm^{-3} and 1.74×10^{15} cm^{-3}, respectively. Steady-state photoluminescence (PL) spectra were recorded using a commercial time-correlated single photon counting (TCSPC) setup (FluoTime 300, PicoQuant GmbH) equipped with PMA-C-192-M detector, high-resolution excitation monochromators. Front-face illumination (30° with respect to the incident beam) was used to minimize inner-filter effects. Charge excitation of samples was conducted at 620 nm solid-state laser (intensity power maximum of 1.5 mW·cm^{-2}, as measured using a power meter

(Thorlabs PM100D)). The diode laser was controlled by a PDL 820 driver to control the picosecond pulses of the excitation light source (internal repetition rates between 196 kHz and 80 MHz). Hybrid perovskite was coated on quartz glass substrates. The PL was collected using a high-resolution monochromator and a hybrid photomultiplier detector assembly (PMA Hybrid 40, PicoQuant GmbH). The laser beam was incident on the back side of the hybrid perovskite film. The PL decay signal was detected at 825 nm and collected using integrated sphere mounted on the instrument.

Chapter 6. Summary

In order to produce an efficient perovskite solar cell, many requirements are required. However, if the quality of the perovskite film is not satisfied in advance, the other requirements lose their meaning. In addition, the formation of a dense and uniform thin film on a substrate alone is crucial to the production of a high-performance perovskite solar cell. Perovskite materials are very difficult to form uniform and dense films because of their rapid reaction and self-assembling properties resulting in various thin film morphologies. Therefore, there is a need to improve the surface flatness by controlling the rapid crystallization behavior and to complete the surface bonding.

A perovskite layer coating method called Intramolecular exchange process (IEPs) was developed to form high-quality perovskite film. This is an improvement on the sequential deposition coating method. In the conventional sequential deposition coating method, the PbI_2 layer and the FAI layer are sequentially coated. Subsequently, the film is converted to a perovskite film by a diffusing reaction through a heat treatment process. This process involves crystal nucleation and perovskite phase growth due to the solution or solid state reaction between PbI_2 and organic iodides such as FAI. However, the sequential reaction of PbI_2 and organic iodide to the inner crystal region from the surface of PbI_2 was not effective in producing high-performance perovskite films. The reason is the incomplete conversion of PbI_2, peeling off of the perovskite film in solution, and uncontrolled surface roughness. In the case of IEPs, the crystal formation reaction is induced through the substitution of DMSO and FAI during the spin coating process using a film of newly prepared PbI_2(DMSO) complex. This reaction mechanism does not generate residual PbI_2. Also, due to the similar molecular size of DMSO and FAI, it does not induce volume expansion. As a result, a high-quality $FAPbI_3$ film can be produced. I deposited a $FAPbI_3$-based layer with a thickness of about 500 nm and deposited a fluorine-doped tin oxide (FTO) - glass / barrier layer (bl) -TiO_2 / mesoporous (mp) -TiO_2 / perovskite / poly-triarylamine Au. The current density-voltage (J-V) curve of the fabricated cell with a $FAPbI_3$-based layer was measured under a standard air mass 1.5 global (AM 1.5G) illumination to obtain a device efficiency of 20.2% (J_{SC} = 24.7 mA / cm^2, V_{OC} = 1.06 V, FF = 77.5%).

For the improved Perovskite film, the grain size was controlled by controlling the crystallization rate. In order to improve the optical-cell-physical properties such as light collection, electron transport, and electron diffusion, it is important to control a thin film shape with a uniform and large crystal grains and having few defects. PbI_2, FAI, and MACl make a significant contribution to making uniform and large crystalline $FAPbI_3$ films in IEPs. The morphology changes of $FAPbI_3$ films according to each material were observed through FESEM and the light conversion efficiency of the device was confirmed to confirm the conditions for producing high-efficiency perovskite solar cell.

I_3^- was introduced into the IEPs to solve the imbalance of halide ion during the heat treatment of the perovskite layer. Perovskite solar cells were fabricated by adding I_3^- to the second coating solution. The cell density-voltage (J-V) curves of the fabricated cell were measured under a standard air mass 1.5 global (AM 1.5G) illumination to obtain a device efficiency of 22.1% ($J_{SC} = 24.7$ mA / cm^2, $V_{OC} = 1.06$ V, FF= 77.5 %). Deep-level transient spectroscopy (DLTS) measurements confirmed that deep-level defects with energy levels of 0.78 - 0.82 eV and 0.46 eV were healed after the addition of I_3^-. And, long carrier lifetime was confirmed through time-correlated single photon counting (TCSPC) measurements. The addition of iodide ions to the organic cation solution shows a significant influence on the development of microstructure, the concentration of deep defects, and thus the charge carrier recombination.

High-efficiency solar cells can be produced with high reproducibility using IEP. This research provides an effective protocol for fabricating efficient and cost-effective inorganic-organic hybrid junction solar cells.

REFERENCES

1. Petroleum, B., BP Statistical Review of World Energy, London. 2016.

2. Adib, R.; Murdock, H.; Appavou, F.; Brown, A.; Epp, B.; Leidreiter, A.; Lins, C.; Murdock, H.; Musolino, E.; Petrichenko, K., Renewables 2015 global status report. *Paris: REN21 Secretariat* **2015**.

3. Tsao, J.; Lewis, N.; Crabtree, G., Solar faqs. *US department of Energy* **2006**, 1-24.

4. NREL Best Research-Cell Efficiency Chart. https://www.nrel.gov/pv/cell-efficiency.html.

5. Green, M. A., The path to 25% silicon solar cell efficiency: history of silicon cell evolution. *Progress in Photovoltaics: Research and Applications* **2009,** *17* (3), 183-189.

6. Chapin, D. M.; Fuller, C.; Pearson, G., A new silicon p-n junction photocell for converting solar radiation into electrical power. *Journal of Applied Physics* **1954,** *25* (5), 676-677.

7. Kojima, A.; Teshima, K.; Shirai, Y.; Miyasaka, T., Organometal halide perovskites as visible-light sensitizers for photovoltaic cells. *Journal of the American Chemical Society* **2009,** *131* (17), 6050-6051.

8. Cui, D.; Yang, Z.; Yang, D.; Ren, X.; Liu, Y.; Wei, Q.; Fan, H.; Zeng, J.; Liu, S., Color-tuned perovskite films prepared for efficient solar cell applications. *The Journal of Physical Chemistry C* **2015,** *120* (1), 42-47.

9. Whitfield, P.; Herron, N.; Guise, W.; Page, K.; Cheng, Y.; Milas, I.; Crawford, M., Structures, phase transitions and tricritical behavior of the hybrid perovskite methyl ammonium lead iodide. *Scientific reports* **2016,** *6*, 35685.

10. Kim, H.-S.; Lee, C.-R.; Im, J.-H.; Lee, K.-B.; Moehl, T.; Marchioro, A.; Moon, S.-J.; Humphry-Baker, R.; Yum, J.-H.; Moser, J. E., Lead iodide perovskite sensitized all-solid-state submicron thin film mesoscopic solar cell with efficiency exceeding 9%. *Scientific reports* **2012,** *2*, 591.

11. Noh, J. H.; Im, S. H.; Heo, J. H.; Mandal, T. N.; Seok, S. I., Chemical management for colorful, efficient, and stable inorganic–organic hybrid nanostructured solar cells. *Nano letters* **2013,** *13* (4), 1764-1769.

12. Kitazawa, N.; Watanabe, Y.; Nakamura, Y., Optical properties of CH 3 NH 3 PbX 3 (X= halogen) and their mixed-halide crystals. *Journal of materials science* **2002,** *37* (17), 3585-3587.

13. Li, M.-H.; Shen, P.-S.; Wang, K.-C.; Guo, T.-F.; Chen, P., Inorganic p-type contact materials for perovskite-based solar cells. *Journal of Materials Chemistry A* **2015,** *3* (17), 9011-9019.

14. UNIVERSITET, U. Perovskite crystal structure. https://www.kemi.uu.se/research/physical-chemistry/research-groups/gerrit-boschloo-group/perovskite-solar-cells/.

15. Korshunova, K.; Winterfeld, L.; Beenken, W. J.; Runge, E., Thermodynamic stability of mixed Pb: Sn methyl-ammonium halide perovskites. *physica status solidi (b)* **2016,** *253* (10), 1907-1915.

16.   Yang, W. S.;   Noh, J. H.;   Jeon, N. J.;   Kim, Y. C.;   Ryu, S.;   Seo, J.;   Seok, S. I., High-performance photovoltaic perovskite layers fabricated through intramolecular exchange. *Science* **2015,** *348* (6240), 1234-1237.

17.   Docampo, P.;   Ball, J. M.;   Darwich, M.;   Eperon, G. E.; Snaith, H. J., Efficient organometal trihalide perovskite planar-heterojunction solar cells on flexible polymer substrates. *Nature communications* **2013,** *4*, 2761.

18.   Lee, M. M.;   Teuscher, J.;   Miyasaka, T.;   Murakami, T. N.; Snaith, H. J., Efficient hybrid solar cells based on meso-superstructured organometal halide perovskites. *Science* **2012,** *338* (6107), 643-647.

19.   Jiang, C.-S.;   Yang, M.;   Zhou, Y.;   To, B.;   Nanayakkara, S. U.;   Luther, J. M.;   Zhou, W.; Berry, J. J.;   Van De Lagemaat, J.; Padture, N. P., Carrier separation and transport in perovskite solar cells studied by nanometre-scale profiling of electrical potential. *Nature communications* **2015,** *6*, 8397.

20.   Green, M. A.;   Zhao, J.;   Wang, A.; Wenham, S. R., Very high efficiency silicon solar cells-science and technology. *IEEE Transactions on electron devices* **1999,** *46* (10), 1940-1947.

21.   Sanchez, R. S.;   Gonzalez-Pedro, V.;   Lee, J.-W.;   Park, N.-G.;   Kang, Y. S.;   Mora-Sero, I.; Bisquert, J., Slow dynamic processes in lead halide perovskite solar cells. Characteristic times and hysteresis. *The journal of physical chemistry letters* **2014,** *5* (13), 2357-2363.

22.   Wang, H.;   Sheikh, A. D.;   Feng, Q.;   Li, F.;   Chen, Y.;   Yu, W.;   Alarousu, E.;   Ma, C.; Haque, M. A.; Shi, D., Facile synthesis and high performance of a new carbazole-based hole-transporting material for hybrid perovskite solar cells. *ACS Photonics* **2015,** *2* (7), 849-855.

23.   Wehrenfennig, C.;   Eperon, G. E.;   Johnston, M. B.;   Snaith, H. J.; Herz, L. M., High charge carrier mobilities and lifetimes in organolead trihalide perovskites. *Advanced materials* **2014,** *26* (10), 1584-1589.

24.   Wang, Z.;   Lou, Y.;   Naka, S.; Okada, H., Bias and temperature dependent charge transport in solution-processed small molecular mixed single layer organic light emitting devices. *Applied Physics Letters* **2011,** *98* (6), 24.

25.   Eperon, G. E.;   Burlakov, V. M.;   Docampo, P.;   Goriely, A.; Snaith, H. J., Morphological control for high performance, solution-processed planar heterojunction perovskite solar cells. *Advanced Functional Materials* **2014,** *24* (1), 151-157.

26.   Zhao, Z.;   Chen, X.;   Wu, H.;   Wu, X.; Cao, G., Probing the photovoltage and photocurrent in perovskite solar cells with nanoscale resolution. *Advanced Functional Materials* **2016,** *26* (18), 3048-3058.

27.   Shi, D.;   Adinolfi, V.;   Comin, R.;   Yuan, M.;   Alarousu, E.;   Buin, A.;   Chen, Y.;   Hoogland, S.;   Rothenberger, A.; Katsiev, K., Low trap-state density and long carrier diffusion in organolead trihalide perovskite single crystals. *Science* **2015,** *347* (6221), 519-522.

28.   D'Innocenzo, V.;   Srimath Kandada, A. R.;   De Bastiani, M.;   Gandini, M.; Petrozza, A., Tuning the light emission properties by band gap engineering in hybrid lead halide perovskite. *Journal of the American Chemical Society* **2014,** *136* (51), 17730-17733.

29.   Zhang, B.;   Zhang, M. J.;   Pang, S. P.;   Huang, C. S.;   Zhou, Z. M.;   Wang, D.;   Wang, N.; Cui, G. L., Carrier transport in CH3NH3PbI3 films with different thickness for perovskite solar cells. *Advanced Materials Interfaces* **2016,** *3* (17), 1600327.

30.   Wang, L.;   Liu, F.;   Liu, T.;   Wang, J.;   Cai, X.;   Wang, G.;   Ma, T.;   Jiang, C., Pinhole-free perovskite films by methylamine iodide solution-assisted repair for high-efficiency photovoltaics under ambient conditions. *ACS applied materials & interfaces* **2016,** *8* (45), 30920-30925.

31.   Wang, K.;   Liu, C.;   Du, P.;   Chen, L.;   Zhu, J.;   Karim, A.; Gong, X., Efficiencies of perovskite hybrid solar cells influenced by film thickness and morphology of CH3NH3PbI3− xClx layer. *Organic Electronics* **2015,** *21*, 19-26.

32.   Koh, T. M.;   Fu, K.;   Fang, Y.;   Chen, S.;   Sum, T.;   Mathews, N.;   Mhaisalkar, S. G.;   Boix, P. P.;   Baikie, T., Formamidinium-containing metal-halide: an alternative material for near-IR absorption perovskite solar cells. *The Journal of Physical Chemistry C* **2013,** *118* (30), 16458-16462.

33.   Pellet, N.;   Gao, P.;   Gregori, G.;   Yang, T. Y.;   Nazeeruddin, M. K.;   Maier, J.; Grätzel, M., Mixed-organic-cation Perovskite photovoltaics for enhanced solar-light harvesting. *Angewandte Chemie International Edition* **2014,** *53* (12), 3151-3157.

34.   Lee, J. W.;   Seol, D. J.;   Cho, A. N.;   Park, N. G., High-efficiency perovskite solar cells based on the black polymorph of HC (NH2) 2PbI3. *Advanced Materials* **2014,** *26* (29), 4991-4998.

35.   Knop, O.;   Wasylishen, R. E.;   White, M. A.;   Cameron, T. S.; Oort, M. J. V., Alkylammonium lead halides. Part 2. CH3NH3PbX3 (X= Cl, Br, I) perovskites: cuboctahedral halide cages with isotropic cation reorientation. *Canadian Journal of Chemistry* **1990,** *68* (3), 412-422.

36.   Heo, J. H.;   Song, D. H.; Im, S. H., Planar CH3NH3PbBr3 hybrid solar cells with 10.4% power conversion efficiency, fabricated by controlled crystallization in the spin-coating process. *Advanced Materials* **2014,** *26* (48), 8179-8183.

37.   Baena, J. P. C.;   Steier, L.;   Tress, W.;   Saliba, M.;   Neutzner, S.;   Matsui, T.;   Giordano, F.; Jacobsson, T. J.;   Kandada, A. R. S.; Zakeeruddin, S. M., Highly efficient planar perovskite solar cells through band alignment engineering. *Energy & Environmental Science* **2015,** *8* (10), 2928-2934.

38.   Jeon, N. J.;   Noh, J. H.;   Yang, W. S.;   Kim, Y. C.;   Ryu, S.;   Seo, J; Seok, S. I., Compositional engineering of perovskite materials for high-performance solar cells. *Nature* **2015,** *517* (7535), 476.

39.   Bi, D.;   Tress, W.;   Dar, M. I.;   Gao, P.;   Luo, J.;   Renevier, C.;   Schenk, K.;   Abate, A.; Giordano, F.; Baena, J.-P. C., Efficient luminescent solar cells based on tailored mixed-cation perovskites. *Science advances* **2016,** *2* (1), e1501170.

40.   Jacobsson, T. J.;   Correa-Baena, J.-P.;   Pazoki, M.;   Saliba, M.;   Schenk, K.;   Grätzel, M.; Hagfeldt, A. J. E.; Science, E., Exploration of the compositional space for mixed lead halogen perovskites for high efficiency solar cells. **2016,** *9* (5), 1706-1724.

41.   Roldan-Carmona, C.;   Gratia, P.;   Zimmermann, I.;   Grancini, G.;   Gao, P.;   Graetzel, M.; Nazeeruddin, M. K. J. E.; Science, E., High efficiency methylammonium lead triiodide perovskite solar cells: the relevance of non-stoichiometric precursors. **2015,** *8* (12), 3550-3556.

42.   Kim, Y. C.;   Jeon, N. J.;   Noh, J. H.;   Yang, W. S.;   Seo, J.;   Yun, J. S.;   Ho-Baillie, A.; Huang, S.;   Green, M. A.; Seidel, J. J. A. E. M., Beneficial effects of PbI2 incorporated in organo-lead

halide perovskite solar cells. **2016,** *6* (4), 1502104.

43.	Cao, D. H.; Stoumpos, C. C.; Malliakas, C. D.; Katz, M. J.; Farha, O. K.; Hupp, J. T.; Kanatzidis, M. G. J. A. M., Remnant PbI2, an unforeseen necessity in high-efficiency hybrid perovskite-based solar cells? **2014,** *2* (9), 091101.

44.	Chen, Q.; Zhou, H.; Song, T.-B.; Luo, S.; Hong, Z.; Duan, H.-S.; Dou, L.; Liu, Y.; Yang, Y. J. N. l., Controllable self-induced passivation of hybrid lead iodide perovskites toward high performance solar cells. **2014,** *14* (7), 4158-4163.

45.	Nakayashiki, S.; Daisuke, H.; Ogomi, Y.; Hayase, S. J. o. P. f. E., Interface structure between titania and perovskite materials observed by quartz crystal microbalance system. **2015,** *5* (1), 057410.

46.	Somsongkul, V.; Lang, F.; Jeong, A. R.; Rusu, M.; Arunchaiya, M.; Dittrich, T. J. p. s. s. R. R. L., Hole blocking PbI2/CH3NH3PbI3 interface. **2014,** *8* (09), 763-766.

47.	Calloni, A.; Abate, A.; Bussetti, G.; Berti, G.; Yivlialin, R.; Ciccacci, F.; Duo, L. J. T. J. o. P. C. C., Stability of organic cations in solution-processed CH3NH3PbI3 perovskites: formation of modified surface layers. **2015,** *119* (37), 21329-21335.

48.	Jacobsson, T. J.; Correa-Baena, J.-P.; Halvani Anaraki, E.; Philippe, B.; Stranks, S. D.; Bouduban, M. E.; Tress, W.; Schenk, K.; Teuscher, J. l.; Moser, J.-E. J. J. o. t. A. C. S., Unreacted PbI2 as a double-edged sword for enhancing the performance of perovskite solar cells. **2016,** *138* (32), 10331-10343.

49.	Burschka, J.; Pellet, N.; Moon, S.-J.; Humphry-Baker, R.; Gao, P.; Nazeeruddin, M. K.; Grätzel, M. J. N., Sequential deposition as a route to high-performance perovskite-sensitized solar cells. **2013,** *499* (7458), 316.

50.	Jeon, N. J.; Noh, J. H.; Kim, Y. C.; Yang, W. S.; Ryu, S.; Seok, S. I. J. N. m., Solvent engineering for high-performance inorganic–organic hybrid perovskite solar cells. **2014,** *13* (9), 897.

51.	Liu, M.; Johnston, M. B.; Snaith, H. J. J. N., Efficient planar heterojunction perovskite solar cells by vapour deposition. **2013,** *501* (7467), 395.

52.	Chen, Q.; Zhou, H.; Hong, Z.; Luo, S.; Duan, H.-S.; Wang, H.-H.; Liu, Y.; Li, G.; Yang, Y. J. J. o. t. A. C. S., Planar heterojunction perovskite solar cells via vapor-assisted solution process. **2013,** *136* (2), 622-625.

53.	Liang, P. W.; Liao, C. Y.; Chueh, C. C.; Zuo, F.; Williams, S. T.; Xin, X. K.; Lin, J.; Jen, A. K. Y. J. A. m., Additive enhanced crystallization of solution-processed perovskite for highly efficient planar-heterojunction solar cells. **2014,** *26* (22), 3748-3754.

54.	Im, J.-H.; Jang, I.-H.; Pellet, N.; Grätzel, M.; Park, N.-G. J. N. n., Growth of CH 3 NH 3 PbI 3 cuboids with controlled size for high-efficiency perovskite solar cells. **2014,** *9* (11), 927.

55.	Ren, X.; Yang, Z.; Yang, D.; Zhang, X.; Cui, D.; Liu, Y.; Wei, Q.; Fan, H.; Liu, S. F. J. N., Modulating crystal grain size and optoelectronic properties of perovskite films for solar cells by reaction temperature. **2016,** *8* (6), 3816-3822.

56.	Liang, Z.; Zhang, S.; Xu, X.; Wang, N.; Wang, J.; Wang, X.; Bi, Z.; Xu, G.; Yuan, N.; Ding, J. J. R. a., A large grain size perovskite thin film with a dense structure for planar heterojunction

solar cells via spray deposition under ambient conditions. **2015,** *5* (74), 60562-60569.

57.	Fei, C.;	Li, B.;	Zhang, R.;	Fu, H.;	Tian, J.; Cao, G. J. A. E. M., Highly efficient and stable perovskite solar cells based on monolithically grained CH3NH3PbI3 film. **2017,** *7* (9), 1602017.

58.	Kim, W.;	Jung, M. S.;	Lee, S.;	Choi, Y. J.;	Kim, J. K.;	Chai, S. U.;	Kim, W.;	Choi, D. G.; Ahn, H.; Cho, J. H. J. A. E. M., Oriented Grains with Preferred Low-Angle Grain Boundaries in Halide Perovskite Films by Pressure-Induced Crystallization. **2018,** *8* (10), 1702369.

59.	Bi, C.;	Wang, Q.;	Shao, Y.;	Yuan, Y.;	Xiao, Z.; Huang, J. J. N. c., Non-wetting surface-driven high-aspect-ratio crystalline grain growth for efficient hybrid perovskite solar cells. **2015,** *6,* 7747.

60.	Kim, D. H.;	Park, J.;	Li, Z.;	Yang, M.;	Park, J. S.;	Park, I. J.;	Kim, J. Y.;	Berry, J. J.; Rumbles, G.; Zhu, K. J. A. M., 300% enhancement of carrier mobility in uniaxial-oriented perovskite films formed by topotactic-oriented attachment. **2017,** *29* (23), 1606831.

61.	Colella, S.;	Mosconi, E.;	Fedeli, P.;	Listorti, A.;	Gazza, F.;	Orlandi, F.;	Ferro, P.; Besagni, T.;	Rizzo, A.; Calestani, G. J. C. o. M., MAPbI3-xCl x mixed halide perovskite for hybrid solar cells: the role of chloride as dopant on the transport and structural properties. **2013,** *25* (22), 4613-4618.

62.	Stranks, S. D.;	Eperon, G. E.;	Grancini, G.;	Menelaou, C.;	Alcocer, M. J.;	Leijtens, T.; Herz, L. M.;	Petrozza, A.; Snaith, H. J. J. S., Electron-hole diffusion lengths exceeding 1 micrometer in an organometal trihalide perovskite absorber. **2013,** *342* (6156), 341-344.

63.	Buin, A.;	Comin, R.;	Xu, J.;	Ip, A. H.; Sargent, E. H. J. C. o. M., Halide-dependent electronic structure of organolead perovskite materials. **2015,** *27* (12), 4405-4412.

64.	Buin, A.;	Pietsch, P.;	Xu, J.;	Voznyy, O.;	Ip, A. H.;	Comin, R.; Sargent, E. H. J. N. l., Materials processing routes to trap-free halide perovskites. **2014,** *14* (11), 6281-6286.

65.	Yin, W.-J.;	Shi, T.; Yan, Y. J. A. P. L., Unusual defect physics in CH3NH3PbI3 perovskite solar cell absorber. **2014,** *104* (6), 063903.

66.	Stewart, R. J.;	Grieco, C.;	Larsen, A. V.;	Maier, J. J.; Asbury, J. B. J. T. j. o. p. c. l., Approaching bulk carrier dynamics in organo-halide perovskite nanocrystalline films by surface passivation. **2016,** *7* (7), 1148-1153.

67.	Noel, N. K.;	Abate, A.;	Stranks, S. D.;	Parrott, E. S.;	Burlakov, V. M.;	Goriely, A.; Snaith, H. J. J. A. n., Enhanced photoluminescence and solar cell performance via Lewis base passivation of organic–inorganic lead halide perovskites. **2014,** *8* (10), 9815-9821.

68.	Xu, J.;	Buin, A.;	Ip, A. H.;	Li, W.;	Voznyy, O.;	Comin, R.;	Yuan, M.;	Jeon, S.;	Ning, Z.; McDowell, J. J. N. c., Perovskite–fullerene hybrid materials suppress hysteresis in planar diodes. **2015,** *6,* 7081.

69.	De Marco, N.;	Zhou, H.;	Chen, Q.;	Sun, P.;	Liu, Z.;	Meng, L.;	Yao, E.-P.;	Liu, Y.; Schiffer, A.; Yang, Y. J. N. l., Guanidinium: a route to enhanced carrier lifetime and open-circuit voltage in hybrid perovskite solar cells. **2016,** *16* (2), 1009-1016.

70.	Edri, E.;	Kirmayer, S.;	Mukhopadhyay, S.;	Gartsman, K.;	Hodes, G.; Cahen, D. J. N. c., Elucidating the charge carrier separation and working mechanism of CH 3 NH 3 PbI 3− x Cl x

perovskite solar cells. **2014,** *5*, 3461.

71.   Yun, J. S.; Ho-Baillie, A.; Huang, S.; Woo, S. H.; Heo, Y.; Seidel, J.; Huang, F.; Cheng, Y.-B.; Green, M. A. J. T. j. o. p. c. l., Benefit of grain boundaries in organic–inorganic halide planar perovskite solar cells. **2015,** *6* (5), 875-880.

72.   Stewart, R. J.; Grieco, C.; Larsen, A. V.; Doucette, G. S.; Asbury, J. B. J. T. J. o. P. C. C., Molecular origins of defects in organohalide perovskites and their influence on charge carrier dynamics. **2016,** *120* (23), 12392-12402.

73.   Cao, J.; Jing, X.; Yan, J.; Hu, C.; Chen, R.; Yin, J.; Li, J.; Zheng, N. J. J. o. t. A. C. S., Identifying the molecular structures of intermediates for optimizing the fabrication of high-quality perovskite films. **2016,** *138* (31), 9919-9926.

74.   Manglik, A.; Sharma, S.; Kudesia, V. J. R. K.; Letters, C., Kinetics of oxidation of isopropyl alcohol by aóueous iodine. **1981,** *15* (4), 467-473.

75.   Gardner, J. M.; Abrahamsson, M.; Farnum, B. H.; Meyer, G. J. J. J. o. t. A. C. S., Visible light generation of iodine atoms and I— I bonds: Sensitized I— oxidation and I3— photodissociation. **2009,** *131* (44), 16206-16214.

76.   Ball, J. M.; Petrozza, A. J. N. E., Defects in perovskite-halides and their effects in solar cells. **2016,** *1* (11), 16149.

77.   Heo, S.; Chung, J.; Lee, H.-I.; Lee, J.; Park, J.-B.; Cho, E.; Kim, K.; Kim, S. H.; Park, G. S.; Lee, D. J. S. r., Defect visualization of Cu (InGa)(SeS) 2 thin films using DLTS measurement. **2016,** *6*, 30554.

78.   Fu, W.; Yan, J.; Zhang, Z.; Ye, T.; Liu, Y.; Wu, J.; Yao, J.; Li, C.-Z.; Li, H.; Chen, H. J. S. E. M.; Cells, S., Controlled crystallization of CH3NH3PbI3 films for perovskite solar cells by various PbI2 (X) complexes. **2016,** *155*, 331-340.

79.   Shi, J.; Xu, X.; Li, D.; Meng, Q. J. S., Interfaces in perovskite solar cells. **2015,** *11* (21), 2472-2486.

80.   Han, Q.; Bae, S. H.; Sun, P.; Hsieh, Y. T.; Yang, Y.; Rim, Y. S.; Zhao, H.; Chen, Q.; Shi, W.; Li, G. J. A. M., Single crystal formamidinium lead iodide (FAPbI3): insight into the structural, optical, and electrical properties. **2016,** *28* (11), 2253-2258.

81.   Stranks, S. D.; Burlakov, V. M.; Leijtens, T.; Ball, J. M.; Goriely, A.; Snaith, H. J. J. P. R. A., Recombination kinetics in organic-inorganic perovskites: excitons, free charge, and subgap states. **2014,** *2* (3), 034007.

82.   Herz, L. M. J. A. r. o. p. c., Charge-carrier dynamics in organic-inorganic metal halide perovskites. **2016,** *67*, 65-89.

83.   Li, Z.; Yang, M.; Park, J.-S.; Wei, S.-H.; Berry, J. J.; Zhu, K. J. C. o. M., Stabilizing perovskite structures by tuning tolerance factor: formation of formamidinium and cesium lead iodide solid-state alloys. **2015,** *28* (1), 284-292.

84.   Saliba, M.; Matsui, T.; Domanski, K.; Seo, J.-Y.; Ummadisingu, A.; Zakeeruddin, S. M.; Correa-Baena, J.-P.; Tress, W. R.; Abate, A.; Hagfeldt, A. J. S., Incorporation of rubidium cations into perovskite solar cells improves photovoltaic performance. **2016,** *354* (6309), 206-209.

85.   Saliba, M.; Matsui, T.; Seo, J.-Y.; Domanski, K.; Correa-Baena, J.-P.; Nazeeruddin, M. K.; Zakeeruddin, S. M.; Tress, W.; Abate, A.; Hagfeldt, A. J. E.; science, e., Cesium-containing triple cation perovskite solar cells: improved stability, reproducibility and high efficiency. **2016,** *9* (6), 1989-1997.

86.   Noh, J. H.; Seok, S. I. J. M. B., Steps toward efficient inorganic–organic hybrid perovskite solar cells. **2015,** *40* (8), 648-653.

Abstract (in Korean)

지난 몇 년 동안 금속 할라이드 페로브스카이트는 매우 유망한 PV 소재로써 태양전지 연구 분야에서 큰 주목을 받고 있다. 페로브스카이트 소재는 낮은 트랩 밀도로 인한 장 거리 전하 캐리어의 확산 길이, 직접 밴드 갭으로 인한 높은 흡수 계수, 높은 개방 회로 전압 & 작은 엑시톤 결합 에너지와 같은 우수한 광전지 특성을 보인다. 또한 페로브스카이트 태양전지는 용액 및 저 비용 공정을 통해 제조될 수 있다.

최근, 페로브스카이트 태양전지의 기록 효율은 1 sun condition에서 24.2% 이상에 도달하였다고 국립 신 재생 에너지 연구소(National Renewable Energy Laboratory)에 의해 보고 되었다.

효율적인 페로브스카이트 태양전지를 만들기 위해서는 많은 요구사항들을 필요로 한다. 그중, 페로브스카이트 필름의 quality는 선행적으로 만족되어야 하는 필수 사항이다. 소재 자체의 조성을 제어하는 것 이상으로, 기판상에 치밀하고 균일한 필름을 형성하는 것이 고성능 페로브스카이트 태양전지의 제조에 결정적이다. 특히, 용액공정에 의해 제조되는 페로브스카이트 필름의 quality는 coating 방법에 따라 크게 달라질 수 있다. 태양전지의 고효율을 달성하기 위해, 페로브스카이트 필름은 적절한 형태학적 특성을 가져야 한다. 충분히 큰 입자, 전체 표면 커버리지, 낮은 표면 거칠기 및 양호한 입자간 연결을 포함한다. 하자만, 일반 유기 필름과는 다르게 MAI or FAI와 PbI2 간의 빠른 반응 및 자기 조립 성질로 인해 다양한 필름 형태가 나타나기 때문에 단순 스핀 코팅을 이용하여 균일하고 치밀한 필름을 형성하기는 매우 어렵다. 따라서 빠른 결정화 거동을 제어함으로써 표면 평탄도를 개선하고 표면 결합을 완전하게 하는 증착 방법의 개발이 중요하다.

1 장에서는 스핀 코팅 공정 중 저온에서 FAI와의 분자 교환 능력이 우수한 PbI_2(DMSO) 전구체 합성 및 20 %를 초과하는 인증된 PCE를 갖춘 고효율 $FAPbI_3$ 기반 PSC의 제조에 대해 보고한다. 사전 증착 된 PbI_2(DMSO) 필름과 FAI (MABr) 용액을 사용하여 DMSO와

FAI (MABr) 사이의 분자 내 교환을 통해 FAPbI$_3$ 기반 PSC를 제조한다. PbI$_2$(DMSO)로부터 유래된 FAPbI$_3$ 필름은 보다 큰 입자를 갖는 고밀도이고 잘 발달된 입자 구조를 나타냈다. 약 500 nm의 두께로 FAPbI$_3$ 기반 필름을 증착하고 불소가 도핑 된 산화 주석 (FTO) - 유리 / blocking layer (bl) -TiO$_2$ / mesoporous (mp) -TiO$_2$ / perovskite / poly-triarylamine (PTAA) / Au 구조의 태양전지를 제작하였다. FAPbI$_3$ 기반 층을 갖는 제조된 소자의 전류 밀도 - 전압 (J-V) 곡선을 표준 공기 질량 1.5 글로벌 (AM 1.5G) 조명 하에서 측정하고 외부 양자 효율 (EQE) 스펙트럼을 측정하였다. 최고 성능의 태양 전지 중 하나에 대해 역방향 및 순방향 바이어스 스윕을 통해 J-V 곡선을 측정하였다. 제작한 장치에서 히스테리시스 현상은 나타나지 않는다. J-V 곡선으로부터 결정된 J$_{SC}$, V$_{OC}$ 및 FF는 각각 24.7 mA / ㎠, 1.06 V 및 77.5 %였고 표준 AM 1.5G 조명 하에서 20.2 %의 PCE에 해당한다. 이 연구는 효율적이고 비용 효율적인 무기 - 유기 하이브리드 접합 태양 전지를 제작하기위한 효과적인 프로토콜을 제공한다.

2 장에서는 분자 내 교환 법 (IEPs)의 첨가물을 제어하여 소자의 광전지 변환 효율을 증가시키기 위한 실험을 진행하였다. PbI$_2$, FAI 및 MAC1의 순도와 첨가 농도를 제어하였다. 집광, 전자 전달, 전자 확산 등의 광학적 물성을 향상시키기 위해서는 균일하고 큰 결정립을 가지고 결함이 거의 없는 필름 형상을 제어하는 것이 중요하다. PbI$_2$, FAI 및 MACl은 IEP에서 균일하고 큰 결정 성 FAPbI$_3$ 필름을 만드는데 중요한 기여를 한다. 각 물질의 조건에 따른 FAPbI$_3$ 필름의 형태 변화를 FESEM을 통해 관찰하였고, 고효율 페로브스카이트 태양 전지의 제조를 위한 물질 조건을 확인하였다.

3 장에서 결함 제어된 페로브스카이트 필름의 조성을 사용하여 인증된 PCE를 소형 셀에서 22.1 %, 1cm^2 셀에서 19.7 %를 달성하였다. Deep-Level Transient Spectroscopy (DLTS) 및 시간 상관 단일 광자 계수 (TCSPC) 측정을 사용하여 IEPs 방법으로 생성된 페로브스카이트 필름을 분석하였다. 페로브스카이트 필름을 형성하기 위해 사용된 유기 양이온 용액에 아이오다이드 이온을 첨가하면 미세 구조 현상, 딥 결함의 집중 및 전하 캐리어 재조

합에 상당한 영향을 미친다는 것을 확인하였다. 우리는 페로브스카이트 층에서 할로겐화

물 음이온의 관리가 고효율 PSC 생산의 새로운 방향을 제공할 것이라고 생각한다.

궁극적으로, 분자 내 교환 법 (IEPs)을 통해 deep level 결함 및 전하 캐리어 재결합의

농도를 제어함으로써 phase-pure & high-quality morphology FAPbI$_3$ 필름을 제조할 수 있었고,

이는 고효율 페로브스카이트 태양 전지 제조를 위한 방향성을 제공할 것이라고 생각한다.

Research Achievements

1. Min, H., Kim, G., Paik, M. J., Lee, S., <u>Yang, W. S.</u>, Jung, M., & Seok, S. I. (2019). Perovskite Solar Cells: Stabilization of Precursor Solution and Perovskite Layer by Addition of Sulfur (Adv. Energy Mater. 17/2019). *Advanced Energy Materials*, *9*(17), 1970056.

2. Park, B. W., Kedem, N., Kulbak, M., <u>Yang, W. S.</u>, Jeon, N. J., Seo, J., ... & Cahen, D. (2018). Understanding how excess lead iodide precursor improves halide perovskite solar cell performance. *Nature communications*, *9*(1), 3301.

3. <u>Yang, W. S.</u>, Park, B. W., Jung, E. H., Jeon, N. J., Kim, Y. C., Lee, D. U., ... & Seok, S. I. (2017). Iodide management in formamidinium-lead-halide–based perovskite layers for efficient solar cells. *Science*, *356*(6345), 1376-1379.

4. Shin, S. S., Yeom, E. J., <u>Yang, W. S.</u>, Hur, S., Kim, M. G., Im, J., ... & Seok, S. I. (2017). Colloidally prepared La-doped BaSnO3 electrodes for efficient, photostable perovskite solar cells. *Science*, *356*(6334), 167-171.

5. Chen, S., Wen, X., Yun, J. S., Huang, S., Green, M., Jeon, N. J., <u>Yang, W. S.</u>, ... & Ho-Baillie, A. (2017). Spatial distribution of lead iodide and local passivation on organo-lead halide perovskite. *ACS applied materials & interfaces*, *9*(7), 6072-6078.

6. Yeom, E. J., Shin, S. S., <u>Yang, W. S.</u>, Lee, S. J., Yin, W., Kim, D., ... & Seok, S. I. (2017). Controllable synthesis of single crystalline Sn-based oxides and their application in perovskite solar cells. *Journal of Materials Chemistry A*, *5*(1), 79-86.

7. Jung, M., Kim, Y. C., Jeon, N. J., <u>Yang, W. S.</u>, Seo, J., Noh, J. H., & Il Seok, S. (2016). Thermal Stability of CuSCN Hole Conductor-Based Perovskite Solar Cells. *ChemSusChem*, *9*(18), 2592-2596.

8. Shin, S. S., <u>Yang, W. S.</u>, Yeom, E. J., Lee, S. J., Jeon, N. J., Joo, Y. C., ... & Seok, S. I. (2016). Tailoring of electron-collecting oxide nanoparticulate layer for flexible perovskite solar cells. *The journal of physical chemistry letters*, *7*(10), 1845-1851.

9. Kim, Y. C., Jeon, N. J., Noh, J. H., <u>Yang, W. S.</u>, Seo, J., Yun, J. S., ... & Ahn, T. K. (2016). Beneficial effects of PbI2 incorporated in organo-lead halide perovskite solar cells. *Advanced Energy Materials*, *6*(4), 1502104.

10. Seo, J., Jeon, N. J., <u>Yang, W. S.</u>, Shin, H. W., Ahn, T. K., Lee, J., ... & Seok, S. I. (2015). Effective Electron Blocking of CuPC-Doped Spiro-OMeTAD for Highly Efficient Inorganic–Organic Hybrid Perovskite Solar Cells. *Advanced Energy Materials*, *5*(20), 1501320.

11. Shin, S. S., <u>Yang, W. S.</u>, Noh, J. H., Suk, J. H., Jeon, N. J., Park, J. H., ... & Seok, S. I. (2015). High-performance flexible perovskite solar cells exploiting Zn 2 SnO 4 prepared in solution below 100 C. *Nature communications*, *6*, 7410.

12. <u>Yang, W. S.</u>, Noh, J. H., Jeon, N. J., Kim, Y. C., Ryu, S., Seo, J., & Seok, S. I. (2015). High-performance photovoltaic perovskite layers fabricated through intramolecular exchange. *Science*, *348*(6240), 1234-1237.

13. Jeon, N. J., Noh, J. H., <u>Yang, W. S.</u>, Kim, Y. C., Ryu, S., Seo, J., & Seok, S. I. (2015). Compositional engineering of perovskite materials for high-performance solar cells. *Nature*, *517*(7535), 476.

14. Jeon, N. J., Noh, J. H., Kim, Y. C., <u>Yang, W. S.</u>, Ryu, S., & Seok, S. I. (2014). Solvent engineering for high-performance inorganic–organic hybrid perovskite solar cells. *Nature materials*, *13*(9), 897.

15. Choi, Y. C., Lee, Y. H., Im, S. H., Noh, J. H., Mandal, T. N., <u>Yang, W. S.</u>, & Seok, S. I. (2014). Efficient Inorganic-Organic Heterojunction Solar Cells Employing Sb2 (Sx/Se1-x) 3 Graded-Composition Sensitizers. *Advanced Energy Materials*, *4*(7), 1301680.

16. Choi, Y. C., Mandal, T. N., <u>Yang, W. S.</u>, Lee, Y. H., Im, S. H., Noh, J. H., & Seok, S. I. (2014). Sb2Se3-sensitized inorganic–organic heterojunction solar cells fabricated using a single-source precursor. *Angewandte Chemie International Edition*, *53*(5), 1329-1333.

17. Ryu, S., Noh, J. H., Jeon, N. J., Kim, Y. C., <u>Yang, W. S.</u>, Seo, J., & Seok, S. I. (2014). Voltage output of efficient perovskite solar cells with high open-circuit voltage and fill factor. *Energy & Environmental Science*, *7*(8), 2614-2618.